

**Faculteit Wetenschappen**  
**Departement Chemie**  
**Afdeling Moleculaire en nanomaterialen**



---

KATHOLIEKE  
UNIVERSITEIT  
LEUVEN

## **An experimental study on the preparation of gold nanoparticles and their properties**

Promotoren:

Prof. Dr. André Persoons

Prof. Dr. Thierry Verbiest

Tom Mortier

Doctoraatsproefschrift

-Mei 2006-

Copyright Faculteit Wetenschappen, Departement Chemie

ISBN 90-8649-007-7

Wettelijk depot D/2006/10.705/4

UDC 62-039.3

**Leden van de jury:**

Prof. Dr. André Persoons, promotor

Prof. Dr. Thierry Verbiest, promotor

Prof. Dr. Steven De Feyter

Prof. Dr. Wim Dehaen

Prof. Dr. Yves Engelborghs

Prof. Dr. Roberto Lazzaroni



# ***Dankwoord***

*Met dit proefschrift wordt een belangrijke periode uit mijn leven afgesloten en daarom zou ik in eerste instantie alle mensen willen danken die in min of meerdere mate hebben bijgedragen tot mijn ontwikkeling.*

*Er zou geen sprake zijn van dit werk was als Prof. Dr. André Persoons en Prof. Dr. Thierry Verbiest me niet de kans hadden gegeven om zelfstandig te werken aan een project. Dankuwel voor het vertrouwen.*

*De juryleden wil ik danken voor het nalezen van mijn manuscript en het geven van waardevolle aanwijzingen.*

*Alle ESEM figuren werden genomen door Ing. Rudy De Vos. Dankjewel Rudy voor je grote bijdrage aan dit proefschrift. I also would like to thank Dr. Palash Gangopadhyay and Dr. Sung-Hoon Joo for their contributions to this PhD thesis.*

*In de jaren dat ik verbonden was aan het labo, heb ik vele gesprekken gevoerd met verschillende medewerkers. Ik wil zeker niemand vergeten en dank jullie allen voor de aanmoediging en ondersteuning.*

*De financiële steun nodig voor het tot stand komen van dit werk, kwam van het “Instituut voor de aanmoediging van Innovatie door Wetenschap en Technologie in Vlaanderen (IWT-Vlaanderen)”. Het was een opsteker om te beseffen dat het fundamenteel onderzoek gepresenteerd in dit proefschrift ook een kans kreeg van de IWT-jury.*

*Mijn moeder en grootmoeder dank ik voor hun steun gedurende mijn volledige studie.*

*Dr. Erik Buntinx ben ik dankbaar omdat hij steeds in me is blijven geloven.*

*Tot slot gaat al mijn dankbaarheid uit naar Natalie omdat jouw liefde fundamenteel was om door te zetten. Ons dochtertje Lenne is bovendien het mooiste geschenk wat ik kon wensen.*



# CONTENTS

<b>Preface</b> . . . . .	xi
 <b>Part I General Background</b>	 1
<b>1. Historical Overview</b> . . . . .	3
1.1 Introduction . . . . .	3
1.2 Gold in the ancient civilizations . . . . .	3
1.3 Potable gold in medicine during the Middle Ages . . . . .	5
1.4 The Purple of Cassius . . . . .	7
1.5 A more scientific approach to colloidal gold . . . . .	8
1.5.1 Dr. Michael Faraday on diffused particles of gold . . . . .	8
1.5.2 Light Scattering in Colloidal Solutions by Gustav Mie . . .	10
1.5.3 Nobel Laureate Richard Adolf Zsigmondy . . . . .	10
1.6 The renaissance of gold nanoparticles . . . . .	11
 <b>2. Theoretical Background</b> . . . . .	 13
2.1 Introduction . . . . .	13
2.2 Nanoscaled Materials . . . . .	13
2.3 Gold Chemistry . . . . .	16
2.3.1 Properties and use . . . . .	16
2.3.2 Stability and chemical reactivity . . . . .	17
2.3.3 Gold complexes . . . . .	22
2.3.4 UV-Vis spectroscopy of gold complexes . . . . .	23
2.4 Colloid Stability . . . . .	26
2.4.1 Electrostatic forces and electrical potential . . . . .	27

2.4.2	The electric double layer surrounding the metal particles .	27
2.4.3	Mathematical derivation of the Diffuse Layer . . . . .	31
2.4.4	Nanoparticle Stability- The DVLO theory . . . . .	34
2.4.5	Steric Stabilization . . . . .	36
2.5	Optical properties of small metal particles . . . . .	38
2.5.1	Surface Plasmon Resonances . . . . .	38
2.5.2	The Lorentz-Drude-Sommerfeld Model . . . . .	39
2.5.3	Light Absorption by spherical Metal Colloids . . . . .	44
2.5.4	Size dependence of spherical metal nanoparticles on the plasmon absorption band . . . . .	47
2.5.5	Light Absorption by Metal Nanorods . . . . .	49
2.5.6	Light Absorption by Metal Core-Shell particles . . . . .	51
<b>Part II</b>	<b>Results &amp; Discussions</b>	<b>53</b>
<b>3.</b>	<b>Wet chemical synthesis techniques for small spherical particles . . .</b>	<b>55</b>
3.1	Introduction . . . . .	55
3.2	The citrate reduction method . . . . .	55
3.3	The Brust Method . . . . .	58
3.3.1	Stabilization of gold colloids with thiocholesterol . . . . .	59
3.3.2	Stabilization of gold colloids by polythiophenes . . . . .	62
3.4	Optical activity coming from gold clusters and gold complexes . .	64
3.4.1	Gold-Glutathione cluster compounds . . . . .	64
3.4.2	L-Cysteinato-gold(I) complexes . . . . .	66
3.4.3	Gold-L-cysteine-ethyl ester cluster compounds . . . . .	68
3.5	Conclusions . . . . .	69
<b>4.</b>	<b>Preparation of small metal particles by Laser ablation . . . . .</b>	<b>71</b>
4.1	Introduction . . . . .	71
4.2	Experimental set-up . . . . .	72
4.3	Laser ablation of the coinage metals . . . . .	72
4.4	Theoretical Discussion . . . . .	74
4.4.1	The Dynamic Formation Mechanism . . . . .	74



---

4.4.2	The Laser-induced Size Reduction Process . . . . .	75
4.5	Laser ablation of gold in chloroform . . . . .	76
4.5.1	Experimental Results . . . . .	76
4.5.2	A proposal for the Laser Ablation Mechanism . . . . .	79
4.6	Conclusions . . . . .	81
<b>5.</b>	<b>Preparation of small metal particles using ultrasound . . . . .</b>	<b>83</b>
5.1	Introduction . . . . .	83
5.2	Sonochemical fabrication of colloidal gold . . . . .	83
5.3	Oxidation of solid gold using ultrasound . . . . .	85
5.3.1	Experimental Results . . . . .	86
5.3.2	Gold colloid formation . . . . .	88
5.4	Conclusions . . . . .	91
<b>6.</b>	<b>Wet chemical synthesis of gold nanorods . . . . .</b>	<b>93</b>
6.1	Introduction . . . . .	93
6.2	Optical properties of gold nanorods . . . . .	93
6.3	Two-step synthesis of high aspect ratio gold nanorods . . . . .	95
6.3.1	Experimental procedure . . . . .	96
6.3.2	Experimental results . . . . .	96
6.4	Conclusions . . . . .	101
<b>7.</b>	<b>Wet chemical synthesis of gold nanoshells . . . . .</b>	<b>103</b>
7.1	Introduction . . . . .	103
7.2	Optical properties of gold nanoshells . . . . .	103
7.3	Experimental Procedure & Results . . . . .	104
7.4	Conclusions . . . . .	109
	<b>General Conclusions &amp; Summary . . . . .</b>	<b>111</b>
	<b>Appendix . . . . .</b>	<b>113</b>
<b>A.</b>	<b>Group theory applications for gold complexes . . . . .</b>	<b>115</b>
A.1	Molecular vibrations . . . . .	115

---

A.1.1	Square-planar complexes $[\text{AuX}_4]^-$ . . . . .	116
A.1.2	Linear molecules $[\text{AuX}_2]^-$ . . . . .	119
A.2	Ultraviolet-Visible Spectroscopy . . . . .	121
A.2.1	Ligand Field Theory . . . . .	121
A.2.2	Symmetry Adapted Linear Combinations (SALCs) . . . . .	122
<b>B.</b>	<b>Derivation of the flat electrical double layer</b> . . . . .	<b>127</b>
<b>References</b>	. . . . .	<b>131</b>
<b>Publications</b>	. . . . .	<b>139</b>
<b>Nederlandse Samenvatting</b>	. . . . .	<b>141</b>

## PREFACE

The work presented in this PhD thesis is fundamental research dealing with a series of different experimental techniques for the preparation of gold nanoparticles.

Gold nanoparticles have a long history as they were found together with silver nanoparticles in glass manufactured during the Roman empire. The specific optical properties of these small metal nanoparticles attracted many scientists working in both the theoretical and experimental field. The understanding of their properties was fundamental for the start of colloid chemistry and is nowadays a research domain itself in the field of nanoscaled materials with many potential applications.

Part I of this PhD thesis provides a general introduction.

Chapter 1 introduces colloidal gold from a historical point of view. The Lycurgus cup is discussed, as this Roman glass masterpiece shows the effects and the behavior of small metal particles. Techniques to prepare colloidal gold were discovered by the alchemists, but a first recipe was written down in the seventeenth century when gold colloids were used to control the coloration process in glassware. The true nature of colloidal gold however (and colloidal systems in general), was firstly mentioned by Dr. Michael Faraday. His experiments are generally recognized as the start of modern colloid chemistry. An important fact is that he had to oxidize bulk gold to gold complexes prior to the reduction of these complexes in order to prepare kinetically stable gold colloids.

Theoretical issues related to the properties of gold nanoparticles are discussed in Chapter 2. An introduction in gold chemistry is reported including the stability of bulk gold to oxidation and the formation of gold complexes where the oxidized gold atom is stabilized by suitable ligands. The stabilization of colloidal gold however is discussed by focussing on the stability theory of colloids in general. This

chapter ends with a description of plasmon resonances responsible for the remarkable colors of gold and silver nanoparticles in solution.

In Part II of this PhD thesis the experimental results and discussions are given.

Different wet chemical synthesis techniques to fabricate gold nanoparticles are explained in Chapter 3, focussing on introducing chirality in the synthesis methods. Furthermore, the issues related to the stability of colloidal gold systems introduced in Chapter 2 are experimentally verified here.

Chapter 4 and Chapter 5 discuss two physicochemical techniques to fabricate gold nanoparticles, i.e. laser ablation and ultrasonic irradiation.

Laser ablation of bulk gold means that the metal is irradiated by a laser leading to the formation of colloidal gold. The main advantage is the high purity of the nanoparticles and the fact that it can be performed in any solution. Chapter 4 discusses laser ablation in chloroform solutions of a surfactant. We found that laser ablation allows to oxidize gold to form gold complexes. Therefore, a hypothesis for the theory behind the laser ablation experiments is discussed.

Ultrasonic irradiation of gold salts (or gold complexes) is another method for the preparation of gold nanoparticles. With this technique we were equally able to oxidize bulk gold in chloroform solutions of a surfactant and in Chapter 5 the mechanism behind this phenomenon is discussed by focussing on the stability of bulk gold.

The last two chapters discuss techniques to fabricate gold colloids with different shapes. Changing the shape of gold nanoparticles, modifies their optical properties which makes them valuable candidates for optical applications.

A study of a wet chemical seed-mediated growth technique to prepare gold nanorods is described in Chapter 6. We were able to synthesize gold nanorods with high aspect ratios and average lengths over more than 1  $\mu\text{m}$ . Furthermore, we show that the wet chemical seed-mediated growth technique is size controllable.

In Chapter 7 a wet chemical synthesis technique to prepare gold nanoshells by coating small silica spheres with a continuous gold layer is discussed. We show in this chapter that we were able to coat individual silica nanoparticles simultaneously with a gold layer.

## **Part I**

### **GENERAL BACKGROUND**



# **1. HISTORICAL OVERVIEW**

## **1.1 Introduction**

Since ancient times, gold has been valued in every culture for its beauty as well as for its unique physical and chemical properties. Gold is probably one of the first metals known to man. Long before it became a standard medium for exchange, gold was regarded as divine and offered to the gods. It was mentioned even in the Bible as early as *Genesis*. Moreover, it was valued as the most noble of all the metals.

This chapter gives an overview of the history of (colloidal) gold starting from the ancient times and ending with the renaissance of gold colloids used in the field of nanochemistry.

## **1.2 Gold in the ancient civilizations**

The Babylonians and Assyrians believed that heavenly bodies were controlled by gods who influenced the lives of men. The sun, moon, and ‘five’ planets were the ruling powers of the world. Each was assigned a metal playing an important role in the lives of people. The sun controlled gold as the noblest of metals and silver was linked to the moon [1]. These astrological ideas were accepted by the ancient Egyptians.

The ancient civilizations of Egypt and Mesopotamia developed a high degree of technical skill in metallurgy. These skills were probably developed for the benefit of the king and the temples [2]. Objects made of gold were found in the most ancient graves of Egypt and Mesopotamia. For example, one of the richest golden

treasure store was found in Egypt in 1922 by Howard Carter in the tomb of the pharaoh Tutankhamen.

That compounds of gold could impart a red color had been known for many centuries. Egyptian manuscripts from the Greco-Roman era refer to it [3]. The Egyptians, Greeks and Romans used many colored pigments for the decoration of their buildings, ceramics and glass-ware. The use of gold and silver particles in glass-blowing can be seen in the famous *Lycurgus Cup* (Figure 1.1) exposed in the British Museum [4]. This cup is a late Roman masterpiece and based on the analysis of the glass it was probably made in the fourth century AD. The gilded bronze base and rim were more recent additions. The Cup is called the Lycurgus cup because the inner solid cup is surrounded by a frieze showing the myth of King Lycurgus. The most unusual feature of this cup however is its color. When viewed in reflected



**Fig. 1.1:** The Lycurgus cup dates from the fourth century AD. In reflected light (daylight) the glass appears to be green, but when light is transmitted from the inside of the vessel it is red (by Courtesy of the British Museum) [4].

light, for example in daylight, it appears to be green, but when light is transmitted from the inside of the vessel through the glass, it appears to be red. Chemical analysis of the Lycurgus cup shows that it is similar to most other Roman glass, but



it contains very small amounts of gold (about 40 parts per million) and silver (about 300 parts per million). Figure 1.2 shows a TEM image of a silver-gold alloy coming from a sample from the Lycurgus cup [5]. The crystalline nature of the Ag/Au particles and their fine dispersion in the glass suggests that this colloidal metal was precipitated out from solution by heat treatment.

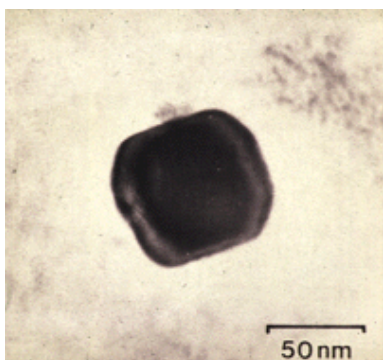


**Fig. 1.2:** TEM image of a Ag/Au alloy (by Courtesy of the British Museum) [5].

There are only a handful of ancient glasses showing this remarkable effect and all of them are Roman. Roman glass makers were used to make red glass using copper, but this was nearly always opaque. They added scrap metal to color their glass and sometimes these materials con-

tained small amounts of gold and silver. The glass of the Lycurgus cup may therefore have been made by an accident because other ancient glasses with gold and silver are less impressive.

Two important works of our early chemical (and gold) knowledge have to be mentioned. There is the *Historia Naturalis*, written by Caius Plinius Secundus, the “Elder Pliny”. This work includes many subjects related to the chemical knowledge around the first century AD and it describes extensively the occurrence, mining and properties of gold. Another treatise *Materia Medica* from the same era was written by Dioscorides Pedanus, a Greek physician. He treated gold from the point of view pertaining to its use in medicine. Dioscorides mentioned that gold is capable of extremely fine subdivisions and serves as an antidote for quicksilver (or mercury) poisoning in the form of thin flakes or leaf [1].

### 1.3 Potable gold in medicine during the Middle Ages

In the Middle Ages, chemistry developed mostly through the protoscience of Alchemy. Its primary goal was transmutation, i.e. the conversion of base metals into gold, which was believed to be achievable by the philosopher’s stone [6, 7]. For

century after century this quest was pursued by many alchemists all over the world, resulting in an extensive knowledge of the physical properties and chemical reactions of an immense variety of natural and artificially prepared substances [8]. In their attempts to transmute base metals into gold, the alchemists contributed a lot to modern chemistry. Alchemical processes required the construction of much scientific apparatus and the invention of many laboratory techniques like heating, refluxing, extraction, sublimation and distillation to treat metals with various chemical substances at elevated temperatures [2]. In the early thirteenth century the improvement of distillation methods resulted in the discovery of the mineral acids which greatly increased the power of the alchemist to dissolve substances and to carry out reactions in solution. The ‘royal’ solvent to dissolve gold was found to be *aqua regia* and was created by adding *sal ammoniac* (ammonium chloride) to *aqua fortis* ( $\text{HNO}_3$ ) [8].

Gold however was the only metal that did not corrode. It symbolized immortality and so it was recommended for medical use in a form that could be consumed internally as potable gold or *aurum potabile*. The idea that liquid gold could be the “elixir of life” probably originated in China [8]. The Chinese alchemist believed that by eating gold he could attain eternal life and become immortal with almost unlimited powers [2].

Theophrastus Bombastus von Hohenheim or Paracelsus, the father of the iatrochemistry, severely criticized the alchemists for their fascination for gold and insisted that they should be better spending their time in the preparation of drugs to relieve suffering [6]. He recommended potable gold in the sixteenth century as a cure for ailments. He believed that it was particularly good for heart disorders because gold and the heart were ruled by the sun [8].

Most preparations for potable gold made during the Middle Ages seem to have been gold sols or colloidal gold. Recipes for the preparation of medicinal colloidal gold were well known by the early seventeenth century and even today potable gold is occasionally encountered [8].

Closely related to its use in medicine, the colloidal gold preparations were used to produce gold ruby glass. This will be discussed in the next section.

## 1.4 The Purple of Cassius

That gold can impart a red color to glass is known for many centuries. In 1612 a first treatise on glass making appeared, written by the Florentine priest Antonio Neri. He visited Venice and Antwerp, the centers of glass arts in that time. He mentioned a glass with “a wonderful red obtained from gold” [3], but the author

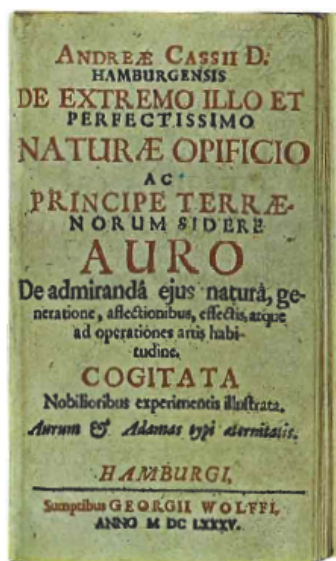


**Fig. 1.3:** Title page of *De Auro* by Andreas Cassius published in Hamburg 1685 [3].

did not refer to the purple preparation of gold with a tin compound. To give glass a red color, they used a gold powder and heated it until it received a purple color and then imparted it into glass. The initial discovery of obtaining the desired red color can be attributed to Johann Rudolph Glauber, probably the first industrial chemist making a living from the sales of his medicinal preparations. Glauber was familiar with several means of precipitating gold from its solution in aqua regia, having a gold chloride solution. He is the first to mention in 1659 that it can be precipitated with a solution of a tin compound to give a “brilliant purple-colored powder” [3] although he was unaware of its immense coloring power and sensitivity. A contemporary chemist, Johann Kunckel, an alchemist, was well experienced in the glass technology and in 1678 he was given charge of the glass factory at Potsdam

by Prince Friedrich Wilhelm of Brandenburg. He had published his *Ars Vitraria Experimentalis, oder Vollkommene Glasmacherkunst*. Herein, the work from Antonio Neri was incorporated together with Kunckel’s own material. This work was a standard treatise on glass technology for many years. In this work there are some veiled references to the production of ruby glass by the use of the purple precipitate, but its successful use to produce a red or ruby glass (referred to as Kunckel glass) was not revealed until the publication *Laboratorium Chymicum* in 1716 in Hamburg some years after his death.

The purple precipitate of gold is mostly referred to as the “Purple of Cassius”. The

reason is that in 1685 a doctor called Andreas Cassius published a basic alchemical work *De Auro*. In this book he described a method for the precipitation of gold. First, tin is dissolved in aqua regia so that the solution becomes completely yellow. Then some gold is dissolved in another solution of aqua regia and finally a large amount of water is poured into an open glass. In this glass, some of the tin solution and the same amount of the gold solution is dissolved. Immediately, a curious precipitation of gold in this water can be seen, turning it into a beautiful reddish purple. Dr. Cassius knew about the work of Johann Kunckel and his special knowledge of chemistry to produce ruby glass on a large scale although it was Johann Rudolph Glauber who firstly optimized the colloidal precipitate of gold [3].

In 1719 basically the same recipe to obtain the “Purple of Cassius” was used for the decoration of porcelain in the factory of Meissen. The *secret* also reached China where it was the basis of the famous *Famille Rose* Chinese porcelain.

## 1.5 A more scientific approach to colloidal gold

In the middle of the nineteenth century a more scientific interest in colloidal systems arose. Dr. Michael Faraday published a comprehensive paper about the preparation and properties of gold sols which can now be seen as the foundation of modern colloid science. The first theoretical description was given by Gustav Mie in the beginning of the twentieth century and in 1925, Richard Zsigmondy received the Nobel price in Chemistry for his work in the field of modern colloid chemistry by studying the properties of gold sols and inventing an ultra microscope.

### 1.5.1 Dr. Michael Faraday on diffused particles of gold

Michael Faraday (1791-1867) is probably the greatest experimentalist of all time. He is mostly known for his contributions in electrochemistry [9], but also for experimental studies in many other areas including the light scattering properties of gold hydrosols. The unusual colors displayed by metal particles forced Dr. Michael Faraday's investigations into the colors of colloidal gold. In 1857 he published a

Bakerian Lecture “Experimental Relations of Gold (and other metals) to Light” in *Philosophical Transactions of the Royal Society* [10]. In this lecture he described



**Fig. 1.4:** Colloidal gold solutions by Michael Faraday (by Courtesy of the Royal Institution of Great Britain).

the optical investigations of very thin gold films and of ruby-red colored suspensions of ultra-microscopic gold particles in various liquids. He described the production of a “ruby fluid” by treating solutions of gold chloride with solid phosphorus and other substances (Figure 1.4). He observed that it was very sensitive to the addition of small quantities of electrolytes and stated “The gold is reduced in exceedingly fine particles, which becoming diffused, to produce a beautiful ruby fluid” [10]. He mentioned that “the fluids have all the appearance of *solutions*, but they are not, containing no dissolved, but only diffused gold. The particles can be easily detected by gathering the rays of the sun into a cone by a lens and sending the part of the cone near the focus into the fluid; the

cone becomes visible, and though the illuminated particles cannot be distinguished because of their minuteness, the light they reflect is golden in character” [10]. The phenomenon that an external observer is able to see light out of the direction of the incident beam is known today as the Faraday-Tyndall effect. John Tyndall (1820-1893) collected Faraday’s observations and wrote a pioneering work in light scattering by small particles suspended in air.

Faraday’s discovery that metals could form colloids was a breakthrough, although the importance of Faraday’s observations on the concept of colloid chemistry was not fully realized at that time. Today his studies are generally considered to mark the foundations of modern colloid science [11]. The word “colloid” however was first introduced by his London colleague Thomas Graham (1805-1869), who is often referred to as “the father of colloid chemistry”. Graham also introduced the expressions hydrosol (an aqueous colloidal solution) and hydrogel (the jelly derived from it) [12].

### 1.5.2 Light Scattering in Colloidal Solutions by Gustav Mie

The German physicist Gustav Mie (1869-1957) first worked in theoretical physics, but he also published work in experimental physics. In 1908 he published an important article on light scattering in matter in *Annalen Der Physik* with the title “Beiträge zur Optik trüber Medien, speziell kolloidaler Metallösungen” [13]. This theoretical work is the foundation of the theory describing the optical properties of small metal particles. Metal particles like gold sols are small in respect to the visible wavelength and they show characteristic absorbing and scattering properties. Gustav Mie calculated the absorbance of colloidal gold particles as a function of the particle size using classical electromagnetic theory with the bulk optical properties of metallic gold.

### 1.5.3 Nobel Laureate Richard Adolf Zsigmondy

In 1925 Richard Adolf Zsigmondy (1865-1929) was awarded the Nobel price [12].

*... for his demonstration of the heterogenous nature of colloid solutions and for the methods he used, which have since become fundamental in modern colloid chemistry.*

Zsigmondy prepared practically equally-sized red gold hydrosols by the reduction of gold chloride with formaldehyde in a weakly alkaline solution. Furthermore, he devised and built an ultramicroscope in 1903 whereby it was possible to observe particles with a diameter of 10-millionth of a millimeter. Using his ultramicroscope, he was able to carry out size determinations of the gold particles by counting the number of gold particles in a given volume of a colloidal gold solution. He showed that colloidal gold particles have a negative electrical charge, which is very important as it is the main cause of their stability. This charge can be taken away by adding salts resulting in an immediate particle aggregation whereby the system coagulates. This is noticeable with colloidal gold by the change in color from red to blue. In the ultramicroscope he noticed not only a color change of the individual particles, but also an important change in the number of particles. The coagulation however, can be interrupted by the addition of protective colloids such as gelatin.

## 1.6 The renaissance of gold nanoparticles

Since colloidal gold has a particle size falling below the resolution limit of the optical microscope, the field of colloids opened up for detailed study with the invention of the electron microscope at the start of World War II [14]. In 1945 the resolution of the electron microscope was 2 nm and decreased ever since. An interesting investigation of various preparations of colloidal gold using the electron microscope as the main tool was started in 1948 at Princeton University and the RCA Laboratories by John Turkevich and colleagues. In his paper in Discussions of the Faraday society [15], Turkevich studied the reduction of gold salt with sodium citrate extensively. This preparative method has been the standard preparation of gold sols, whereas the optical properties of these gold particles, linked with Mie theory, were published by Robert Doremus in 1964 [16]. G. Frens used this citrate reduction method to control the size of gold particles ranging from 16 nm to 150 nm simply by varying the concentration of sodium citrate added to the solution during the nucleation of the particles [17]. The real renaissance of gold nanoparticles however started when M. Brust and colleagues reported a simple reductive method using the borohydride reduction of chloroauric acid in the presence of alkane thiols [18]. This was an exciting development because in some respects gold nanoparticles were behaving as chemical compounds as they were stable over extended periods and could be precipitated, re-dissolved, chromatographed and size separated by fractional crystallization. Functionalized groups on their surfaces allow their incorporation in three dimensional networks and make them useful in a wide range of applications in the fields of sensors and molecular electronics.





## **2. THEORETICAL BACKGROUND**

### **2.1 Introduction**

Nanoscience finds its origin in colloidal science because colloid chemistry covers a lot of theoretical background and expertise needed to understand the specific character of nanoscaled materials [19]. In fact, it was Michael Faraday who identified the real nature of colloidal, nanoscaled metal particles. He pointed out that colloidal metal sols were thermodynamically unstable and that the individual metal (gold) nanoparticles had to be stabilized kinetically to prevent aggregation. In this chapter we will discuss the nanoscaled materials and give an overview of the stability and different oxidation states of gold. In a next section, the theoretical explanation of the stability of colloidal sols shall be described and we end with a theoretical description of the unusual optical properties of small metal particles.

### **2.2 Nanoscaled Materials**

The general vision of nanoscience depends strongly on the ability of creating and manipulating matter at the nanoscale [20]. Figure 2.1 shows the nanoscale in context illustrating the size of a football compared to a carbon 60 ( $C_{60}$ ) molecule. Nanoscaled materials are usually categorized as materials having structured components with at least one dimension less than 100 nm [21]. The research in nanoscaled matter began to grow exponentially when it became recognized that the bulk properties of materials change drastically as their sizes decrease from the bulk material to small clusters of atoms [22]. Suitable control of the properties of nanometer-scale structures can lead to new science as well as new products, devices

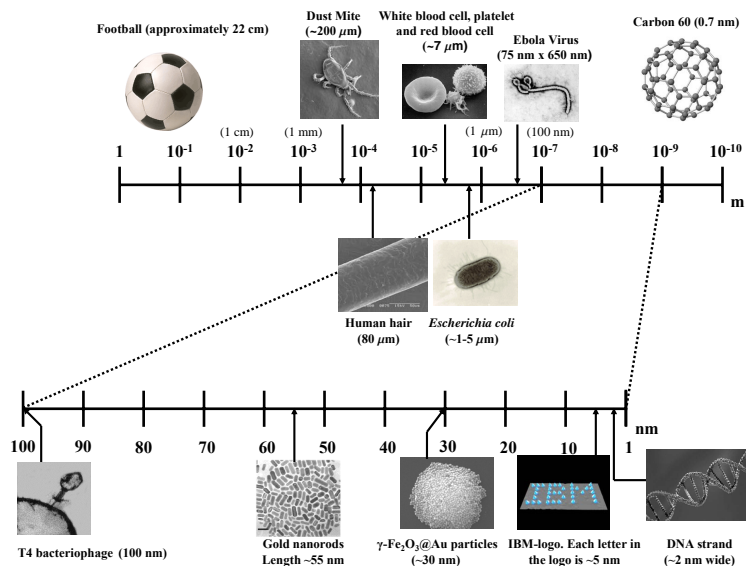
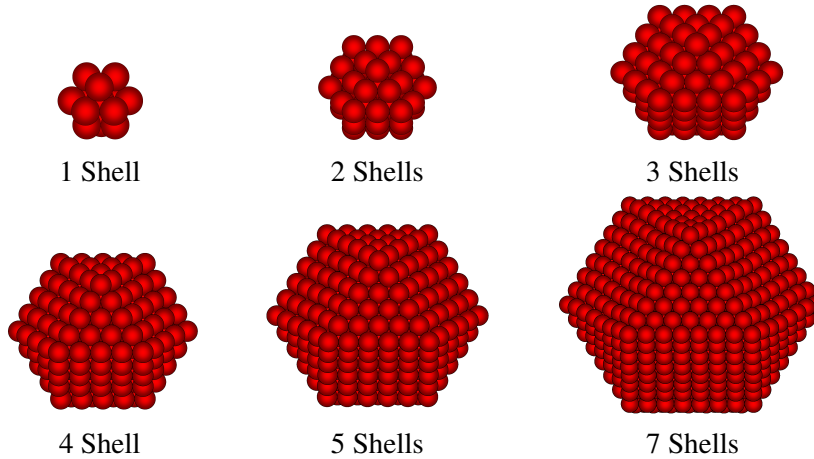


**Fig. 2.1:** Picture showing the nanoscale in context. The length scale at the top ranges from 1 m to  $10^{-10}$  m. The section from  $10^{-7}$  m (100 nm) to  $10^{-9}$  m (1 nm) is expanded on the length scale below. The typical length scale of interest for nanoscience is from 100 nm down to the atomic scale.

and technologies [23]. Two principal factors are responsible for causing the properties of nanoscaled materials to differ significantly from their behavior in bulk condition. Firstly, there is the increased relative surface area and secondly size-dependent properties begin to dominate when matter is reduced to the nanoscale. These effects cannot only change the chemical reactivity and strength drastically, but also the electrical, optical and thermal characteristics. For example, when a metal particle decreases in size to become a nanoparticle or a nanocrystal, a greater proportion of atoms is found at the surface. As catalytic chemical reactions occur at surfaces, this leads to much more reactivity when a given mass in nanoparticulate form is used than when the same mass of material made up of larger particles is doing the catalytic reaction. Metallic nanoclusters are built up by hexagonal (hcp) or cubic (ccp) close-packed atoms (nuclearities) as this is the case in most bulk metals where a central atom is surrounded by 1, 2, 3, ... closed-packed shells. Table 2.1 shows a schematic illustration of metal nanocrystals of different sizes in closed-shell configurations and contains information on the percentage of surface

**Tab. 2.1:** Schematic illustration of metal nanocrystals in closed-shell configurations with their magic numbers of atoms and the relation between the total number of atoms and the percentage of surface atoms [24].

Full-shell Clusters	Total Number of Atoms	Surface Atoms %
1 Shell	13	92
2 Shells	55	76
3 Shells	147	63
4 Shells	309	52
5 Shells	561	45
7 Shells	1415	35



atoms. The number of atoms per shell is  $\sum = 10n^2 + 2$ , where  $n$  is the number of the shell. The smallest closed-shell configuration consists of  $1 + 12 = 13$  atoms, the next of  $13 + 42 = 55$  and so on. The numbers 13, 55, 147, 309, 561 and 1451 stand for magic nuclearities corresponding to the closure of 1, 2, 3, 4, 5 and 7 shells respectively [25]. It is clear from the table that the percentage of surface atoms decreases as the closed-packed shells surrounding the central atom increases. A spherical particle of 50 nm in diameter for example has only 6% of surface atoms left. Furthermore, it is obvious that for millimeter and micrometer-sized particles the surface atoms can be neglected with respect to their contribution on the aver-

age coordination number. Gold for example is a potentially valuable catalyst as it is inert in bulk, but becomes highly reactive at the nanoscale range.

Another example of different properties which can arise when bulk matter is reduced to the nanoscale can be found in the relationship between the melting points of gold and silver nanoparticles and their particle size. Experimental investigations and calculations indicated that there is a dramatic decrease of the melting temperature when particles are smaller than 3-4 nm [24, 26]. Hence, thermodynamic properties change with the dimension of the material.

On the other hand, characteristic size-dependent effects can arise in combination with surface-area effects. Squeezing the atoms' electrons into smaller-than-typical spaces can change properties such as the color of the light they emit. The size-dependent properties are typical in gold sols where the so called *plasmon* oscillation is responsible for the typical ruby-red colors. This surface plasmon excitation is a collective excitation of the free conduction band electrons and this effect can be seen in the visible region of the spectrum. The theory of plasmon resonances will be discussed later in this chapter.

## 2.3 Gold Chemistry

Aqueous solutions containing gold complexes like  $[\text{AuCl}_4]^-$  or  $[\text{AuBr}_4]^-$  are easily reduced to gold and under controlled conditions colloidal gold can be formed. Before dealing with the theory of colloidal stability, we will first discuss the chemistry of gold needed to understand this thesis. This section is largely based on the book "The Chemistry of Gold" by Richard J. Puddephatt [27] and references herein.

### 2.3.1 Properties and use

In the solid form, gold is a soft, yellow metal with the highest ductility and malleability of all the elements. The pure metal melts at 1063°C and boils at 2966°C. It has an atomic weight of 196.967 with a density of 19.32 g cm<sup>-3</sup> at 20°C. Its beauty and rarity has led to the use in jewelry and in coinage. Furthermore, it has been a standard for monetary systems throughout the world for thousands of years.

Since gold is such a soft metal, it is usually alloyed to give more strength. The term carat is used to express the amount of gold present in alloys; 24 carats being pure gold. Alloys of gold with the other elements of group IB are most frequently used. As an example, coinage gold typically contains 10% copper, while gold in jewelery may contain varying proportions of silver and copper. The colors of the alloys are frequently controlled by the other metals.

Gold has many applications in electronics having high thermal and electrical conductivity properties. The high cost of gold however, necessitates the use of very thin films, formed by electroplating on a base metal support, for gold switching devices. Like the other group IB elements, gold crystallizes in the face-centered cubic lattice and the closest inter-nuclear distance is 288.4 pm. At high temperature in the gas phase, gold exists as a mixture of atoms and diatomic molecules.

### 2.3.2 Stability and chemical reactivity

Gold is probably the most noble of the metals, being the only one which is not attacked in water by either oxygen or sulphur at any temperature. To understand this nobility of gold, it is useful to consider the redox potentials of gold in the absence of coordinating ligands. Thus, gold must be oxidized for a reaction to take place. For example,



The tendency for this reaction to take place is given by the Nernst equation or the reduction potential:

$$E = E^\ominus - 2.303 \frac{RT}{F} \log_{10} \frac{[\text{Au}]}{[\text{Au}^+]}$$

where  $R$  is the gas constant,  $F$  the Faraday constant,  $T$  the absolute temperature (25°C or 298K) and  $E^\ominus$  the standard electrode potential for the reaction ( $\sim 1.7$  V). Filling this in by taking  $[\text{Au}]$  as unity, the equation reduces to

$$E = 1.7 + 0.059 \log_{10} [\text{Au}^+]$$

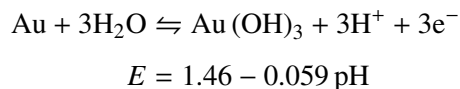
A similar expression can also be written for the alternative oxidation process



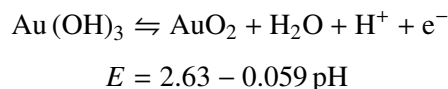
and with  $E_{\text{Au}^{3+}/\text{Au}}^{\ominus} = 1,50$ , we can write similarly

$$E = 1.50 + 0.0197 \log_{10} [\text{Au}^{3+}]$$

When it is oxidized, the metal may also interact with its environment



and

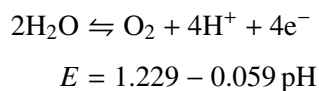


These reactions can only take place if sufficiently strong oxidants are present. The relationship indicating the conditions under which auric hydroxide is in equilibrium with  $10^{-4}$  M auric ions is represented by [28]

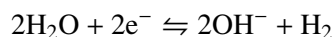
$$\text{Au}^{3+} + 3\text{H}_2\text{O} \rightleftharpoons \text{Au}(\text{OH})_3 + 3\text{H}^{+}$$

$$\text{pH} = -\frac{1}{3} \log_{10} [\text{Au}^{3+}] - 0.693$$

The reactions in aqueous solution are further restricted by the limits of the stability of water as it can be oxidized to oxygen or reduced to hydrogen. The oxidation of water can be written as



The reduction of water is the following redox couple



$$E = 0.0017 - 0.059 \text{ pH}$$

The gold-water system can be expressed graphically in a Pourbaix diagram where the equilibrium potential of each couple is plotted against pH for particular concentrations. A simplified Pourbaix diagram for gold (using a concentration of  $10^{-4}$  M) is shown in Figure 2.2 and indicates the conditions under which particular species

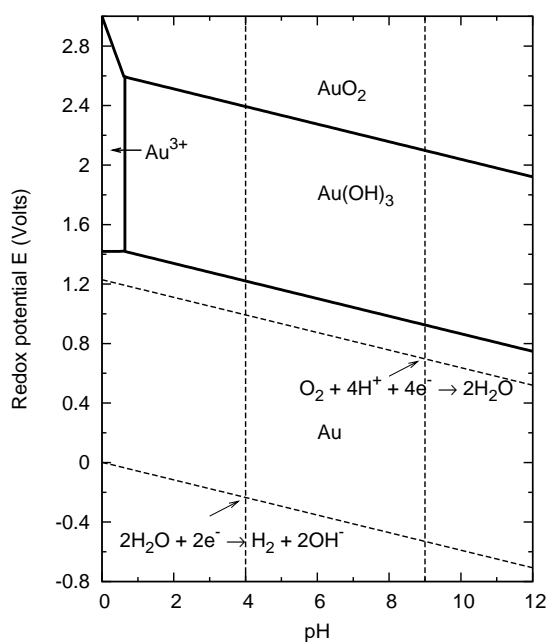
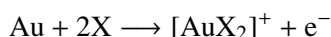


**Fig. 2.2:** Simplified Pourbaix diagram for the system gold-water at 25°C.

are expected to be formed. The dotted lines represent the limits of stability of water. From this Pourbaix diagram, it can be concluded that the oxidized forms of gold only exist at potentials significantly greater than the line of the oxidation of water to oxygen. Thus, under these conditions, water is oxidized to oxygen and the various gold species are reduced to gold metal. It can be concluded that in the absence of coordinating ligands, gold cannot be oxidized by dissolved oxygen in

the presence of either strong acids or strong alkalis. Gold is the only metal with this property and therefore one can say that it is truly the most noble of the metallic elements.

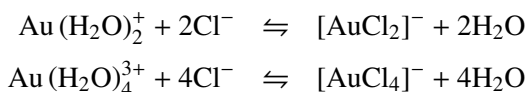
However, gold can dissolve in aqueous solutions containing good ligands for gold and an oxidizing agent, but neither condition alone is sufficient. For example, gold does not dissolve appreciably in hydrochloric or nitric acid separately, but dissolves readily in *aqua regia* to give tetrachloroauric(III)acid,  $[\text{AuCl}_4]^-$ . Similarly, gold dissolves in hydrochloric acid in the presence of hypochlorite or iron(III) as oxidant. The dissolution of gold in cyanide solutions with air or hydrogen peroxide as oxidant is another example of this effect [27]. The reaction with oxygen as oxidizing agent apparently takes place by adsorption of oxygen onto the gold surface, followed by reaction of this surface layer with cyanide to give first AuCN and then the complex  $[\text{AuCN}_2]^-$  which passes into solution. In general, the reaction to oxidize gold to gold(I) in the presence of suitable ligands can be written as



and it is, of course, also possible to oxidize gold to gold(III) in the presence of suitable ligands



The standard potentials  $E^\ominus$  depend on the stability constant for formation of the complex. In the presence of a good ligand a high value of  $K$  and a low value of  $E^\ominus$  is obtained. It is now clear that ionic  $\text{Au}^+$  and  $\text{Au}^{3+}$  can not exist free in solution, but always forms complexes with available ligands. In pure water, the ions form the respective aqua ions and reaction 2.1 and 2.2 are more correctly written in terms of the ions  $\text{Au}(\text{H}_2\text{O})_2^+$  and  $\text{Au}(\text{H}_2\text{O})_4^{3+}$ . If a stronger ligand than  $\text{H}_2\text{O}$  is present (e.g. chloride) the following equilibria are established





As a result the reactions 2.1 and 2.2 reach equilibrium further to the right as can be seen in Figure 2.3. The reduction potentials are reduced and the metal is oxidized

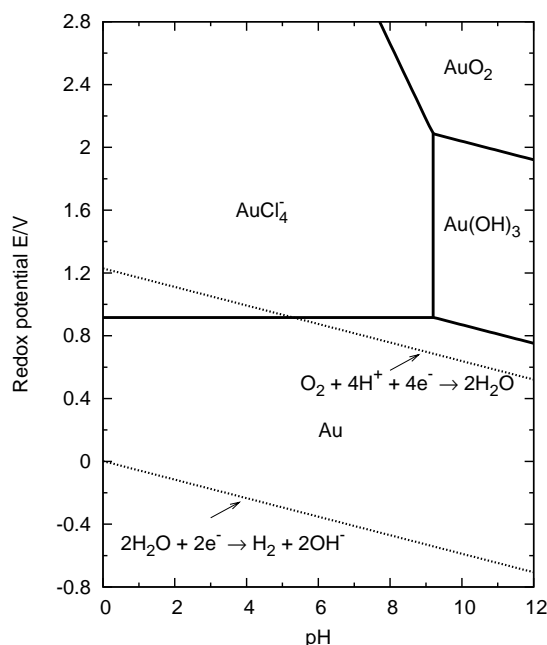


**Fig. 2.3:** Simplified Pourbaix diagram for the system gold-water- $\text{Cl}^-$  at 25°C.

more easily. Figure 2.3 summarizes the effect of the addition of chloride ion to the gold-water system. In this Pourbaix diagram it is clearly seen where the complex  $[\text{AuCl}_4]^-$  is the most stable. Figure 2.3 is drawn for  $\text{Cl}^- = 2\text{ M}$  and  $[\text{Au(III)}] = 10^{-2}\text{ M}$ . In this Figure it is important to see that a part of the domain of stability of  $[\text{AuCl}_4]^-$  falls within the region of stability of water. Therefore, in the presence of the chloride ion, gold can exist in an oxidized form in contact with water under acid conditions. Stronger ligands than chloride obviously increase the domain of stability of the oxidized species.

We end our discussion about the stability of gold by saying that Pourbaix diagrams are very instructive, but it is important to note that they are purely thermodynamic representations and do not consider the kinetic properties of the system.

### 2.3.3 Gold complexes

We have already mentioned the ability of gold to form complexes when suitable ligands are present. However, a large number of gold complexes exists and therefore we will focus our discussion on the halo gold complexes. The stability of gold complexes is related to the atom in the ligand which is bound directly to the gold. Gold(I) and gold(III) are class B metal ions, meaning that the stability of their complexes tends to decrease with increasing electronegativity of the ligand donor atom. Generally, this leads to stability orders as  $I^- > Br^- > Cl^- > F^-$ , whereas the order of electronegativities is  $F^- > Cl^- > Br^- > I^-$ .

For complexes containing a single gold atom, the oxidation states I, II and III are possible<sup>1</sup>. Gold has the electronic configuration  $[Xe] 4f^{14}5d^{10}6s^1$  and belongs to group IB of the periodic table along with copper and silver. We will now discuss the halide gold complexes with different oxidation states of gold separately compared to the other coinage metals.

#### Gold(I) complexes

$Au^+$  has a closed shell electronic configuration  $[Xe] 4f^{14}5d^{10}$ . Therefore, gold(I) complexes are diamagnetic and the stereochemistry of the halo gold(I) complexes is linear with a coordination number two. The stability of the ions  $[AuX_2]^-$  increases with the heavier halide ions. They can be prepared by reduction of  $[AuCl_4]^-$  or  $[AuBr_4]^-$  in ethanol or acetone solutions according to the following reaction



#### Gold(II) complexes

The oxidation state two is the dominant oxidation state for copper, but is very rare for a gold atom. In gold(II) complexes, the metal atom has a  $5d^9$  configuration and such complexes are expected to be paramagnetic. This oxidation state can be es-

<sup>1</sup> Oxidation state V is also possible, but will not be considered here.

tablished as transient intermediates in redox reactions between the stable oxidation states I and III.

### Gold(III) complexes

It has already been stated earlier that gold dissolves in aqua regia to give tetrachloroauric(III) acid,  $\text{H}[\text{AuCl}_4]$ . In a mixture of hydrobromic and nitric acids, gold dissolves to give tetrabromoauric(III) acid,  $\text{H}[\text{AuBr}_4]$ . These strong acids can then be isolated by evaporation of the solutions, with repeated addition of hydrochloric or hydrobromic acid to remove all the nitric acid and nitrogen oxides to generate the hydrated forms  $\text{H}[\text{AuCl}_4] \cdot 3\text{H}_2\text{O}$  and  $\text{H}[\text{AuBr}_4] \cdot x\text{H}_2\text{O}$ . The oxidation state III is very important for gold. All known gold(III) complexes are diamagnetic with a low-spin  $5d^8$  electron configuration, and the vast majority of these compounds have the four coordinate square-planar stereochemistry.

#### 2.3.4 UV-Vis spectroscopy of gold complexes

The Au(I) ion in linear gold(I) complexes has a closed  $5d^{10}$  electron configuration. Hence, the frontier  $5d$  orbitals are filled, followed by empty  $6s$  and  $6p$  orbitals. Thus, ligand field transitions ( $d-d$ ) are not possible for gold(I). The electronic absorption spectra of gold(I) complexes have high energy bands and these are generally assigned as ligand-to-metal charge-transfer (LMCT) transitions [29, 30]. Measuring electronic spectra for the gold(I) complexes encounter experimental difficulties because dihalo complexes are unstable with respect to disproportionation. Hence, our interest will focus on the electronic spectra of the square planar gold(III) complexes. Figure 2.4 shows a qualitative molecular orbital energy level diagram<sup>2</sup> for a square-planar gold(III) complex [27, 31]. Quantum chemical molecular orbital calculations showed that the order of  $d$ -orbital energies is  $d_{x^2-y^2} > d_{xy} > d_{xz} > d_{yz} > d_{z^2}$  [31, 32]. Since Au(III) has a  $d^8$  electronic configuration, all the  $5d$  orbitals are double occupied in the ground state except the  $d_{x^2-y^2}$ .

<sup>2</sup> Appendix A gives more information about constructing a molecular orbital energy level diagram by using group theory. Quantum mechanical calculations however are always needed to know the energy levels of this diagram.

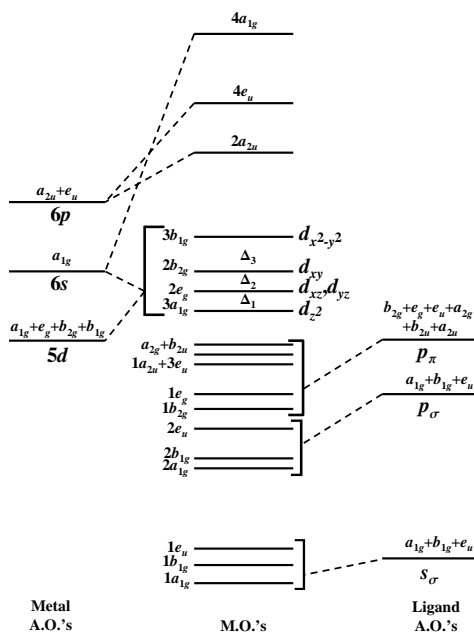


**Fig. 2.4:** Qualitative Molecular orbital energy levels for a square-planar gold(III) complex.

Three ligand-field orbital splitting parameters ( $\Delta_1$ ,  $\Delta_2$  and  $\Delta_3$ ) are illustrated in Figure 2.4 to define the  $d$  orbital splitting in the complexes. Ligand field transitions occur, but are usually weak bands at low energy. Examples of electronic absorption spectra from the commercially available gold salts Hydrogen tetrachloroaurate(III), trihydrate ( $\text{H}[\text{AuCl}_4] \cdot 3\text{H}_2\text{O}$ , Acros organics) and Hydrogen tetrabromoaurate(III) hydrate ( $\text{H}[\text{AuBr}_4] \cdot x\text{H}_2\text{O}$ , Acros organics) dissolved at concentrations of  $10^{-5}$  M in methanol can be seen in Figure 2.5. Both  $[\text{AuCl}_4]^-$  and  $[\text{AuBr}_4]^-$  show two strong bands in the UV. The band at lower wavelength (which we will assign  $\lambda_1$ ) is more or less seven times more intense than the other ( $\lambda_2$ ). The bands of the bromo complex are located at longer wavelengths than those of the chloro complex. The high extinction coefficients indicate that the electron transfer bands seen in the UV-Vis spectra are not ligand field transitions within the metal  $d$  shell, but correspond to ligand to metal charge transfer transitions [30, 33]. Furthermore, a shift to longer wavelengths in bromo (lower ionization potential) over chloro is then expected because ligand-to-metal charge transfer bands move to lower energy along the series

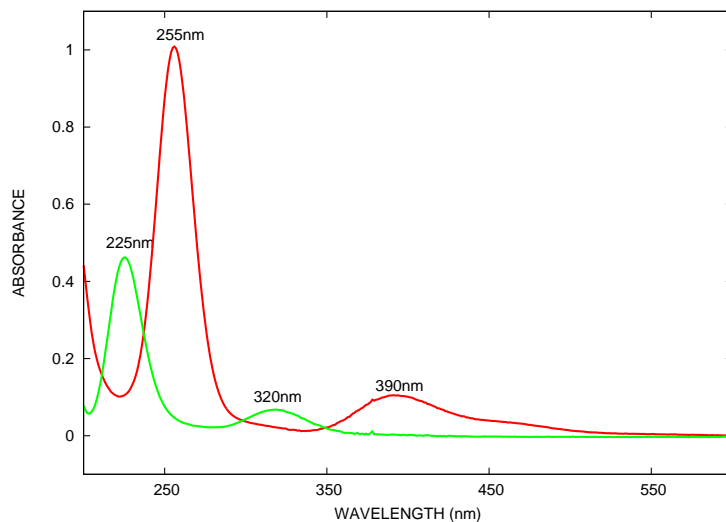


**Fig. 2.5:** UV-VIS absorption spectra of  $10^{-5}$  M  $\text{HAuCl}_4$  (green line) and  $10^{-5}$  M  $\text{HAuBr}_4$  (red line) dissolved in methanol.

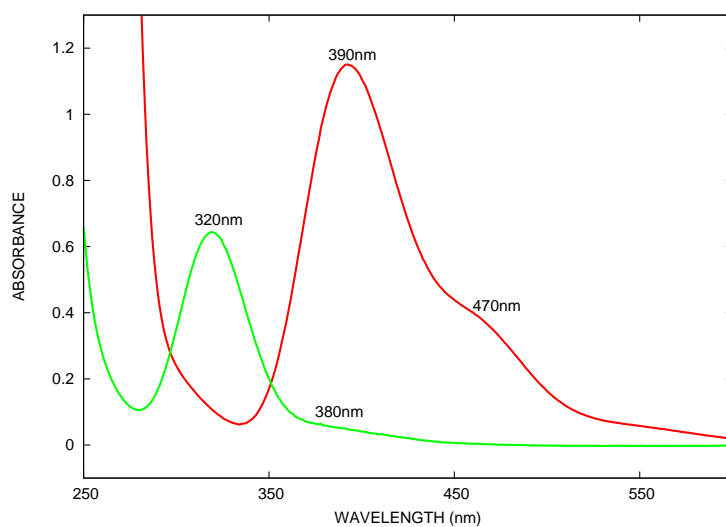


**Fig. 2.6:** UV-VIS absorption spectra of  $10^{-4}$  M  $\text{HAuCl}_4$  (green line) and  $10^{-4}$  M  $\text{HAuBr}_4$  (red line) dissolved in methanol.

$X = \text{Cl} > \text{Br} > \text{I}$  as it becomes progressively easier to oxidize the halide. However, Figure 2.6 shows UV-Vis spectra from higher concentration of the gold salts ( $10^{-4}$  M) in methanol. It can be clearly seen that there exists a shoulder on the tail of  $\lambda_2$  in the spectra of  $[\text{AuCl}_4]^-$  and  $[\text{AuBr}_4]^-$  at 380 nm and 470 nm respectively. These shoulders possibly represent ligand-field transitions, but are almost completely obscured by the more intense LMCT bands.

The identification of  $[\text{AuBr}_4]^-$  is crucial in this research work as will be explained in the Results & Discussions.

## 2.4 Colloid Stability

The colloidal gold systems in our study are typical examples of lyophobic colloids. In contrast to lyophilic colloids (e.g. proteins), which are thermodynamically stable, the Gibbs free energy of the lyophobic colloidal system is at a minimum when the particles are condensed together into one large crystal. A “stable” lyophobic colloid is stabilized kinetically by the presence of a repulsive energy barrier which prevents the particle collisions to result in actual contacts. In general there are two mechanisms in which the aggregation can be avoided:

- (a) an either positive or negative electric charge can be given to the particles and if the particles have the same charge, they repel one another when they approach;
- (b) the particles can be coated with an adsorbed layer that prevents their close approach.

The first mechanism is referred to as *electrostatic stabilization* and the second mechanism as *steric stabilization*. Both mechanisms will be discussed in this section. A system is colloidal unstable if the collisions of the particles result in the formation of aggregates, which is called coagulation.

### 2.4.1 Electrostatic forces and electrical potential

The fundamental law of electrostatic theory is Coulomb's law which states that the force  $F$  between two charges  $q_1$  and  $q_2$ , separated by a distance  $r$  takes the form

$$F = \frac{q_1 q_2}{4\pi\epsilon r^2} \quad (2.3)$$

where  $\epsilon = \epsilon_0 \epsilon_r$  is the permittivity with  $\epsilon_0$  the permittivity of a vacuum or free space and  $\epsilon_r$  the relative permittivity.

The work necessary to bring two charges together from infinity to the distance  $r$  is

$$W(r) = - \int_{\infty}^r F dr = \frac{q_1 q_2}{4\pi\epsilon r} \quad (2.4)$$

For charges of the same sign,  $W(r)$  is positive and the interaction is repulsive. If the charges have opposite sign, the interaction is attractive.

Consider for a moment that  $q_2$  is the unit electrical charge and that the charge  $q_1$  is isolated in space. The charge  $q_1$  produces an electric field at a point  $r$ . The quantity of work necessary to bring a unit electrical charge  $q_2$  from infinity to a distance  $r$  from  $q_1$  is defined as the *electrical potential*  $\psi$  at  $r$  due to the charge  $q_1$ . Mathematically, the electric potential can be written as

$$\psi = \frac{q_1}{4\pi\epsilon r} \quad (2.5)$$

The force involved in bringing the charge  $q_2$  within a distance  $r$  of  $q_1$  is then simply  $q_2\psi$ .

### 2.4.2 The electric double layer surrounding the metal particles

Metal particles in colloidal systems often carry an electric charge on their surfaces. In the standard citrate reduction gold sol, the gold particles have a negative charge as shown by their migration in the electric field toward the positive electrode [34]. This negative charge is due to strongly adsorbed citrate ions and "free" chloride ions. The particles are then balanced by loosely bound sodium cations to make the overall solution neutral. The charge on the gold particles can also be made positive

by passing the colloid through an ion exchange column by treating the solution with low molecular weight N-hexyl pyridinium polyethylene bromide. The positively charged polymer is strongly adsorbed on the gold giving it a positive charge and this is neutralized by loosely bound negative bromide counter ions [35]. This can be theoretically described by the double layer theory.

The theory of colloidal double layers is mostly built upon theoretical models which were developed to explain the electrical properties of the dropping mercury electrode double layer [24]. The earliest theoretical studies of the behavior of an elec-

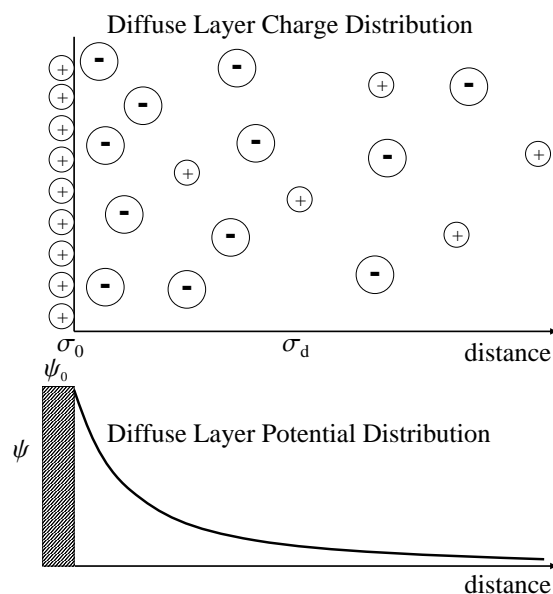


**Fig. 2.7:** A schematic representation of the Gouy-Chapman model illustrating the distribution of ions in the diffuse electrical double layer around a charged colloidal particle. Both the charge distribution and the potential decay near the surface are shown.

trified interface were made by Helmholtz in 1879 [36]. However, the Helmholtz model was unrealistic and in 1947 Grahame incorporated and modified the ideas of Helmholtz, Stern, Gouy and Chapman [37]. Figure 2.7 shows schematically the Gouy-Chapman model explaining what the electrostatic potential  $\psi$  in the vicinity of a positively charged particle is expected to look like. At the charged particle surface there is an excess of ions of one sign and in the solution there is an excess of ions of the opposite sign. The concentration of these counterions (ions with op-



positive sign) is greater close to the surface while the concentration of the co-ions (ions with the same sign as the charged surface) is less. This system of a charged surface together with the unequal concentration counterions and co-ions is called the *diffuse electrical double layer*. The counterions form a diffuse layer around the particle because on one hand they are attracted to the surface by electrostatic forces, but on the other hand they also move away from the surface to the solution by diffusion. In Figure 2.7 the electric potential slowly decays to zero as the distance from the particle surface toward the bulk solution becomes larger. In the more elaborate

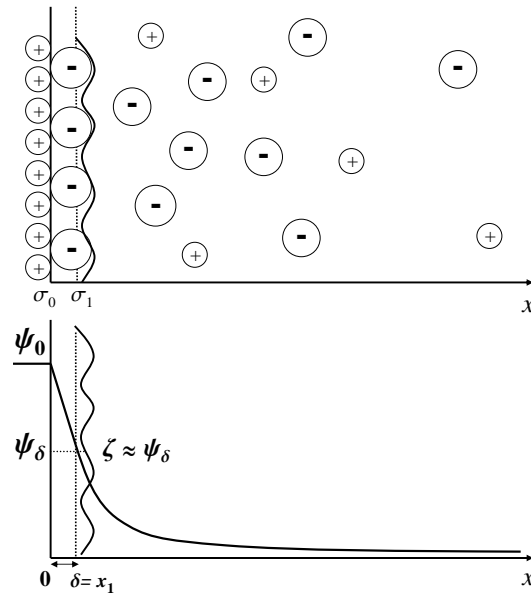


**Fig. 2.8:** A schematic representation of the electrical double layer illustrating the idea of a Stern plane or Helmholtz layer in which some ions are bound at a well-defined distance  $\delta$  from the surface.

theory, proposed by Stern (1924), some of the counterions are strongly absorbed to form a plane of bound countercharge lowering the electric potential immediately adjacent to the particle surface. This region is usually called the *Stern plane* or *Helmholtz layer*. It is composed of both strongly polarized water molecules and desolvated ions and can be represented by a surface charge concentrated in a plane at a small distance  $\delta$  from the actual surface charge on the wall as can be seen in Figure 2.8. The diffuse layer now starts at  $\delta = x_1$  where the potential is  $\psi_\delta$ . The

relative permittivity between the surface and the Stern plane is  $\varepsilon_1$  and has a value between 2 and 6 compared with 78 in bulk water [24]. This drastic decrease is due to the loss of rotational polarization for the aligned water molecules. The distance of the ions from the surface is approximately  $3 \text{ \AA}$  and therefore the surface charge and countercharge may be treated as a parallel condenser with a capacitance per unit surface area given by

$$K_I = \frac{\sigma_0}{\psi_0 - \psi_\delta} = \frac{\varepsilon_1 \varepsilon_0}{\delta} \quad (2.6)$$

where  $\varepsilon_1 \varepsilon_0$  is the permittivity of the layer and  $\sigma_0$  is the surface charge density. The potential at the distance  $\delta = x_1$  is reduced to

$$\psi_\delta = \psi_0 - \frac{\sigma_0}{K_I} = \psi_0 - \frac{\sigma_0 \delta}{\varepsilon_1 \varepsilon_0} \quad (2.7)$$

This Stern plane is usually close to the *shear* plane which is also visualized in Figure 2.8 and the potential at this plane is the observed zeta potential  $\zeta$ , measured by

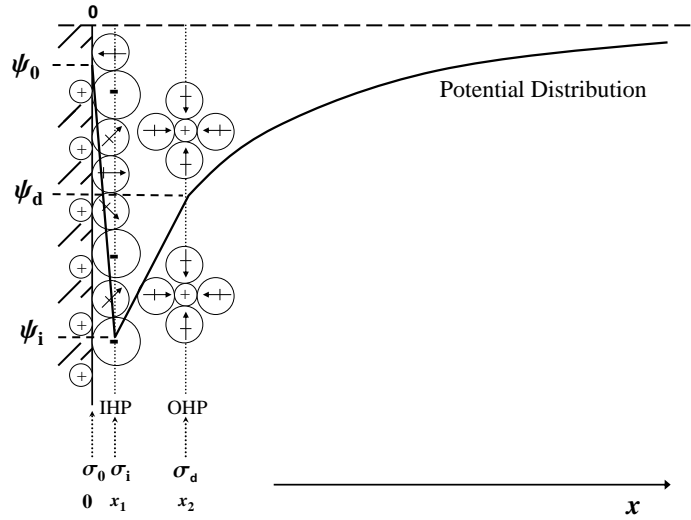


**Fig. 2.9:** A schematic representation of the Gouy-Chapman-Stern-Grahame model of the electrical double layer. The outer Helmholtz plane (OHP) and inner Helmholtz plane (IHP) are shown. The potential distribution at an interface shows the idea of superequivalent adsorption including a reversal of surface charge.

electrophoresis.

The ions adsorbed electrostatically at the Stern plane do normally not neutralize the surface charge completely. The adsorbed countercharge can exceed the real surface charge if there is a chemical driving energy for adsorption reversing the overall charge on the particle. This can be realized with polyelectrolytes superadsorbing colloidal particles [24]. The potential distribution is shown in Figure 2.9 where the potential changes sign before decaying slowly to zero in the bulk solution. The anions are shown unhydrated on the side near the wall, while the cations are hydrated. Water dipoles are expected to be oriented to some extent depending on the charge of the particle and the perturbing effect of the specifically adsorbed anions [38]. The plane where the diffuse layer begins is now called the outer Helmholtz plane (OHP)<sup>3</sup>. This is at a distance  $x_2$  and due to the finite size of the ions and their hydration shells it is the distance of closest approach of the solvated ions to the plane  $x_1$ , being the inner Helmholtz plane (IHP). The potential at the plane  $x_2$  effectively orientates the other ions in solution to build-up the diffuse layer of counterions around the particle.

### 2.4.3 Mathematical derivation of the Diffuse Layer

A first approximative theory for the electro-chemical double layer was given by Debye and Hückel [39]. The computation of the average charge distribution and a corresponding electric potential function was done on the basis of simplifying assumptions. One assumption for example is that the ions are point charges of negligible dimensions. With Poisson's equation the electric potential in every point of space charge in the diffuse layer can be calculated

$$\Delta\psi = -\frac{\rho}{\varepsilon} \quad (2.8)$$

where  $\psi$  is the electrical potential;  $\rho$  the charge density,  $\varepsilon$  the dielectric constant of the medium and  $\Delta$  the Laplace operator  $\Delta = \frac{\partial^2}{\partial x^2} + \frac{\partial^2}{\partial y^2} + \frac{\partial^2}{\partial z^2}$  for the use in three

---

<sup>3</sup> Note that this is the same as the Stern Plane.

dimensions. In one dimension this equation reduces to

$$\frac{\partial^2 \psi}{\partial x^2} = -\frac{\rho}{\varepsilon} \quad (2.9)$$

The Poisson equation describes the decay of  $\psi(x)$  in function of the charge density  $\rho(x)$ . In order to take the thermal motion of the ions into account, the theory makes the implicit assumption that the average concentration of these ions at a given point can be calculated from the average value of the electric potential at the same point with the aid of the Boltzmann's theorem. At a temperature  $T$ , the Boltzmann distribution is given as

$$n = n_0 \exp(-\Delta G/kT) \quad (2.10)$$

When applied to the situation involving charged particles and Coulomb's law (Eq. 2.3), Equation 2.10 predicts that if there exists a negative electrical potential  $\psi$  at some point in an electrolyte solution, in the region of that point the concentration of positive charges is given by

$$n_+ = n_0 \exp(-v_+ e \psi / kT) \quad (2.11)$$

where  $v_+$  is the valency of the positive ions and  $n_0$  is the concentration of the positive ions in a region where  $\psi = 0$ . A similar expression can be written for the negative ions in the solution

$$n_- = n_0 \exp(v_- e \psi / kT) \quad (2.12)$$

The full expression for  $\rho$  can now be written as

$$\rho = ve(n_+ - n_-) = -2nve \sinh(v e \psi / kT) \quad (2.13)$$

In the Debye-Hückel approximation it is assumed that the electric potential is so small that  $v e \psi / kT \ll 1$  and  $\exp(v e \psi / kT)$  may be replaced by  $1 + v e \psi / kT$ . The expression for the charge density then becomes

$$\rho = -2nv^2 e^2 \psi / kT \quad (2.14)$$

These expressions for the charge density may be inserted in Equation 2.9 to obtain the fundamental differential equation or the *Poisson-Boltzmann equation*

$$\frac{d^2\psi}{dx^2} = \frac{2nve}{\varepsilon} \sinh(ve\psi/kT) \quad (2.15)$$

For small values of  $\psi$  this equation simplifies to

$$\frac{d^2\psi}{dx^2} = \frac{2nv^2e^2}{\varepsilon kT} \psi = \kappa^2 \psi \quad (2.16)$$

Equation 2.16 is the well known starting point in the theory of Debye and Hückel for strong electrolytes where  $\kappa$  is the Debye-Hückel parameter and is called the double layer thickness

$$\kappa^2 = \frac{2nv^2e^2}{\varepsilon kT} \quad (2.17)$$

For the double layer in colloid systems we should preferably apply the complete Poisson-Boltzmann equation 2.15 (Appendix B). A first integration of Equation 2.15 with the appropriate boundary conditions gives

$$\frac{d\psi}{dx} = \frac{-2\kappa kT}{ve} \sinh \frac{ve\psi}{2kT} \quad (2.18)$$

The second integration gives for the potential  $\psi(x)$

$$\tanh \left[ \frac{ve\psi(x)}{4kT} \right] = \tanh \left[ \frac{ve\psi_0}{4kT} \right] e^{-\kappa x} \quad (2.19)$$

Equation 2.19 is the solution for the approximation of a flat double layer around a colloid particle. This is valid if  $\kappa a \gg 1$  (with  $a$  the radius of the colloid particle). However, for nanosized particles with diameters less than 100 Å, the assumption of flat double layers is no longer accurate<sup>4</sup> and integration of Equation 2.15 should be solved for the case of spherical symmetry [40]. Hence, the linearization and integration of Equation 2.15 for the case of spherical symmetry yields

$$\psi(r) = \psi_0 \frac{a}{r} \exp[-\kappa(r-a)] \quad (2.20)$$

<sup>4</sup> At 0.1 mM NaNO<sub>3</sub> for example, the Debye length is 300 Å and  $\kappa a \sim 0.3$  [24].

**Tab. 2.2:** Solutions of the Poisson-Boltzmann equation for nanoparticles.

	Small $\kappa a$	Large $\kappa a$
Low potentials	$\psi(r) = \psi_0 \frac{a}{r} \exp[-\kappa(r-a)]$	$\psi(x) = \psi_0 \exp(-\kappa x)$
High potentials	$\Delta\psi = \frac{2nve}{\varepsilon} \sinh(v\psi/kT)$	$\tanh\left[\frac{v\psi(x)}{4kT}\right] = \tanh\left[\frac{v\psi_0}{4kT}\right] e^{-\kappa x}$
	where $\kappa^2 = \frac{2nv^2e^2}{\varepsilon kT}$	

This equation is useful in the description of colloidal systems with low surface potential and as a comparison standard for more exact solutions [40]. However, a surface potential  $< 25$  mV is insufficient to prevent particle coalescence. Moreover, it does not provide accurate results for stable colloids with high surface potentials and the potential distribution then has to be solved numerically. The different solutions of the Poisson-Boltzmann equation for different regimes are summarized in Table 2.2.

#### 2.4.4 Nanoparticle Stability - The DVLO theory

The electrical double layer plays an important role in the stability of nanoparticles preventing them to coagulate into larger aggregates which is an undesirable process because it changes the properties of the nanoparticles. Furthermore, if nanoparticles form aggregates it is difficult to redisperse them to retain their individuality [40]. The forces leading to coalescence of the particles in a colloid system is caused by the Van Der Waals-London attractive forces acting between their surfaces. The nanoparticle stability thus depends on the total interaction between the double layers (repulsion potential energy  $V_R$ ) and the Vander Waals-London forces (attraction potential energy  $V_A$ ). The repulsive potential energy rises exponentially when particles are approaching, reaching a finite value when they are in contact. However, at the same time, the attraction potential energy increases in magnitude without limit as the particles approach. The attraction always dominates over the

repulsion at both large and small separations. The sum of these two potential energies is referred to as the Derjaguin-Landau-Verwey-Overbeek (DLVO) theory [40] and is shown schematically in Figure 2.10. A colloidal system is stable if the repul-

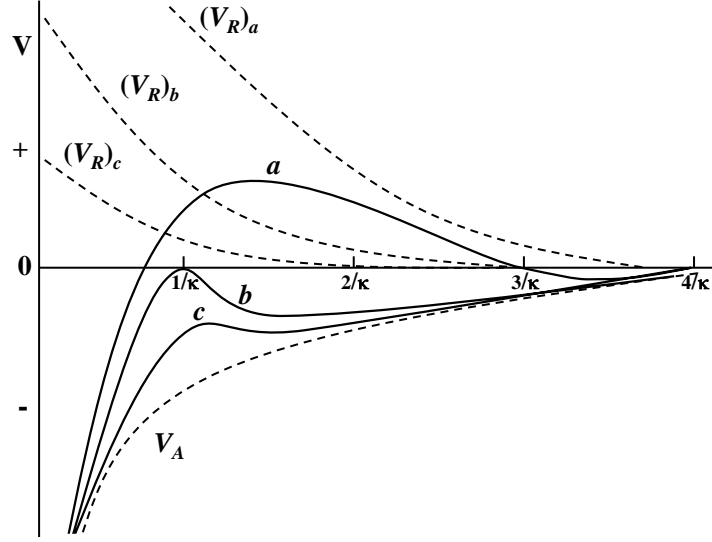


**Fig. 2.10:** A schematic representation of the DLVO theory showing the total potential energy of repulsion for a stable (a), marginal (b) and unstable (c) colloidal system where  $|\zeta|_a > |\zeta|_b > |\zeta|_c$ .

sion dominates over the attraction at an intermediate separation. This meta stability or kinetic stability of the colloidal system is determined by the width and the height of the potential barrier.

For small spherical particles with radius  $a$  ( $\kappa a \approx 1$ ) the electrostatic repulsion energy at small potentials (using the Debye-Hückel linearization) must be expanded in spherical harmonics and the resulting expressions for  $V_R$  are rather complicated. However, an estimate of the repulsion energy can be obtained from the following expression [39, 40]

$$V_R = \frac{4\pi\epsilon\psi_0^2 a \exp(-\kappa H_0)}{2 + H_0/a} \quad (2.21)$$

with  $H_0$  being the shortest distance between the two spheres and the other symbols defined previously.

The electrostatic attraction energy on the other hand is given by [39, 40]

$$V_A = -\frac{A}{6} \left( \frac{2}{s^2 - 4} + \frac{2}{s^2} + \ln \frac{s^2 - 4}{s^2} \right) \quad (2.22)$$

where  $A$  is commonly called the Hamaker constant for the metal-water-metal system and  $s = r/a$  with  $r$  being the center-to-center distance. Putting  $r = 2a + H_0$  and assuming that  $H_0 \ll a$ ,  $V_A$  can be approximated

$$V_A = -\frac{Aa}{12H_0} \quad (2.23)$$

indicating that the free energy of attraction decays very slowly.

Hence, the total potential energy of interaction between two spherical particles can be written

$$V_T = V_R + V_A = \frac{4\pi\epsilon\psi_0^2 a \exp(-\kappa H_0)}{2 + H_0/a} - \frac{Aa}{12H_0} \quad (2.24)$$

#### 2.4.5 Steric Stabilization

The stability of lyophobic colloidal dispersions can be enhanced by the addition of soluble lyophilic material (protective agents) adsorbing or otherwise attaching to the particle surfaces leading to a repulsion [41]. These steric stabilizers are usually amphipathic surfactants consisting of at least two chemically bound components, one being soluble in the dispersion medium while the other, being insoluble, attaches the soluble part to the colloidal particles [36]. In Equation 2.24 an extra structural term ( $V_S$ ) must be included to describe the total potential energy of interaction for sterically stabilized colloidal systems:

$$V_T = V_R + V_A + V_S \quad (2.25)$$

The Van Der Waals attraction between the colloidal particles is usually relatively small as can be seen in a schematically potential energy diagram in Figure 2.11 where the potential barrier characteristic for the metastability of electrostatically stabilized dispersions is minimized. The less important contribution of the Van Der Waals attraction in inducing aggregation of sterically stabilized dispersions is



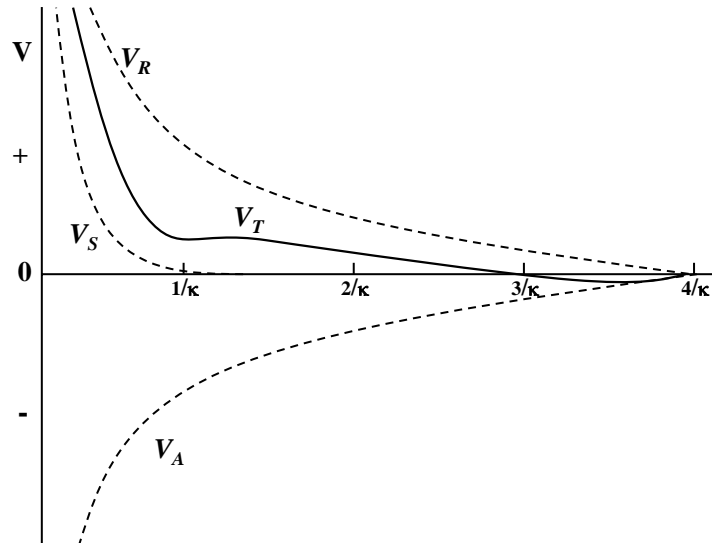


**Fig. 2.11:** A schematic representation for sterically stabilised particles together with the electric double layer repulsion ( $V_T = V_R + V_S$ ).

in sharp contrast with its role in causing coagulation in electrostatically stabilized dispersions. Thus, steric stabilization depends solely on the properties of the adsorbed or attached material and can be described thermodynamically. When two particles approach, the adsorbed molecules experience a loss of entropy in the narrow gap between the two particles and secondly, the increased concentration of the adsorbate in the gap causes an increase in free energy. Both the loss of entropy and increase in free energy result in a repulsion of the particles [42].

Steric stabilization has several advantages compared to electrostatic stabilization. It protects hydrophobic colloids against aggregation by electrolytes and it is equally effective in both aqueous and non-aqueous dispersion media. This contrasts strongly with the electrostatically stabilized dispersions being ineffective in non-polar dispersion media and where the addition of electrolyte causes a coagulation.

## 2.5 Optical properties of small metal particles

Metal colloids exhibit colors that often differ from the color of their bulk materials. For example, a dispersion of gold colloids is red and of silver colloids yellow. The origin of these color changes are explained by surface plasmon resonances, which are electrons oscillating collective in response to an applied field. For example, when a metal particle is decreased below the wavelength of visible light and when the visible light has a frequency close to that of the oscillating electrons, then the surface plasmon resonance absorbs energy. In this section a theoretical understanding of the optical response of small metal particles shall be given. The surface plasmon resonances are explained by the Lorentz-Drude-Sommerfeld Model which gives us an intuitive basis for the understanding of free electrons moving in response to an electric field. Furthermore, the absorption of light by metal colloids is explained by the application of the Mie theory. The Mie theory, which is tedious and lengthy, will not be derived as this can be found elsewhere in the original work of Mie [13] and in the book of Bohren and Hoffman [43].

### 2.5.1 Surface Plasmon Resonances

The optical response of metal colloids to an electric field of incident wavelength, with radius  $r \ll \lambda$ , is schematically shown in Figure 2.12. In the *quasi-static regime* the positive charges in the metal colloids are assumed to be immobile, while the negative charges (the conduction electrons) are allowed to move under the influence of an external field. Hence, when metal colloids are placed in an electric field, a displacement of the negative charges from the positive ones occurs. These collective resonances from the negative electrons are denoted as Mie resonances or surface plasmon resonances with the term *surface* coming from the main effect producing the restoring force being the surface polarization [44].

The optical properties of metal colloids are described by the optical material function or the dielectric function  $\varepsilon(\omega)$ . For metal colloids with a diameter larger than 10 nm, the dielectric functions have the values of the bulk material. For smaller metal colloids, the dielectric functions vary as a function of particle size and for sub-nm nanoclusters, quantum mechanical methods have to be applied as single

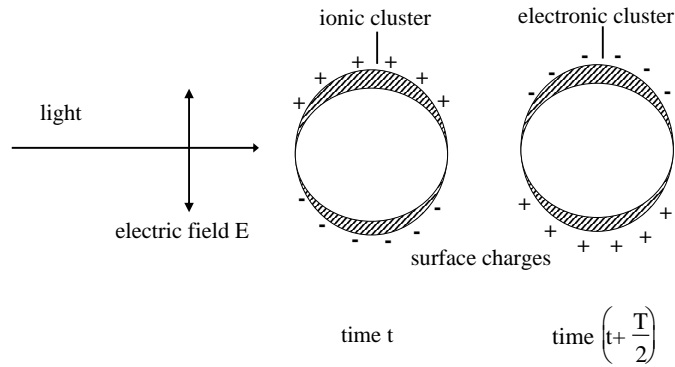


**Fig. 2.12:** A schematic representation illustrating the optical response of a metal colloid to an electric field (an incident light wave) leading to a dipolar surface plasmon. The negative charges (the conduction electrons) move under the influence of the external field [44].

electron excitations can occur [44]. Sub-nm nanoclusters are too small to have a continuous density of states. Therefore, the plasmon resonance characteristic for larger free-electron metal nanoparticles, is absent for very small metal clusters [45].

### 2.5.2 The Lorentz-Drude-Sommerfeld Model

Lorentz and Drude developed a classical theory of optical properties in which the electrons and ions of matter were treated as simple harmonic oscillators subject to the driving force of applied electromagnetic fields [43]. The Lorentz-Drude-Sommerfeld model is very useful in understanding the collective oscillations of the free electrons. According to this theory, the electron within the metal is assigned its free mass  $m_e$  and some velocity  $v$ . The electron is accelerated by an incident radiation, which is the electric field

$$E = E_0 \exp(-i\omega t) \quad (2.26)$$

The electric field is time harmonic with frequency  $\omega$ . The electron in the metal, while being accelerated, experiences collisions with the lattice, with other electrons, and with impurities at a rate proportional to its velocity. These collisions immediately reduce its velocity back to zero and the average velocity of the electron can then be calculated to be roughly  $eE\tau/m_e$ , where  $\tau$  is the time between collisions. The equation of motion is ( $x$  is the displacement of the electron)

$$m_e \frac{\partial^2 x}{\partial t^2} + \gamma \frac{\partial x}{\partial t} = eE_0 \exp(-i\omega t) \quad (2.27)$$

with  $\gamma (= \tau^{-1})$  representing the phenomenological damping due to collisions. Equation 2.27 is similar to the equation of motion for a simple harmonic oscillator without a restoring force  $k$ . The solution to Equation 2.27 is composed of a transient part and an oscillatory part (the steady state solution). The transient part dies away because of damping and we are only interested in the steady-state solution

$$x = \frac{eE/m_e}{-\omega^2 - i\omega_d\omega} \quad (2.28)$$

where  $\omega_d = \gamma/m_e$  is the damping frequency of the electron. It must be noted that this treatment is for one electron only and if there are  $N$  free electrons per unit volume, this creates a polarization  $P = Nex$ , having the electrons oscillating at the driving frequency of the radiation. Furthermore, to obtain the optical response of a collection of free electrons from Equation 2.27, we consider isotropic media where  $P \parallel E$  with the polarization  $P$  connecting to the dielectric function  $\varepsilon(\omega)$  by the definition

$$P = \chi \varepsilon_0 E = \varepsilon_0 (\varepsilon - 1) E \quad (2.29)$$

where  $\chi$  is the electric susceptibility. From Equation 2.29 it is common to express the dielectric function  $\varepsilon(\omega)$  in terms of this electric susceptibility to give  $\varepsilon(\omega) = 1 + \chi^{DS}(\omega)$  where  $\chi^{DS}(\omega)$  denotes the free-electron Drude-Sommerfeld susceptibility [44]. Inserting Equation 2.29 into Equation 2.28 yields the dielectric function  $\varepsilon(\omega) = \varepsilon_1(\omega) + i\varepsilon_2(\omega)$  for free electrons per unit volume

$$\varepsilon(\omega) = 1 - \frac{Ne^2/m_e\varepsilon_0}{\omega^2 + i\omega_d\omega} = 1 - \frac{\omega_p^2}{\omega^2 + i\omega_d\omega} \quad (2.30)$$

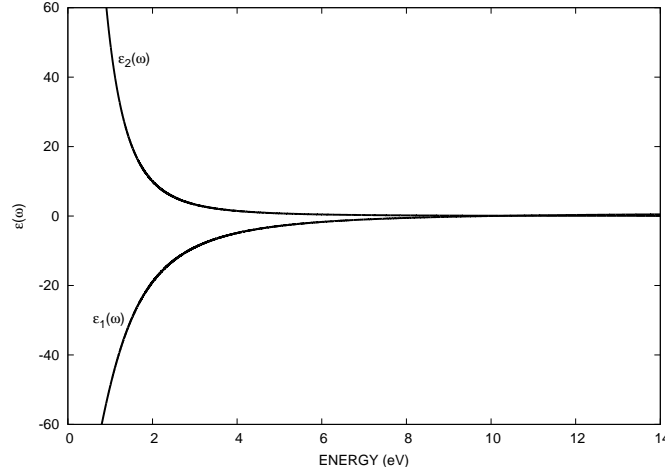


**Fig. 2.13:** The real and imaginary parts of the dielectric function of a simple free electron system (Drude Model) as a function of frequency ( $\omega$ ) in eV for values  $\omega_p = 10$  eV and  $\omega_d = 1$  eV .

where  $\omega_p = (Ne^2/m_e\epsilon_0)^{1/2}$  is the Drude plasma frequency in terms of  $N$ , the concentration of free electrons in the metal [46]. The real and imaginary parts of the dielectric function may then be written as [43]

$$\begin{aligned}\epsilon_1(\omega) &= 1 - \frac{\omega_p^2}{\omega^2 + \omega_d^2} \\ \epsilon_2(\omega) &= \frac{\omega_p^2\omega_d}{\omega(\omega^2 + \omega_d^2)}\end{aligned}\quad (2.31)$$

This is the *Drude model* for optical properties of a free-electron metal and can be considered as the classical model of a metal where free electrons move against a fixed background of immobile positive ions. The real and imaginary parts of the dielectric function for a free-electron metal as a function of frequency are shown in Figure 2.13 for  $\omega_p = 10$  eV and  $\omega_d = 1$  eV. All the frequencies of the oscillating electrons are out of phase with the applied field which is illustrated in Figure 2.13 where  $\epsilon_1(\omega)$  is negative over a wide range. Furthermore,  $\epsilon_1(\omega)$  is negative in the frequency regime below the bulk plasma frequency ( $\omega_p$ ) of a metal and this is due to the fact that the polarization field is larger than and opposite in sign to the ap-

plied field.

The Drude model is the optical response of a collection of “free” electrons without a restoring force. In a chemical bond, the displacement of the electron sets up a restoring force due to the positive nuclear charge on the ion, which “pulls” the electron back to the equilibrium bond length. In a metal on the other hand, the nuclear charge is shielded by the other neighboring conduction electrons, so the electrons do not experience a restoring force. However, for small metal particles the dipole which is created by the electric field of the incident light wave, sets up a surface polarization charge and this acts as a restoring force for the free electrons. To see what effect this will have, we add to Equation 2.27 a linear restoring force determining the eigenfrequency of the “oscillating” electron. The equation of motion is then

$$m_e \frac{\partial^2 x}{\partial t^2} + \gamma \frac{\partial x}{\partial t} + kx = eE_0 \exp(-i\omega t) \quad (2.32)$$

and we are again only interested in the steady-state solution to Equation 2.32 being

$$x = \frac{eE/m_e}{\omega_0^2 - \omega^2 - i\omega_d\omega} \quad (2.33)$$

where  $\omega_0^2 = k/m_e$  is the resonance frequency of the oscillator and  $\omega_d = \gamma/m_e$  the damping frequency of the electron. For a nonzero  $\omega_0$ , there is a frequency whereby  $x$  is a maximum, close to  $\omega_0$ . Furthermore, if  $\omega_d \neq 0$ , the proportionality factor between  $x$  and  $E$  is complex. Hence, the displacement and field are generally not in phase. The displacement is written as  $Ae^{i\phi} (eE/m_e)$  with  $A$  the amplitude and  $\phi$  the phase angle given by [43]

$$\begin{aligned} A &= \frac{1}{\sqrt{[(\omega_0^2 - \omega^2)^2 + \omega_d^2\omega^2]}} \\ \phi &= \tan^{-1} \frac{\omega_d\omega}{\omega_0^2 - \omega^2} \end{aligned} \quad (2.34)$$

Figure 2.14 shows the amplitude as a function of frequency in eV. The amplitude is at a maximum at  $\omega \simeq \omega_0$ , whereas the height of this maximum is inversely proportional to  $\omega_d$  and the width at half-maximum is proportional to  $\omega_d$ .

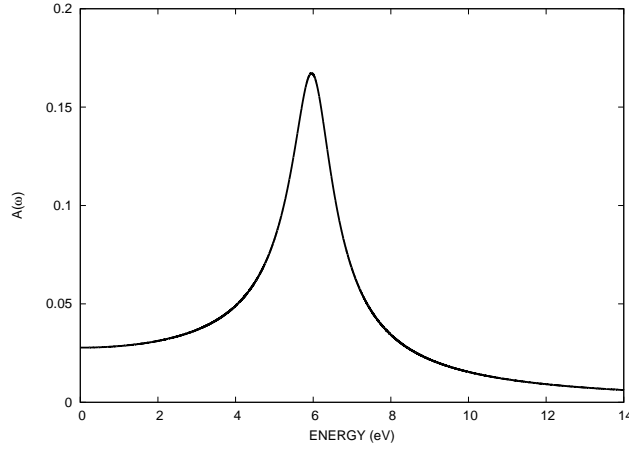


**Fig. 2.14:** The amplitude  $A$  of the one-oscillator (Lorentz) model as a function of frequency ( $\omega$ ) in eV with  $\omega_0 = 6$  eV and  $\omega_d = 1$  eV.

This treatment is again for one electron only and with  $N$  free electrons per unit volume a polarization  $P = Nex$  is created. Considering isotropic media where  $P \parallel E$ , the polarization  $P$  connects to the dielectric function  $\varepsilon(\omega)$  by inserting Equation 2.29 into Equation 2.33 yielding the dielectric function  $\varepsilon(\omega) = \varepsilon_1(\omega) + i\varepsilon_2(\omega)$  for a system of simple harmonic oscillators

$$\varepsilon(\omega) = 1 + \frac{Ne^2/m_e\varepsilon_0}{\omega_0^2 - \omega^2 - i\omega_d\omega} = 1 + \frac{\omega_p^2}{\omega_0^2 - \omega^2 - i\omega_d\omega} \quad (2.35)$$

$$= 1 + \frac{\omega_p^2(\omega_0^2 - \omega^2)}{(\omega_0^2 - \omega^2)^2 + \omega_d^2\omega^2} + i \frac{\omega_p^2\omega_d\omega}{(\omega_0^2 - \omega^2)^2 + \omega_d^2\omega^2} \quad (2.36)$$

where  $\omega_p$  is again the Drude plasma frequency in terms of  $N$ , the concentration of free electrons in the metal [46]. The real and imaginary parts of the dielectric function may now be written as [43]

$$\begin{aligned} \varepsilon_1(\omega) &= 1 + \chi' = 1 + \frac{\omega_p^2(\omega_0^2 - \omega^2)}{(\omega_0^2 - \omega^2)^2 + \omega_d^2\omega^2} \\ \varepsilon_2(\omega) &= \chi'' = \frac{\omega_p^2\omega_d\omega}{(\omega_0^2 - \omega^2)^2 + \omega_d^2\omega^2} \end{aligned} \quad (2.37)$$

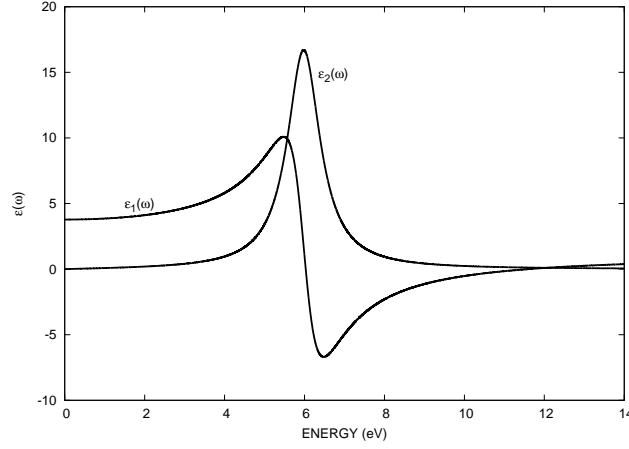


**Fig. 2.15:** The real and imaginary parts of the dielectric function of a harmonic oscillator as a function of frequency ( $\omega$ ) in eV for values  $\omega_p = 10$  eV,  $\omega_0 = 6$  eV and  $\omega_d = 1$  eV .

This is the *Lorentz model* for the optical properties of “free” electrons in a metal having a restoring force. Note that the Drude model can be easily obtained from Equation 2.37 by setting  $\omega_0$  equal to zero. The frequency dependence of the real and imaginary parts of the dielectric function as a function of frequency is shown in Figure 2.15 for  $\omega_p = 10$  eV,  $\omega_0 = 6$  eV and  $\omega_d = 1$  eV. This figure illustrates that  $\varepsilon_1(\omega)$  is negative around a certain absorption frequency  $\omega_0$ . Therefore, the Lorentz model can be used to explain intuitively the effect of surface plasmon resonances for small metal particles where the long-wavelength absorption by the bulk metal is condensed into a single, surface plasmon band.

### 2.5.3 Light Absorption by spherical Metal Colloids

The optical properties of a metal particle in terms of absorption and scattering cross sections  $\sigma_{\text{abs}}$  and  $\sigma_{\text{sca}}$  are related to the intensity loss of the incident light due to absorption or elastic scattering [44]. In practice, both absorption and scattering contribute, resulting in a total extinction cross section

$$\sigma_{\text{ext}} = \sigma_{\text{abs}} + \sigma_{\text{sca}} \quad (2.38)$$



The measured attenuation of a parallel beam of incident light with intensity  $I_0$ , over a path length  $x$  cm in a spectrophotometer is given by the Lambert-Beer law. For a colloidal solution containing  $N$  particles per unit volume, the transmitted light  $I(x)$  is

$$I(x) = I_0 e^{-N\sigma_{\text{ext}}x} \quad (2.39)$$

However, the Lambert-Beer law is usually expressed as [47]

$$A = \log_{10} \left( \frac{I_0}{I(x)} \right) = \frac{N\sigma_{\text{ext}}x}{2.303} \quad (2.40)$$

where  $A$  is the solution absorbance. The extinction cross section is calculated from *Mie* theory by series expansion of the involved fields into partial waves of different spherical symmetries [44]. For spherical particles with a complex dielectric function, embedded in a medium of dielectric function  $\varepsilon_m$ , the extinction cross section according to *Bohren* and *Huffman* [43], is written as

$$\sigma_{\text{ext}} = \frac{2\pi}{k^2} \sum_{n=1}^{\infty} (2n+1) \text{Re} \{a_n + b_n\} \quad (2.41)$$

where  $k = 2\pi\sqrt{\varepsilon_m}/\lambda$  [11].  $a_n$  and  $b_n$  are the scattering coefficients which are functions of the radius  $r$  and the wavelength  $\lambda$  in terms of Ricatti-Bessel cylindrical functions. However, when the size of the metal particle is much smaller than the wavelength of the exciting radiation ( $r \ll \lambda$ ), the effects of higher multipoles are neglected and only the first, electric dipole term is significant. Hence, the Mie formula (Equation 2.41) is simplified and given by [44, 48]

$$\sigma_{\text{ext}}(\omega) = 9 \frac{\omega}{c} \varepsilon_m^{3/2} V_0 \frac{\varepsilon_2(\omega)}{[\varepsilon_1(\omega) + 2\varepsilon_m]^2 + \varepsilon_2^2(\omega)} \quad (2.42)$$

with  $V_0 = 4/3\pi r^3$  the particle volume,  $\varepsilon_m$  the dielectric function of the embedding medium and  $\varepsilon(\omega)$  the dielectric function of the particle. Taking interband and core transitions into account, the real part of the dielectric function in the Drude model

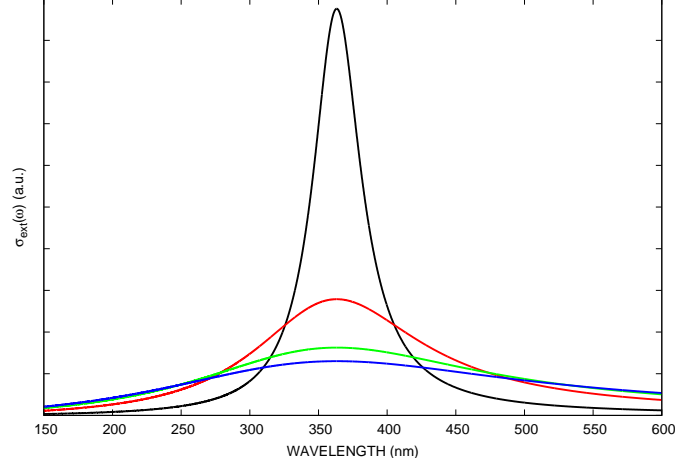


**Fig. 2.16:** Calculated surface plasmon absorption bands for typical values of silver colloids using the dipole approximation of the Mie theory (Equation 2.42) showing the effect of the damping parameter  $\omega_d$ . The damping frequencies in eV are 0.4 (black), 1.4 (red), 2.4 (green) and 3.0 (blue). Other parameters used in the calculation are  $\varepsilon^\infty = 5.0$ ,  $r = 4$  nm and  $\varepsilon_m = 1.77$  [11].

(Equation 2.30) can be rewritten as

$$\varepsilon_1(\omega) = \varepsilon^\infty - \frac{\omega_p^2}{\omega^2 + \omega_d^2}$$

with  $\varepsilon^\infty$  the high frequency dielectric constant. The cross section  $\sigma_{\text{ext}}(\omega)$  has a resonance at the frequency where the denominator  $[\varepsilon_1(\omega) + 2\varepsilon_m]^2 + \varepsilon_2^2(\omega)$  takes its minimum. When  $\varepsilon_2(\omega)$  is small, this condition is simplified to  $\varepsilon_1(\omega) = -2\varepsilon_m$ . Figure 2.16 shows calculated surface plasmon absorption bands using Equation 2.42 with typical silver parameters for several values of the damping parameter  $\omega_d$  [11]. The damping frequency is related to the mean free path of the conduction electrons,  $R_{\text{bulk}}$  and the velocity of the electrons at the Fermi energy  $v_f$  [11]

$$\omega_d = \frac{v_f}{R_{\text{bulk}}} \quad (2.43)$$

The parameter affecting  $\omega_d$  the most is the particle size. It can be seen from Equation 2.43 that when the particle size decreases,  $\omega_d$  increases, causing the band to

broaden and the maximum intensity to decrease.

#### 2.5.4 Size dependence of spherical metal nanoparticles on the plasmon absorption band

The Mie theory within the dipole approximation, which has been described in the previous section, has the advantage that it is conceptually easy to understand. Therefore, it is widely used to explain many experimental results [44]. However, there is no size dependence within this dipole approximation (Equation 2.42) except for a varying intensity due to the dependence of the volume  $V_0$  on the particle radius  $r$ . Furthermore, a strong dependence of spherical metal nanoparticles on the plasmon absorption bandwidth is experimentally observed [44,49]. The position of the plasmon absorption maximum ( $\lambda_{\max}$ ) is also affected with decreasing particle size although both a blue-shift and a red-shift have been observed [49]. The size effect on the plasmon absorption band was examined by Link *et al.* by studying colloidal gold nanoparticles with an average diameter between 9 and 99 nm [49]. The gold nanoparticles were prepared following the method introduced by Turkevich [15] and modified by Frens [17]. Figure 2.17 shows the absorption spectra of four different size gold nanoparticles where  $\lambda_{\max}$  of the plasmon absorption red-shifts with increasing particle diameter. Furthermore, it is seen that the plasmon absorption bandwidth decreases with increasing particle size and then increases again with a minimum for the 22 nm nanoparticles.

A modification to the Mie theory for small metal particles is the assumption that the dielectric function of the metal nanoparticles itself becomes size-dependent [ $\varepsilon = \varepsilon(\omega, r)$ ] and this size dependence is introduced as the diameter of the particle becomes smaller than the mean free path of the conduction electrons [50]. Moreover, this results in a size-dependent absorption cross section within the dipole approximation which is regarded as an *intrinsic size effect* [44]. The collision time  $\tau$  (or the relaxation time) for an electron is the average of the  $\tau_i$  caused by collisions with phonons, impurities and lattice-defects [49,50]

$$\gamma = \tau^{-1} = \sum_i (\tau_i)^{-1} \quad (2.44)$$

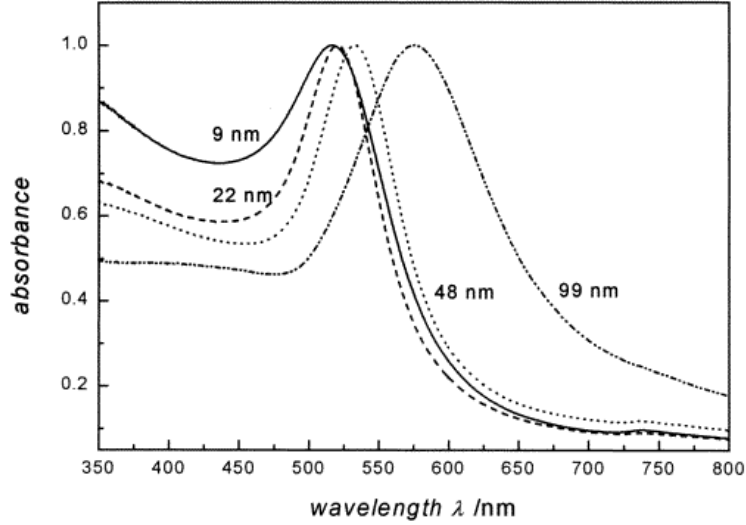


**Fig. 2.17:** UV-Vis absorption spectra of 9, 22, 48, and 99 nm gold nanoparticles in water taken by Link *et al.* [49]. The spectra are normalized at their plasmon absorption maxima, which are 517, 521, 533 and 575 nm respectively.

For small particles the surface acts as an additional collision process because now the size of the particles is comparable to the mean free path of the electrons and for very small particles these collisions of the conduction electrons with the particle surface dominate resulting in a reduced effective mean free path. The damping constant  $\gamma$  then depends on the particle radius  $r$  and is given by [49, 50]

$$\gamma(r) = \gamma_0 + \frac{A \cdot v_f}{r} \quad (2.45)$$

where  $\gamma_0$  is the bulk damping constant as given by Equation 2.44,  $v_f$  being the velocity of the conduction electrons at the Fermi energy and  $A$  describing the specific scattering processes [49].

However, for larger nanoparticles ( $r > 15$  nm) the extinction cross section is also dependent on higher-order multipole modes within the full Mie equation. Therefore the extinction spectrum is not only dominated by dipole absorption, but also by quadrupole and octopole absorption as well as scattering processes [49]. Higher oscillation modes depend explicitly on the particle size whereas the plasmon absorption is shifted to longer wavelengths and the bandwidth increases with increas-

ing particle size. Hence, the total plasmon band absorption is the superposition of all the contributing multipole oscillations peaking at different energies. The broadening of the plasmon band is usually attributed to retardation effects [44] although the increased line width can also be described as a result of the interactions between the dipole and the higher-order oscillatory motions of the electrons [49]. The behavior of the plasmon resonance is regarded as an *extrinsic size effect* when the size effect enters through the full Mie equation and when the complex dielectric function of the bulk material, being no longer size dependent, is used [44].

### 2.5.5 Light Absorption by Metal Nanorods

For rodlike nanoparticles the direction of the plasmon oscillation depends on the orientation of the particle axis with respect to the oscillating electric field of the incident light. This results in two plasmon absorptions, instead of one single plasmon band for spherical metal colloids, being the transverse resonance and the longitudinal resonance. This is shown schematically in Figure 2.18. The optical

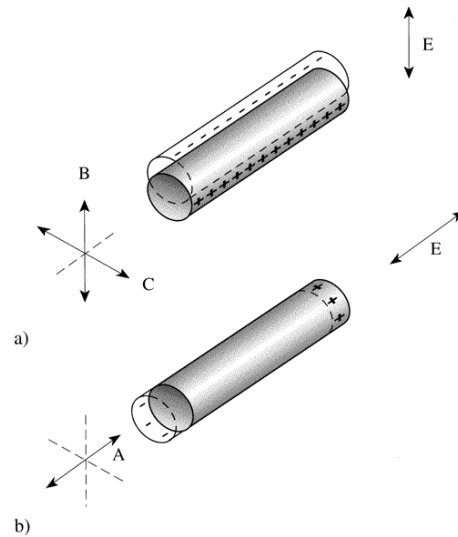


**Fig. 2.18:** Schematic representation illustrating the optical response of rodlike nano particles to an electric field  $E$ . Two oscillating modes can be possible: (a) the transverse oscillation along the  $B$  or  $C$  axis and (b) the longitudinal oscillation along the  $A$  axis [51].

properties of metal nanorods can be theoretically described using the Gans theory,

which is an extension of the Mie theory with a geometrical factor [51,52]. According to this theory, the extinction coefficient  $\kappa$  for  $N$  particles of volume  $V_0$ , within the dipole approximation is given by [53,54]

$$\kappa_{\text{ext}} = \frac{2\pi N V_0 \epsilon_m^{3/2}}{3\lambda} \sum_j \frac{\left(\frac{1}{P_j^2}\right) \epsilon_2}{\left[\epsilon_1 + \left(\frac{1-P_j}{P_j}\right) \epsilon_m\right]^2 + \epsilon_2} \quad (2.46)$$

whereby the  $P_j$  values are the depolarization factors to calculate the absorption of light by the nanorods for the three axes  $A$ ,  $B$ , and  $C$  as indicated in Figure 2.18. The  $B$  and  $C$  axes correspond to the particle diameter ( $d$ ), while the  $A$  axis represents the particle length ( $L$ ). The geometrical factors  $P_j$  for nanorods along the  $A$ ,  $B$ , and  $C$  axes are respectively

$$P_A = \frac{1-e^2}{e^2} \left[ \frac{1}{2e} \ln \left( \frac{1+e}{1-e} \right) - 1 \right] \quad (2.47)$$

$$P_B = P_C = \frac{1-P_A}{2} \quad (2.48)$$

with

$$e = \sqrt{1 - \left(\frac{d}{L}\right)^2} = \sqrt{1 - \frac{1}{R^2}} \quad (2.49)$$

with  $R = L/d$  the aspect ratio. Link *et al.* [53,54] calculated the absorption spectra of gold nanorods using Equation 2.46 for various aspect ratios and with the measured dielectric functions of gold [55]. This can be seen in Figure 2.19a where the medium dielectric constant was chosen to be 4. The maximum of the longitudinal plasmon band red-shifts 150 nm when the aspect ratio increases from 2.6 to 3.6. Moreover, Figure 2.19b shows that the increase in the peak position of the longitudinal plasmon band with increasing nanorod aspect ratio follows a linear trend. The data points shown correspond to the absorption maxima of the longitudinal plasmon band as calculated in Figure 2.19a. The dotted line represents a plot of an equation derived by Link *et al.* in order to predict the maximum of the longitudinal plasmon band  $\lambda_{\text{max}}$  [53]

$$\lambda_{\text{max}} = (33.34R - 46.31) \epsilon_m + 472.31 \quad (2.50)$$

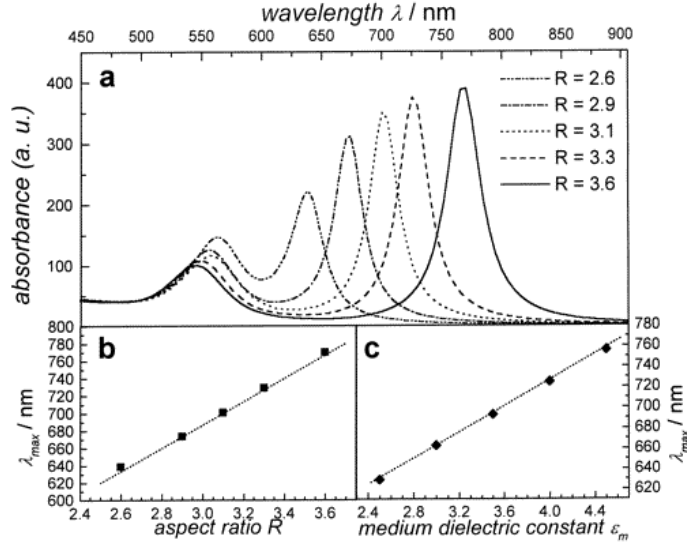


**Fig. 2.19:** Simulation of the surface plasmon absorption for gold nanorods of different aspect ratio by Link *et al.* [53].

It follows from Equation 2.50 that the maximum of the longitudinal plasmon resonance also linearly depends on the medium dielectric constant  $\epsilon_m$ . Hence, Figure 2.19c shows that with increasing medium dielectric constant, there is also a red-shift of  $\lambda_{\max}$  for a fixed aspect ratio  $R = 3.3$ .

### 2.5.6 Light Absorption by Metal Core-Shell particles

Another extension of the Mie theory is its application to Core-Shell nanoparticles. Gold coated silica nanoparticles for example received much interest because of their possible applications in cancer treatments [56, 57]. The solution for scattering from a sphere with a concentric spherical shell was first given by Aden and Kerker [58]. The derived extinction cross section for a small core-shell particle

is [58, 59]

$$\sigma_{\text{ext}} = 4\pi r^2 k \times \text{Im} \left[ \frac{(\epsilon_{\text{shell}} - \epsilon_m)(\epsilon_{\text{core}} - 2\epsilon_{\text{shell}}) + (1 - g)(\epsilon_{\text{core}} - \epsilon_{\text{shell}})(\epsilon_m + 2\epsilon_{\text{shell}})}{(\epsilon_{\text{shell}} + 2\epsilon_m)(\epsilon_{\text{core}} + \epsilon_{\text{shell}}) + (1 - g)(\epsilon_{\text{shell}} - 2\epsilon_m)(\epsilon_{\text{core}} - \epsilon_{\text{shell}})} \right] \quad (2.51)$$

where  $\epsilon_{\text{core}}$  is the complex dielectric function of the core material,  $\epsilon_{\text{shell}}$  is that of the shell,  $g$  is the volume fraction of the shell layer and  $r$  is the radius of the coated particle. Figure 2.20 shows calculations from Halas *et al.* [60] using the

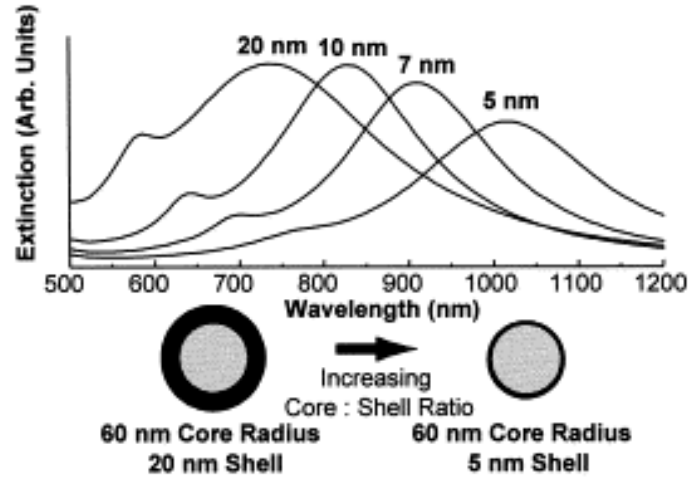


**Fig. 2.20:** Theoretical calculated optical resonances of silica core/ gold shells over a range of core radius/shell thickness ratios [60].

dielectric function of gold [55]. As the shell thickness is varied on a dielectric core of constant size, the optical absorption shifts sensitively as a function of shell thickness and when the shell thickness decreases, the optical absorption is shifted to longer wavelengths. A computer program to calculate coated spheres can be found in Ref [43].



## **Part II**

### **RESULTS & DISCUSSIONS**



## **3. WET CHEMICAL SYNTHESIS TECHNIQUES FOR SMALL SPHERICAL PARTICLES**

### **3.1 Introduction**

The wet chemical synthesis of nanometer-scale coinage metal particles is a major subject in the field of chemistry and physics because of their unusual optical properties [11, 49] and their applications in catalysis [61]. Furthermore, gold and other coinage metal nanoparticles have been proposed as future building blocks in nanotechnological applications [23, 53, 62–64]. Wet chemical methods to prepare such colloids are usually based on the reduction of a suitable metal salt, in the presence of stabilizers. The size and shape of nanoparticles greatly influences their properties [23]. For example, spherical gold nanoparticles exhibit a single plasmon resonance in the visible region of the spectrum, while rodlike particles exhibit a longitudinal and transversal plasmon resonance [65]. The goal of this chapter is to study elementary wet chemical synthesis techniques with a focus on introducing chiral stabilizers to fabricate chiral gold colloids which are interesting materials in fundamental research.

### **3.2 The citrate reduction method**

The citrate reduction method was proposed by Turkevich and this is probably the most well-known method for synthesizing gold colloids [15, 17, 53, 66]. In short,

### 56 Chapter 3. Wet chemical synthesis techniques for small spherical particles

the synthesis procedure to fabricate gold nanoparticles with an average diameter of 20 nm is as follows. Firstly, a solution of 100 mL 1mM hydrogentetrachloroaurate ( $\text{HAuCl}_4$ ) in water is boiled in reflux conditions under vigorous stirring and secondly 10 mL of 38.8 mM aqueous sodiumcitrate is added all at once to the  $\text{HAuCl}_4$  solution. The yellow color in the aqueous solution due to the presence of  $\text{AuCl}_4^-$ , turns clear over dark blue leaving a deep reddish color within a few minutes indicating the formation of gold nanoparticles. This mixture is further stirred and boiled for fifteen minutes, and is then removed from the heat while stirring is continued till room temperature is reached. In this reaction, the citrate ions reduce the gold salt  $\text{HAuCl}_4$  according to

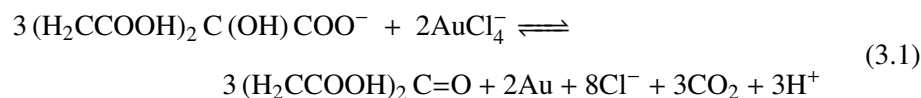
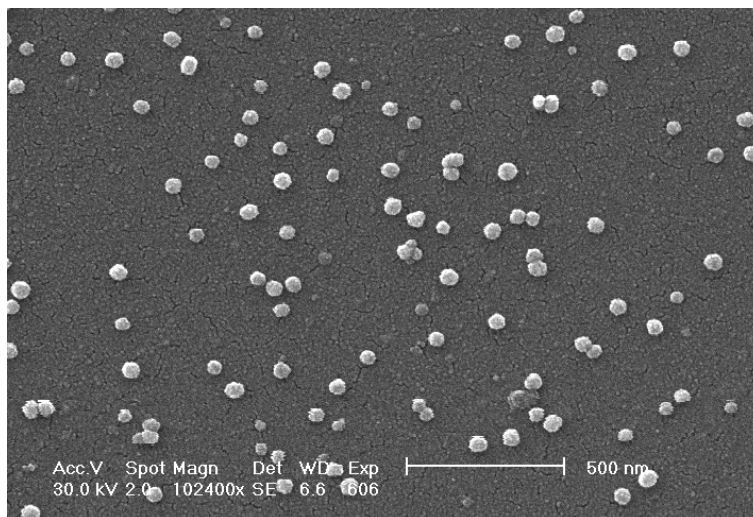


Figure 3.1 shows a characteristic scanning electron microscope picture<sup>1</sup>. It can be seen that the particles are nearly spherical and quasi-monodisperse. The gold col-



**Fig. 3.1:** ESEM picture taken from gold colloids fabricated according to the citrate reduction method.

<sup>1</sup> ESEM pictures were taken with an XL30 ESEM-FEG Scanning Electron Microscope by Ing. Rudy De Vos from the Department of Metallurgy and Materials Engineering (MTM).

loids are stabilized by negatively charged citrate ions and chloride ions that are still present in the solution. Irreversible aggregation or coagulation is easily induced by addition of electrolytes (e.g. KI, NaCl, KNO<sub>3</sub>) to the solution. The coagulation of colloidal gold was studied extensively by Turkevich *et al.* [35]. It is important to note that the citrate is as well a reductant as a kinetic stabilizer. Hence, chirality

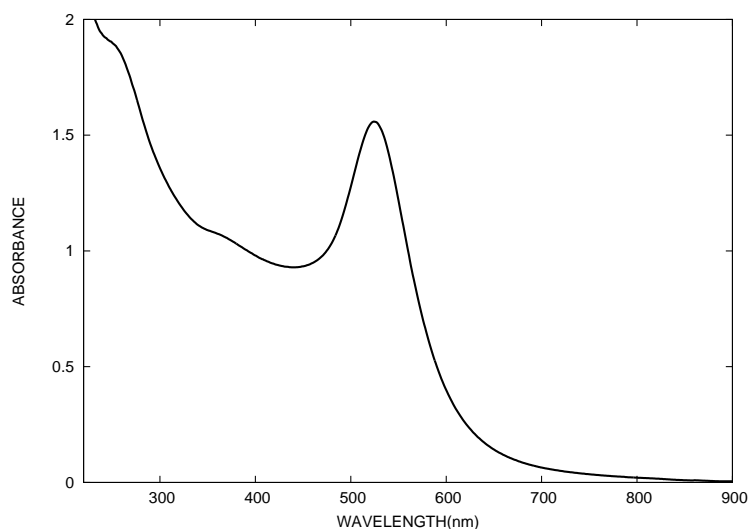


**Fig. 3.2:** UV-VIS spectrum taken from a solution of gold colloids according to the citrate reduction method.

on the surface of the nanoparticles is difficult to introduce. Frens succeeded in fabricating gold sols with average sizes differing from 16 nm to 147 nm by changing the concentration of the added sodium citrate [17]. Adding less sodium citrate, leads to bigger particles, but these results are less reproducible, indicating the importance of the citrate ions stabilizing the gold colloids. The larger particles are less monodisperse and the color of the solution is violet. A typical UV-Vis spectrum<sup>2</sup> from a dispersion of gold colloids according to the citrate reduction method described above is shown in Figure 3.2. The absorption band around 520 nm is the plasmon resonance band which is responsible for the remarkable colors in colloidal gold sols and in other dispersions of silver or copper. The properties of colloids de-

<sup>2</sup> UV-Vis spectra were taken with a Perkin Elmer Lambda 900 spectrophotometer available in the laboratory.

pend on the particle size and the plasmon band shifts to longer wavelengths when larger (less monodisperse) gold nanoparticles are prepared.

### 3.3 The Brust method

This method was described by Brust *et al.* in 1994 [18]. In contrast to the citrate reduction method, where the gold colloids are kinetically stabilized in aqueous solutions by an electrical double layer, the gold colloids in the Brust method are sterically stabilized by organic molecules having thiol, amide or acid groups. The stabilization with organic molecules having thiols is due to the fact that gold binds specifically to the sulfur atom of the thiol group [67] while the organic molecules forms the actual stabilization preventing the particles to coagulate. The main advantage of the Brust method is that the gold particles behave, in a way, as chemical compounds [68]. The particles can be precipitated, filtered off and redispersed in organic solutions. Furthermore, several stabilization agents with thiol, amide or acid groups can be used to sterically stabilize the gold colloids. Therefore, interesting hybrid materials can be formed using this method. In this section we discuss the work done in the laboratory by stabilizing the gold colloids with a chiral stabilizer which is thiocholesterol and we use this Brust method to stabilize gold colloids by using polythiophenes to form an interesting hybrid material. The structural formulas of these two molecules, used in the laboratory is shown

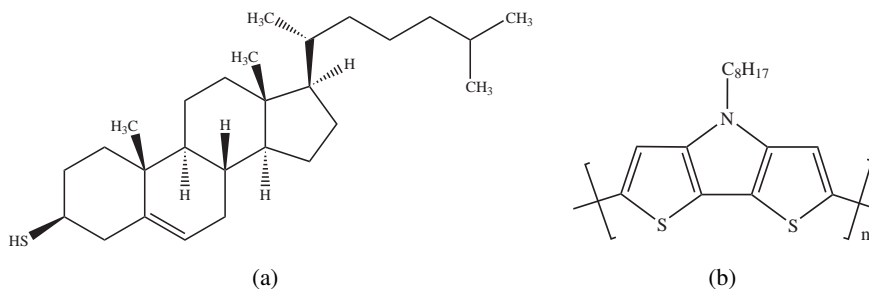
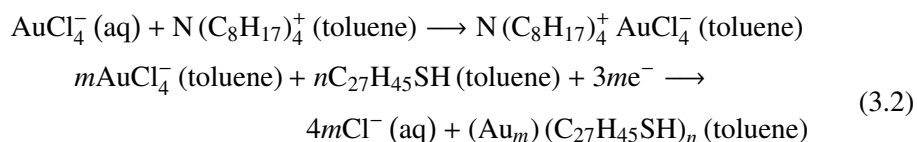


**Fig. 3.3:** Structural formulas of thiocholesterol (a) and a derivative of polythiophene (b) used in the laboratory to stabilize gold colloids by the Brust method.

in Figure 3.3. Thiocholesterol is commercially available (Sigma Aldrich), but the derivatives of fused polythiophenes were synthesized by Koeckelberghs *et al.* [69]. Both approaches to stabilize gold colloids with these two different stabilizers are discussed separately.

### 3.3.1 Stabilization of gold colloids with thiocholesterol

With the Brust method it is possible to use many organic molecules to stabilize gold nanoparticles as long as the molecules have the appropriate functional groups to bind on the gold surfaces. Here, we describe the stabilization of gold colloids with thiocholesterol. The strategy to do this consists in letting the metallic clusters grow with the simultaneous attachment of self-assembled thiocholesterol monolayers on the growing nuclei [18]. To allow this strategy, the particles are grown in a two-phase system by transferring a gold salt  $\text{HAuCl}_4$ , from an aqueous solution to an organic solvent (e.g. toluene) using a phase-transfer catalyst (e.g. tetraoctylammonium bromide). Subsequently, an appropriate amount of thiocholesterol ( $\text{C}_{27}\text{H}_{45}\text{SH}$ ) is added, needed for stabilizing the formed nanoparticles. On addition of the reducing agent ( $\text{NaBH}_4$  in water), the organic phase changes color from orange to deep brown within seconds. The formed colloids are stabilized immediately by the presence of the thiols. These colloids have diameters around 5 nm. The overall reaction can be summarized as follows



After the synthesis, the organic layer must be separated and evaporated to 10 mL in a rotary evaporator. To remove the excess of thiocholesterol, the organic phase is mixed with 400 mL ethanol. The mixture is then kept at  $-10^\circ\text{C}$  for several hours. The brown precipitate can be filtered off and washed with ethanol. These gold colloids, stabilized with thiocholesterol, are then redissolved in an organic solvent (e.g. toluene) and the procedure from the mixing is repeated twice. These colloids can be made quasi-monodisperse by dissolving the gold colloids in 100 mL toluene

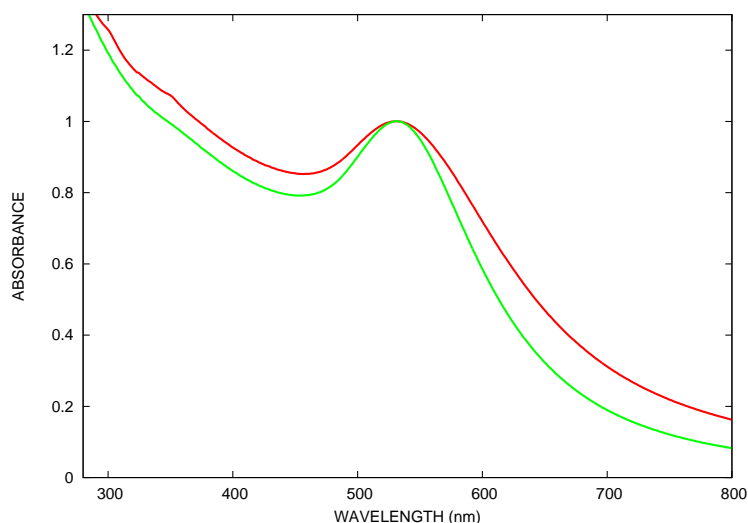


**Fig. 3.4:** The Brust method: before *digestive ripening* (red line); after *digestive ripening* (green line).

and refluxing this mixture for half an hour. In literature this process is described as *Digestive Ripening* [70]. Figure 3.4 shows the influence of refluxing on the plasmon band whereas the nanoparticles become nearly monodisperse. The plasmon band is sharper and less broad after refluxing than before. In Figure 3.5 a circular dichroism (CD) spectrum<sup>3</sup> from gold colloids stabilized by the chiral thiocholesterol and dissolved in toluene can be seen. Although there is no circular dichroism in the region of the plasmon band, there is a CD band present in the 210-260 nm region, attributed to the presence of thiocholesterol bound to the gold colloids (Figure 3.6). Important to notice is that the CD band is not due to excess thiocholesterol still present in the solution, because the solution has been washed and filtered several times with ethanol. Together with the fact that gold colloids are dissolved in toluene, we can conclude that chiral colloids were formed. However, the chirality was not transferred to the spherical particle which would lead to circular dichroism near the plasmon absorption.

<sup>3</sup> Circular dichroism (CD) spectra were taken with a Jasco J-810 Spectropolarimeter available in the laboratory.



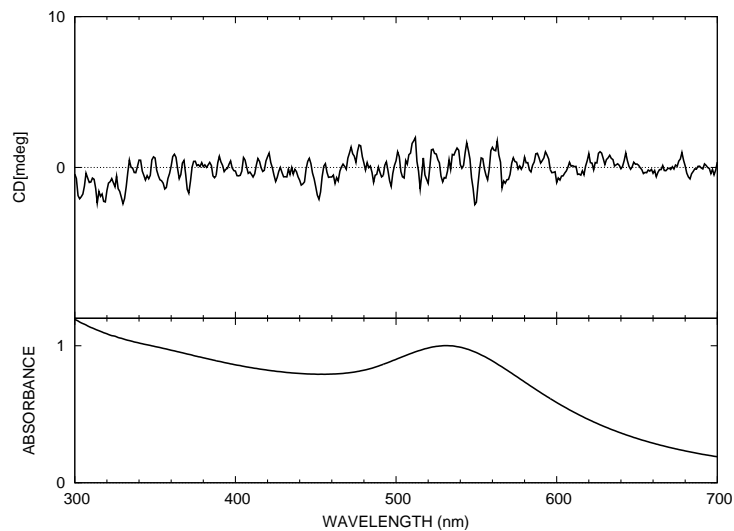


**Fig. 3.5:** CD spectrum from gold colloids prepared following the Brust method (above) and the corresponding UV-Vis spectrum showing the plasmon resonance (down).

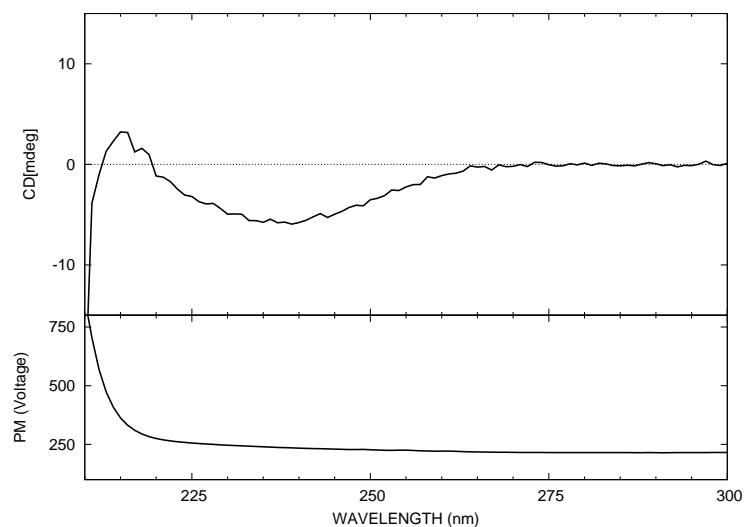


**Fig. 3.6:** Circular dichroism from thiocholesterol in the region between 210-260 nm. Note that the ordinate in the lower curve is labeled by the High Tension voltage (HT) of the photomultiplier (PM). This can be converted to an absorption spectrum showing an identical spectrum.

### 3.3.2 Stabilization of gold colloids by polythiophenes

The stabilization of gold colloids by regioregular polythiophenes is described by McCullough *et al.* which is an interesting application of the Brust method because now special gold nanoparticle hybrid materials are formed [71]. This work has been repeated in the laboratory using poly(N-substituted dithieno[3,2-*b*:2',3'-*d*]pyrrole)s (PDTPs) synthesized by Koeckelberghs *et al.* [69], with the structure given in Figure 3.3(b). To prevent the oxidation of the PDTPs, a large amount of the phase-transfer catalyst tetraoctylammonium bromide is used. The strategy to let the metallic clusters grow, however is the same as described above. The particles are grown in a two-phase system by transferring the gold salt  $\text{AuCl}_4^-$  from the aqueous solution to the toluene solution using by the phase-transfer catalyst. The gold salt is then reduced by  $\text{NaBH}_4$  in water. The gold particles are first stabilized by the phase-transfer catalyst and subsequently, an amount of PDTPs are added which stabilizes the formed nanoparticles. Furthermore, the gold nanoparticles are

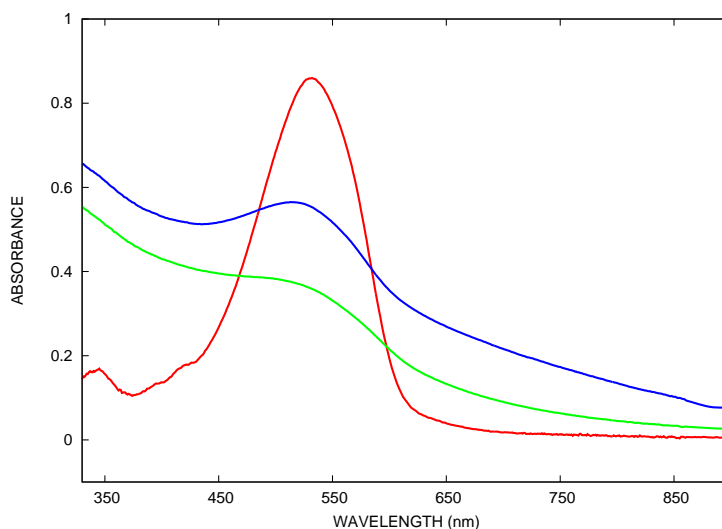


**Fig. 3.7:** UV-Vis absorption spectra taken from a solution of the pure derivatives of fused polythiophenes (PDTPs) in toluene (red), tetraoctylammonium bromide-stabilized gold nanoparticles in toluene (green) and the PDTPs stabilized gold nanoparticles in toluene (blue).

stabilized by the interaction of the sulfur atoms of the PDTPs with the surfaces of the gold nanoparticles. UV-Vis spectra taken from the derivatives of the PDTPs in toluene, gold nanoparticles stabilized with the phase-transfer catalyst and gold nanoparticles stabilized with PDTPs are shown in Figure 3.7. The pure PDTPs show a strong absorbance around 530 nm. The plasmon band coming from the gold nanoparticles stabilized with the phase transfer catalyst is around 520 nm. The polythiophene stabilized nanoparticles show a more characteristic plasmon

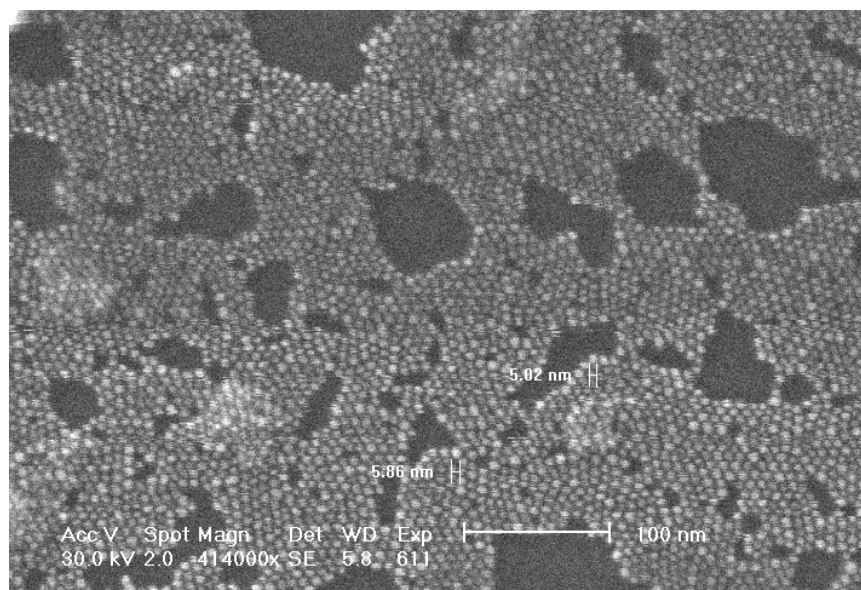


**Fig. 3.8:** ESEM image of regioregular polythiophene stabilized gold nanoparticles.

resonance that is more pronounced being typical for particles around 5 nm. This is confirmed by ESEM and a figure of the stabilized gold nanoparticles with PDTPs is shown in Figure 3.8. The particles are all spherical and nearly monodisperse. It is interesting to notice from this ESEM figure that the nanoparticles are arranged in a structured lattice pattern. Furthermore, it is confirmed that they have diameters around 5 nm.

### 3.4 Optical activity coming from gold clusters and gold complexes

#### 3.4.1 Gold-Glutathione cluster compounds

T. Gregory Schaaff and Robert L. Whetten wrote a study in 2000 about metal clusters being optical active [72]. The metal clusters were composed of a gold core stabilized by the tripeptide glutathione ( $\gamma$ -*glu*-*cys*-*gly*, GSH, Figure 3.9(a)). The gold clusters were less than 1 nm ( $\sim 20 - 40$  Au atoms). They were prepared by reducing a mixture of  $\text{HAuCl}_4$  and glutathione in water with  $\text{NaBH}_4$  to fabricate gold:glutathione (Au:SG) cluster compounds. The synthesis procedure to prepare

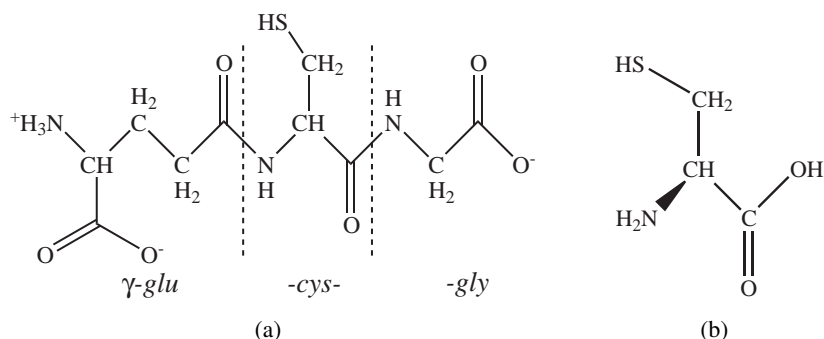


**Fig. 3.9:** Structural formulas of glutathione (a) and L-cysteine (b) used in the laboratory to stabilize gold clusters with the method described by Schaaff and Whetten [72].

Au:SG cluster compounds, described by Schaaff and Whetten, is repeated in the laboratory. In general, 3.0 mmol of glutathione is dissolved in 40 mL distilled water, and 1.0 mmol of  $\text{HAuCl}_4$  is dissolved in 80 mL of methanol. By mixing these two solutions, a white suspension is obtained known as a Au(I)SG polymer [73]. While stirring this solution, 10 mmol  $\text{NaBH}_4$  in 10 mL of water is added all at once. Immediately, the color changes to dark brown, indicating the formation of Au:SG cluster compounds. The precipitate is filtered off and redissolved in 10 mL of distilled water. It is precipitated again with methanol and then filtered off. These steps can be repeated to remove all starting material and byproducts. The mixture is highly soluble in water and insoluble in methanol. The corresponding CD spec-

trum of the Au:SG cluster compounds in water is shown in Figure 3.10. The CD spectrum clearly shows circular dichroism while the specific plasmon band in the

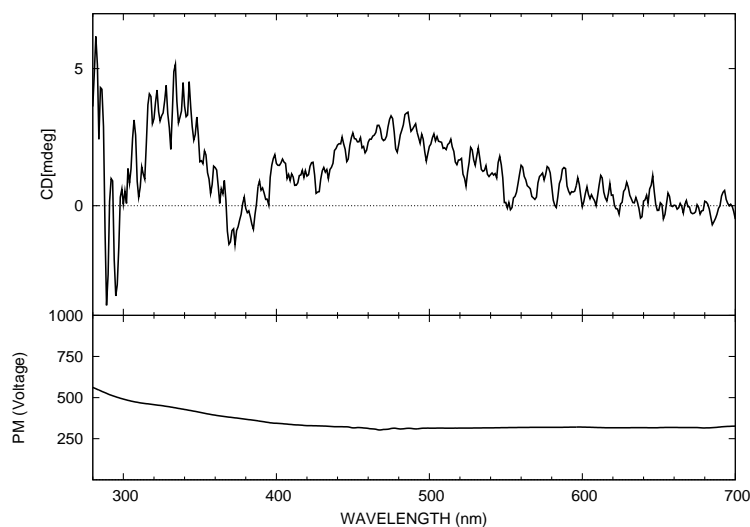


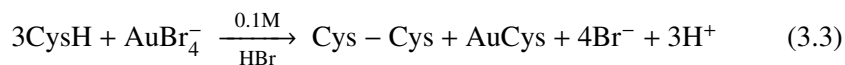
**Fig. 3.10:** CD spectrum from gold colloids according to the Schaaff-Whetten method.

absorption spectrum is almost absent which is in agreement with the Mie theory. Small gold clusters ( $< 1$  nm) do not show a specific plasmon band. The Mie theory predicts that specific plasmon bands are appearing from 1 nm [13,48]. Schaaff *et al.* gave three possible reasons to explain the CD effect whereby they believe that the first reason is the most likely:

- (a) Gold clusters are having a chiral crystal structure.
- (b) The gold clusters are achiral, but the bound thiols are adsorbing in a spacelike pattern that is chiral. Although the metal-thiol bond is still a scientifically unresolved problem, it is plausible that the bond has a strong effect on the electronic structure of the gold.
- (c) Chirality is only coming from chiral centers, present in the molecules.

### 3.4.2 L-Cysteinato-gold(I) complexes

The bonding of the tripeptide glutathione to gold is dependent on the amino acid L-cysteine (Figure 3.9(b)) having the necessary thiol group to bind specifically to the gold surface. Hence, a study was done in the laboratory whereby the same experiments described to fabricate Au:SG compounds were repeated with L-cysteine (Cys) to form Gold:Cysteine (Au:SCys) cluster compounds. Many research was done by Shaw *et al.* to investigate the interaction between gold salts and L-cysteine [73, 74] because cysteinato-gold(I) complexes were used in the eighties in medical applications like the treatment of rheumatic arthritis [75]. Two different complexes between gold and L-cysteine can be formed and it was interesting to investigate these two L-Cysteinato-gold(I) complexes with CD spectroscopy. L-Cysteinato-gold(I) can be easily prepared by the reaction of three moles cysteine with  $\text{AuBr}_4^-$  at low pH:



In this reaction the cysteine is a reducing agent for Au(III) and HBr avoids the oxidation product cystine. The formed L-Cysteinato-gold(I) can then be washed with pure ethanol and ether. The solubility of L-Cysteinato-gold(I) is around  $1.1 \mu\text{M}$ . Because this solubility is very low, the experiments were done with better soluble complexes being formed between cysteine esters and gold salts. The commercial available L-cysteine-ethyl ester was used whereby reaction 3.3 is still correct. After the addition of three moles cysteine-ethyl ester to one mole  $\text{AuBr}_4^-$  at low pH, CD and UV-Vis spectra were recorded. In more detail, to a solution of 10 mL  $1.8 \times 10^{-3}$  M  $\text{HAuBr}_4$  different amounts of a 0.1 M cysteine-ethyl ester solution have been added. After the addition of 0.6 mL from the 0.1 M cysteine solution to the  $\text{HAuBr}_4$  solution (ratio 3/1), there is a remarkable CD band as shown in Figure 3.11. Furthermore, Figure 3.11 shows also a spectrum from a concentrated cysteine-ethyl ester solution (0.1 M). Hence, it is clear from the figure that the complex formed with gold leads to an increased circular dichroism where the concentration of the added cysteine-ethyl ester was  $6 \times 10^{-3}$  M. After the addition of an excess cysteine-ethyl ester to this solution an equilibrium between a second gold(I)

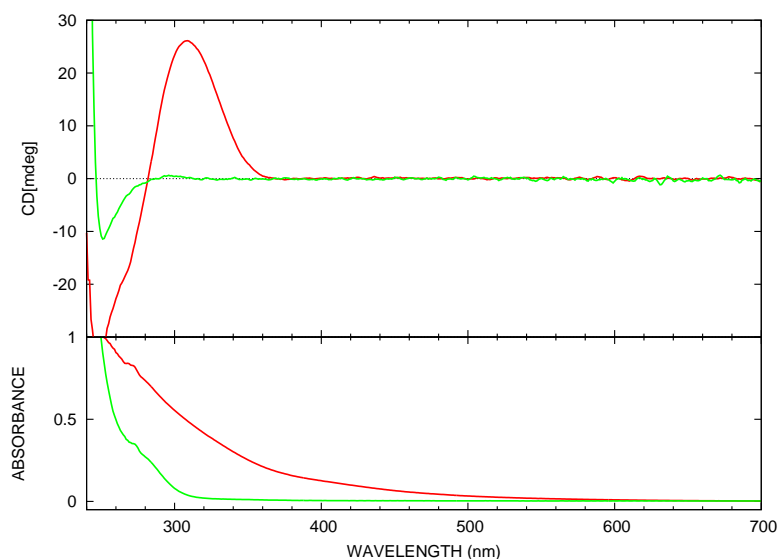
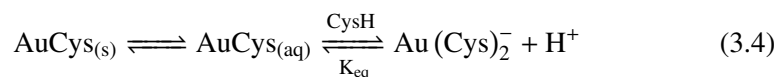


**Fig. 3.11:** Comparison of the CD and UV-Vis spectra between the L-cysteinato-ethyl ester gold(I) complex (red line) whereby the concentration of the added cysteine-ethyl ester is  $6 \times 10^{-3}$  M and a solution of 0.1 M L-cysteine-ethyl ester in water (green line).

complex can be obtained according to the reaction [74]



where  $\text{Au}(\text{Cys})_2^-$  is the bis(cysteinato-ethyl ester)-gold(I) complex. Figure 3.12 shows CD and UV-Vis spectra from these two different gold(I) complexes with L-cysteine-ethyl ester. These gold(I) complexes are stable and therefore it is easy to study their electronic and CD spectra. Since Au(I) is oxidizing as well as reducing, ligand-to-metal charge transfers (LMCT) and metal-to-ligand charge transfers (MLCT) transitions in gold(I) complexes can occur. However, gold(I) complexes with more reducing agents display LMCT absorptions at longer wavelengths [30]. Therefore, the absorption bands in Figure 3.12 around 305 nm and 370 nm coming from the complex  $\text{AuCys}_2^-$ , with L-cysteine-ethyl ester being a more reducing ligand, are probably LMCT transitions.

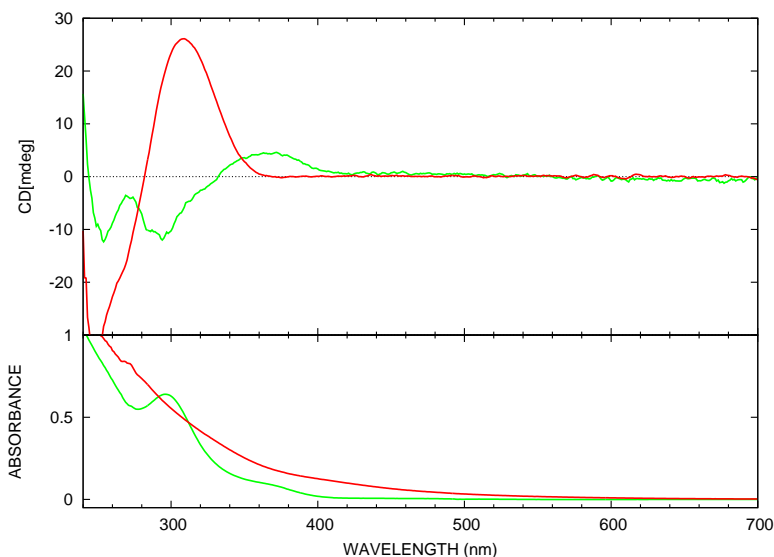


**Fig. 3.12:** Comparing the CD and UV-VIS spectra between  $\text{AuCys}_{(\text{aq})}$  (red line) and  $\text{AuCys}_2^-$  (green line).

### 3.4.3 Gold-L-cysteine-ethyl ester cluster compounds

If the first complex  $\text{AuCys}_{(\text{aq})}$  is reduced with  $\text{NaBH}_4$ , gold clusters can be formed where the thiol group of L-cysteine-ethyl ester binds with the surface of the gold particles. Again it is interesting to take CD spectra and to compare this with the spectrum from the Au:SG clusters. The comparison is shown in Figure 3.13. Some remarkable CD bands are appearing around 270, 375 and 460 nm. Furthermore, the CD spectra are completely different from the CD spectra taken from the two L-cysteinato-ethyl ester gold(I) complexes (Figure 3.12). The plasmon band from the gold clusters with L-cysteine-ethyl ester in the Figure below is remarkable, because now bigger particles are formed. In contrast to the Brust method, circular dichroism can be seen near the plasmon band. From the three reasons mentioned by Schaaff *et al.*, we can delete the third one because here gold colloids were formed with CD bands lying in a broad eV region whereas in the Brust method only circular dichroism was seen in the region between 210 and 260 nm where it was coming from thiocholesterol bound to the gold colloids. Only the first two reasons can be



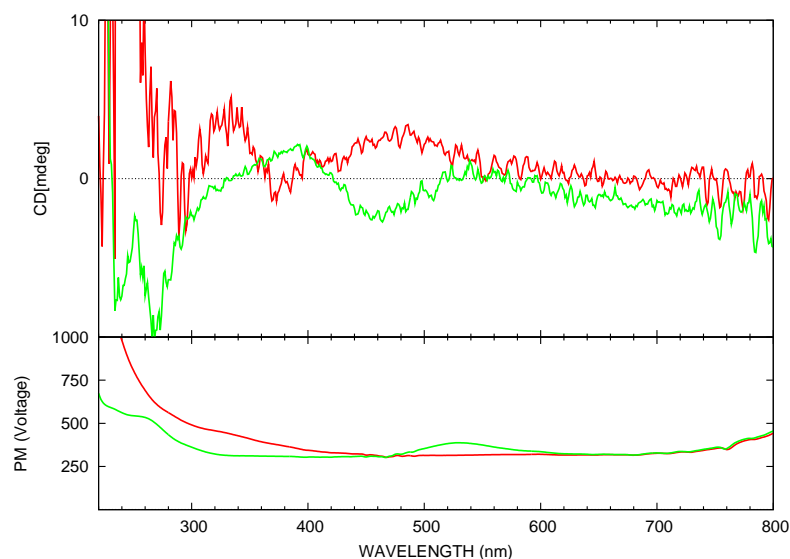


**Fig. 3.13:** Comparison between the CD spectra from Au:SG (red line) and Au:SCys (green line).

considered as the explanation of the CD bands. On one hand the gold colloids can configure in a chiral crystal structure, but on the other hand the biomolecules can conform in a chiral pattern and it is most likely that the adsorption between the specific thiol group from the cysteine and the gold surface raises local effects on the electrons.

### 3.5 Conclusions

In this chapter wet chemical synthesis procedures were discussed to synthesize small spherical gold particles and gold clusters. The particles were characterized by scanning electron microscopy (SEM), UV-Vis spectroscopy and CD spectroscopy. The citrate reduction method has been discussed, being the standard procedure to fabricate gold colloids. The citrate reduction method is useful in understanding the theoretical background of colloidal solutions where the particles are stabilized kinetically by an electrical double layer and therefore chirality is difficult to in-

### **70 Chapter 3. Wet chemical synthesis techniques for small spherical particles**

---

troduce. However, with the Brust method, stabilizing agents with thiol groups can be introduced where the thiol group can bind specifically to the surface of the gold particles. The dispersions of gold particles in organic solvents, prepared by the Brust method, are typical examples of sterically stabilized colloidal solutions. Here, thiocholesterol and derivatives of fused polythiophenes were used to stabilize gold nanoparticles fabricated according to the Brust method. Furthermore, the preparation of small gold clusters was discussed where the particles were stabilized by the biomolecules glutathione and L-cysteine-ethyl ester. Here, we were able to study the stable gold(I) complexes with ligands L-cysteine ethyl ester by taking CD and UV-Vis spectra. After reducing these gold(I) complexes, gold clusters stabilized with L-cysteine-ethyl ester were formed and characterized with CD and UV-Vis spectroscopy.

## **4. PREPARATION OF SMALL METAL PARTICLES BY LASER ABLATION**

### **4.1 Introduction**

In Chapter 3 wet chemical methods to synthesize small metal particles in solution were discussed. Wet chemical methods to prepare metal nanoparticles are based on the reduction of a suitable metal salt, in the presence of stabilizers. Laser ablation, on the other hand, is an alternative route to the chemical synthesis for the preparation of small metal particles [76]. The main advantage of laser ablation is the high purity of the nanoparticles whereas pure bulk materials and solvents can be used in the preparation. Another advantage of this method, includes its simplicity and its versatility with respect to metals or solvents in the absence of chemical reagents or ions in the final solution. Furthermore, it is shown that laser ablation of gold and silver produces stable colloids [77]. This chapter begins with the experimental set-up for a laser ablation experiment and then the preparation of gold, silver or copper colloids in pure Milli-Q water is discussed. In a short literature overview, the dynamic formation mechanism of nanoparticles stabilized by a surfactant in aqueous solutions and the size reduction process shall be explained [78]. In organic solutions however, the laser ablation experiments have been less reported. Therefore, we performed a study of gold ablated in chloroform solutions of the cationic surfactant cetyltrimethylammonium bromide. Chloroform was chosen because it dissolves many organic compounds. It is shown that when gold is ablated under the right circumstances gold complexes are formed instead of gold nanoparticles. On the basis of these observations we propose in this chapter an alternative mechanism for a laser ablation experiment of solid gold.

## 4.2 Experimental set-up

The experimental set-up for a laser ablation experiment is shown schematically in Figure 4.1. Metal nanoparticles are produced by focussing a Q-switched Nd:YAG laser (1064 nm, 8nsec pulses) as the irradiation source on a metal wire. The laser

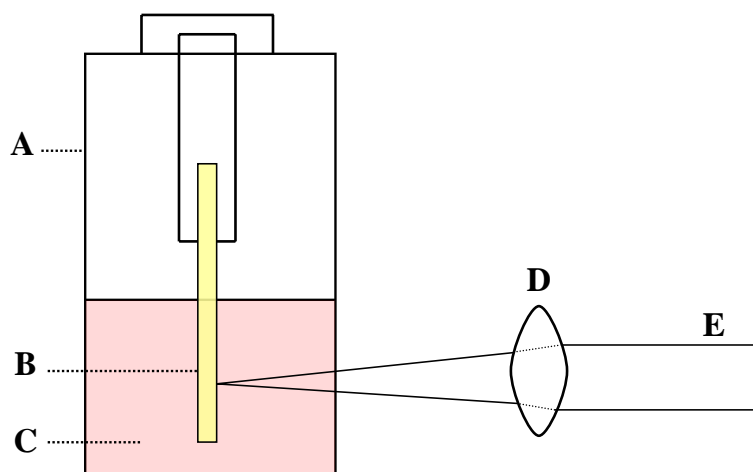


**Fig. 4.1:** Schematic representation for a laser ablation experiment. **A**, Sample holder; **B**, metal; **C**, solvent; **D**, focal lens; **E**, 1064 nm laserbeam.

used in our experiments has an energy output of 5-15 mJ operated at 50 Hz. The 1064 nm laser beam is focused by a lens with 50 cm focal length on the metal wire, suspended in ~ 25 mL of solvent. Typical ablation times were 10 minutes.

## 4.3 Laser ablation of the coinage metals

Laser ablation of gold, silver and copper provides a rapid and simple method for the fabrication of colloidal solutions of the coinage metals. These colloids can be prepared in any solvent, but sometimes solvent decomposition (e.g. in hexane or cyclohexane) can occur due to 1064 nm pulsed laser irradiation [77]. Typical

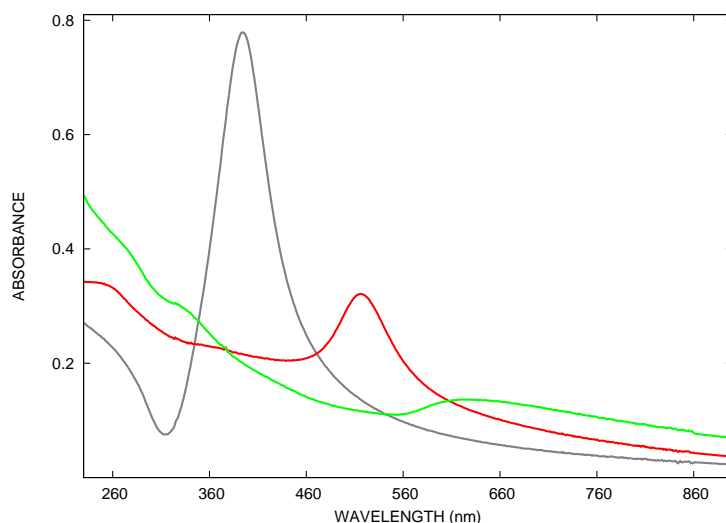


**Fig. 4.2:** UV-Vis absorption spectra of silver (gray line), gold (red line) and copper (green line) ablated with a 1064 nm Nd:YAG laser in Milli-Q water.

UV-Vis absorption spectra of colloidal dispersions in Milli-Q water prepared by laser ablation with a 1064 nm beam focused on the metal wires, are shown in Figure 4.2. The absorbance can be varied by changing the irradiation time or the pulse energy. The characteristic spectral features for the silver and gold colloids around 400 and 520 nm respectively are the surface plasmon excitations which causes the colloidal silver solution to appear yellowish-gray whereas the colloidal gold solution is red [49, 79]. Note that the colloids with their absorption spectra shown in Figure 4.2 were prepared in pure Milli-Q water and that no other chemical compounds were used during the ablation process, but the metal itself. Hence, the other spectral features in the UV region can be assigned to the metal interband transitions [43, 44, 77, 79]. The metal copper, on the other hand, is highly reactive and therefore it is difficult to prepare stable copper colloids in water with laser ablation. Furthermore, laser pulses create reactive species which rapidly react with copper to form byproducts like copper oxide and copper hydroxide [77]. However, it is still possible to observe the copper plasmon band appearing around 625 nm (Figure 4.2) where the color of the colloidal solution is olive green. The broadening of the plasmon band in the copper solutions is most likely due to the fact that

colloidal copper aggregates were formed as a result of the oxidation [80]. The spectral features below 450 nm in the UV-Vis absorption spectrum of the copper colloids can be assigned to metal interband transitions and also to absorptions of the byproducts formed during the ablation process. Hence, it is obvious that stable colloidal copper solutions can only be formed by laser ablation in an oxygen-free environment using stabilizing agents and other solvents than water.

## 4.4 Theoretical Discussion

An overview of the mechanisms proposed in literature shall now be given. The formation of metal nanoparticles fabricated with laser ablation in aqueous solutions of a surfactant is explained by the Dynamic Formation Mechanism [79]. The sizes of the metal nanoparticles can be controlled by the Laser-induced Size Reduction Process [81].

### 4.4.1 The Dynamic Formation Mechanism

Laser ablated silver and gold nanoparticles with diameters less than 10 nm were developed by Mafuné *et al.* and involved irradiation of a silver or gold plate in aqueous solutions of the surfactant sodium dodecyl sulfate (SDS) with the output of the fundamental (1064 nm) or the second harmonic (532 nm) of a pulsed Quanta-ray Nd:YAG laser operating at 10 Hz [79, 82]. Mafuné *et al.* proposed a mechanism for the ablation process, the so called *dynamic formation mechanism*, which is dependent on the concentration of SDS [82]. After laser ablation, a dense cloud of metal atoms (a metal plume) is produced over the laser spot of the metal plate where the atoms aggregate as fast as they are supplied. This initial aggregation continues until the metal atoms in the close vicinity are almost completely consumed resulting in the growth of embryonic metal particles in a region void of atoms. Outside this region however, the supply of atoms by diffusion causes the particles to grow slowly even after rapid growth is stopped. The surfactant SDS now plays an important role in determining the stability and size of the nanoparticles whereas the slow growth of the particles tends to stop when their surfaces

are coated with SDS, which diffuses through the solution toward the particles. The nanoparticles end up coated with a double layer of SDS, ensuring the stability of the particles in solution. In the first layer the SDS molecules orient with the hydrophilic  $-\text{OSO}_3^-$  end inward and with the hydrophobic  $-\text{C}_{12}\text{H}_{25}$  end outward, while in the second layer they do the opposite [79]. Therefore, it can be concluded that the stability of the nanoparticles is dependent on the surfactant concentration, characterized by the coverage of their surfaces with SDS.

#### 4.4.2 The Laser-induced Size Reduction Process

A disadvantage of laser ablation is that when nanoparticles are formed, it is difficult to change their size and to control the aggregation of the ablated atoms. However, size reduction of gold nanoparticles can be induced by laser irradiation (532 nm) in the vicinity of the wavelength of the surface plasmon resonance (520 nm) [81–84]. Gold nanoparticles in solution do not absorb photons at 1064 nm, but absorb photons at 532 nm whereby they fragment into smaller particles. Furthermore, gold nanoparticles can be prepared with laser ablation of the metal at 1064 nm and dissociation can then be achieved by irradiation at 532 nm. When the gold nanoparticles are irradiated with a 532 nm laser, the plasmons in the gold nanoparticles absorb photons and the electrons are excited. During a single laser pulse, one gold nanoparticle is considered to absorb more than one thousand photons and its temperature rises significantly so that fragmentation starts [85]. The mechanism of laser-induced size reduction was proposed by Takami *et al.* [76, 81]. When the electrons in the gold nanoparticles are excited, the temperature of the nanoparticles can rise above the melting point and become liquid. A size reduction takes place due to the vaporization of the gold nanoparticles when the temperature rises to the boiling point while atoms or even small particles are ejected via vaporization. The amount of the ejected atoms depends on the absorbed laser energy. The diameter of the nanoparticles is determined by the equilibrium between the ejected atoms, being very unstable in aqueous solutions, and the deposition of the ejected atoms back onto surfaces of the nanoparticles. The ejected atoms can also agglomerate to form gold nanoparticles themselves.

This process is a promising technique for the preparation of size-selected gold

nanoparticles in solution with diameters less than 10 nm [76].

## 4.5 Laser ablation of gold in chloroform

Laser ablation can be performed in any solvent. Laser ablation of solid gold in chloroform solutions had not been reported in literature although chloroform has the advantage that it dissolves many organic compounds easily. Therefore, a detailed discussion of a study of pure bulk gold being ablated in chloroform is given in this section. The stabilizing agent that is introduced during the ablation process is the cationic surfactant cetyltrimethylammonium bromide (CTAB). The struc-

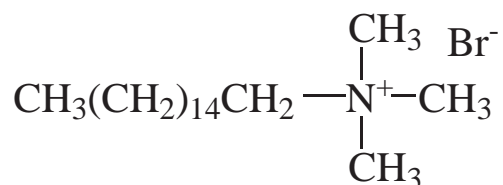


**Fig. 4.3:** Structural formula of the cationic surfactant cetyltrimethylammonium bromide .

tural formula of CTAB is given in Figure 4.3. In the presence of this quaternary ammonium salt gold complexes are formed, instead of gold colloids. At intermediate concentration of CTAB we can observe the formation of cetyltrimethylammonium tetrabromo aurate ( $\text{CTA}^+ \text{AuBr}_4^-$ ) and at higher concentrations of CTAB cetyltrimethylammonium dibromo aurate ( $\text{CTA}^+ \text{AuBr}_2^-$ ) is formed. These observations are consistent with the initial formation of gold ions in the ablation process, followed by complexation with the bromide ions of the quaternary ammonium salt.

### 4.5.1 Experimental Results

In a first experiment the ablation process of a gold wire was performed in pure chloroform without adding any stabilizing surfactants. During the ablation process a red-purple plume of material was emanating from the focus of the laser beam, indicating the formation of gold nanoparticles. After a few minutes the whole



solution became red-purple. The corresponding UV-Vis absorption spectrum is shown in Figure 4.4 where the intense absorption around 565 nm can be attributed to the plasmon resonance of the gold nanoparticles. The plasmon band of the gold

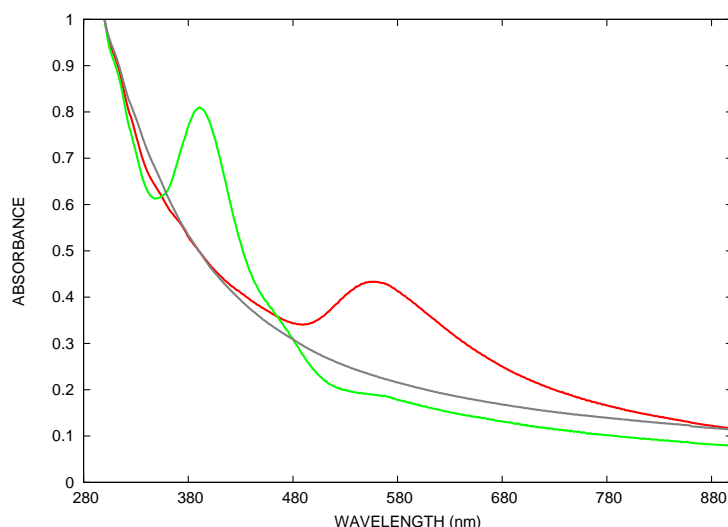


**Fig. 4.4:** UV-Vis absorption spectra of gold ablated in pure chloroform (red line),  $10^{-3}$  M of CTAB in chloroform (green line), and 0.5 M of CTAB in chloroform (gray line).

nanoparticles, shown in Figure 4.4, is relatively broad compared to the plasmon band of gold ablated in pure Milli-Q water (Figure 4.2) which is characteristic for aggregation [66]. Furthermore, after several hours, visible aggregates precipitate in the cell. This precipitation is due to a lack of coulombic stabilization by an electric double layer of the colloidal particles, which leads to their rapid coagulation. When measured directly after the ablation process, dynamic light scattering studies<sup>1</sup> indicate an average size of 30 nm. It is clear though, that the gold nanoparticles formed in chloroform need stabilization. Therefore, the ablation was performed in chloroform solutions of varying concentrations of the quaternary ammonium salt cetyltrimethylammonium bromide (CTAB). This surfactant can be easily dissolved in large amounts of chloroform. At low concentrations of CTAB ( $10^{-4}$  M), the intensity of the plasmon band starts to decrease and a new band at 400 nm appears.

<sup>1</sup> Dynamic light scattering studies were performed with a Malvern Instruments Ltd Zetasizer PCS 5201 available in the laboratory.

At  $10^{-3}$  M the absorption at 400 nm is maximal and the plasmon band is completely absent. These results can be seen in Figure 4.4. The ablated solutions with CTAB were bright yellow and note that the plume of material generated in the laser focus was also bright yellow. Furthermore, dynamic light scattering was never able to detect the presence of the nanoparticles. However, some precipitation in the cell could be visually observed. Since the appearance of the band at 400 nm is correlated with the CTAB concentration (and therefore with the concentration of cetyltrimethylammonium ions and bromide ions), it is plausible that instead of the formation of gold particles, the high CTAB concentration leads to the formation of the tetrabromo aurate ions. To verify this hypothesis the UV-Vis spectra of the “ablated” solution were compared with the spectra of hydrogen tetrabromo aurate solubilized in chloroform by CTAB. These spectra are shown in Figure 4.5. As

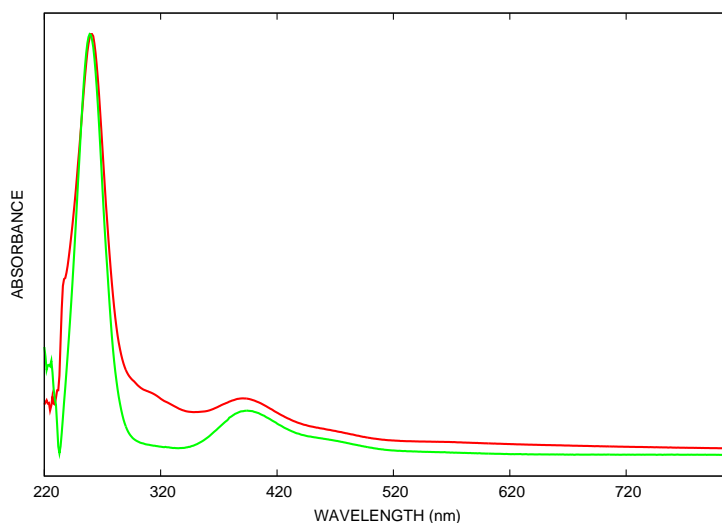


**Fig. 4.5:** UV-Vis absorption spectra of gold ablated in  $10^{-3}$  M of CTAB in chloroform (red line) and cetyltrimethylammonium tetra bromo aurate in chloroform (green line).

can be seen, the position and shape of the absorption band is identical with that observed in the ablation process. Furthermore, addition of a small amount of sodium borohydride ( $\text{NaBH}_4$ ) to the ablated chloroform solution immediately produces a bright red color, indicative of colloid formation.

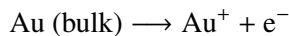
When the concentration of CTAB in the ablation experiment is further increased

the absorption band due to the tetrabromo aurate completely disappears and we obtain a rather featureless spectrum (Figure 4.4). Nevertheless, if a small amount of  $\text{NaBH}_4$  was added to the solution, the solution became bright red again and the spectrum showed a clear plasmon band, indicative of nanoparticle formation. This suggests the presence of another gold ion with an absorption spectrum in the UV part of the spectrum. One possibility is that instead of  $\text{AuBr}_4^-$ ,  $\text{AuBr}_2^-$  is now formed with  $\text{AuBr}_2^-$  being a colorless compound. Unfortunately, it is difficult to verify the presence of  $\text{AuBr}_2^-$  in this experiment because the presence of a large amount of CTAB obscures all spectral features of the  $\text{AuBr}_2^-$  ion, and positive identification is impossible.

#### 4.5.2 A proposal for the Laser Ablation Mechanism

Two possible reasons for the observed behavior can be put forth: either gold is ionized during the ablation process followed by complexation with  $\text{Br}^-$ , or gold is simply dissolved by CTAB. To eliminate the possibility that gold colloids formed during ablation are subsequently dissolved by CTAB ( $\text{Br}^-$  is a strong complexating agent for gold) to yield  $\text{AuBr}_4^-$  or  $\text{AuBr}_2^-$ , the following control experiment was performed. A colloidal solution in pure chloroform, prepared by laser ablation, was mixed with CTAB to yield a  $10^{-3}$  M solution. It is observed that CTAB does indeed dissolve the colloidal gold: the color of the colloidal solution changes from red-purple to almost colorless which suggests that  $\text{AuBr}_2^-$  is formed. The formation of  $\text{AuBr}_4^-$  was never observed. However, the process is extremely slow and it takes several hours to completely dissolve the colloidal gold. Since the formation of  $\text{AuBr}_2^-$  from gold requires an oxidizing agent, possibly oxygen, the same experiment was performed under a nitrogen atmosphere. In this case, we were not able to dissolve the gold during the time course of the experiment (1 day), which suggests that oxygen is the oxidizing agent. In the ablation process, on the other hand, the formation of  $\text{AuBr}_4^-$  is instantaneous, even in the absence of oxygen, as is indicated by the bright yellow plume of the material that is generated in the laser focus. In fact, the formation of gold nanoparticles was never observed at any point during the ablation process. Therefore, we must conclude that ionization of gold is most probably the first step in the ablation process.

Hence, based on this observation we propose the following mechanism for the ablation process. At low concentrations of CTAB gold is first ionized, by the strong laserfield to  $\text{Au}^+$ , which is subsequently converted into gold and  $\text{Au}^{3+}$  through disproportionation.



In the absence of any stabilizing agents the  $\text{Au}^{3+}$  is reduced very rapidly to gold, depending on the reducing power of the solvent. While the nature of the reducing agent is at present unknown, it is clear that several compounds should be able to reduce gold(III) because of its very high oxidation potential. After reduction colloid formation can start following the dynamic formation mechanism. This is consistent with the formation of colloidal gold in pure chloroform. By the addition of CTAB, and hence bromide ions, the gold(III) can effectively be stabilized by complexation with the bromide ion leading to the formation of tetrabromo aurate. Because of the lower oxidation potential of tetrabromo aurate, reduction by the solvent does not occur. The disproportionation step, which will always lead to gold formation, is consistent with the observation of precipitation at the bottom of the cell. At even higher concentrations  $\text{Au(I)}$  ions are stabilized and prevent disproportionation to gold and gold(III).

This study leads to a more detailed explanation of the laser ablation process. Moreover, it opens up other possibilities. For example, with this mechanism it is possible to create other gold(III) and gold(I) complexes as long as the ablation process is done with the proper ligands. However, it must be realized that the formation of ionic compounds through laser ablation depends on the nature of the solvent. Any solvent with strong reducing properties does not lead to the formation of gold complexes.

## 4.6 Conclusions

The experimental set-up for a laser ablation process was reviewed in this chapter. Laser ablation provides a rapid and simple method for the fabrication of stable colloidal solutions of the coinage metals gold and silver. However, the colloidal copper solutions produced by laser ablation needs extra stabilization. This chapter also reviewed the Dynamic Formation Mechanism and the Laser-induced Size Reduction Process, being proposed in literature. A detailed study of laser ablation of gold in chloroform solutions of quaternary ammonium salts leads to a more detailed description of the laser ablation process and also opened up other possibilities. Laser ablation of gold in a solution of CTAB in chloroform can lead to the formation of cetyltrimethylammonium tetrabromo aurate when the concentration of CTAB in chloroform is small. At higher concentrations of CTAB, cetyltrimethylammonium dibromo aurate is possibly formed. These observations have led to the conclusion that the first step in the laser ablation process is the formation of gold ions. The reducing strength of the solvent and the amount of CTAB added, determines if colloid formation occurs or complexation. The laser ablation mechanism suggests the formation of any gold(III) and gold(I) complex, as long as the ablation process is done in the presence of the right amount of ligands.



## 5. PREPARATION OF SMALL METAL PARTICLES USING ULTRASOUND

### 5.1 Introduction

An alternative procedure for the preparation of small metal particles to the other methods described in the previous chapters is the preparation and the formation of gold nanoparticles in aqueous solutions using an ultrasound field [86–88]. This chapter discusses the formation of colloidal gold using ultrasound with the explanation of the ultrasonic irradiation phenomenon as described by Caruso *et al.* [88]. Furthermore, a detailed study of the oxidation of solid gold in chloroform solutions of cetyltrimethylammonium bromide (CTAB) using ultrasonic irradiation is explained. We describe in this chapter that by using ultrasound bulk gold can effectively be oxidized to form gold complexes and only after the addition of a suitable reducing agent to the sonicated solution, the formation of gold colloids is observed.

### 5.2 Sonochemical fabrication of colloidal gold

The reduction of  $\text{AuCl}_4^-$  to colloidal gold in the presence of aliphatic alcohols and sodium dodecyl sulfate in aqueous solutions has been studied extensively by Caruso *et al.* [88]. The sonication was performed with a 20 kHz Branson 450 Probe Sonifier (Branson ultrasonic cooperation) although a simple ultrasonic bath<sup>1</sup> for cleaning glassware is sufficient to reduce the gold salt to colloidal gold. An absorption spectrum taken from a solution of  $2 \times 10^{-4}$  M  $\text{AuCl}_4^-$  and 1 M ethanol

---

<sup>1</sup> The same results were obtained using a Branson Sonifier 2510.

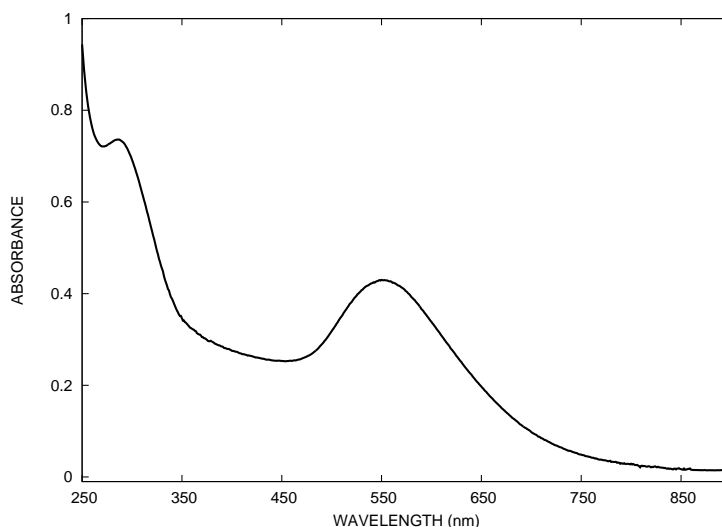
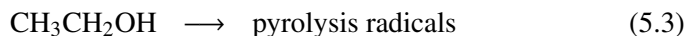


**Fig. 5.1:** UV-Vis absorption spectrum of a sonicated solution of  $2 \times 10^{-4}$  M  $\text{AuCl}_4^-$  and 1 M ethanol in water.

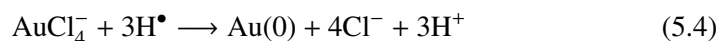
in water sonicated for 5 minutes with the Branson 450 Probe Sonifier is shown in Figure 5.1. The characteristic plasmon band for gold colloids with  $\lambda_{\text{max}}$  around 550 nm is quite broad because the nanoparticles are polydisperse in size and shape [88]. The mechanism of the fabrication of the gold nanoparticles depends on the pyrolysis of water and other organic compounds present in the aqueous solution resulting in the formation of free radicals at high temperatures and pressures. When water is sonicated in the presence of ethanol, the following reactions proceed [86,88]



These radicals can reduce gold(III) ions into gold(II), gold(I), and finally gold(0). However, if  $\text{AuCl}_4^-$  is sonicated in water without the addition of ethanol, some colloidal gold is produced according to three separate near diffusion-controlled



one-electron transfer steps with  $\text{H}^\bullet$  as the primary reducing species [88]



In the presence of ethanol a more complex sequence of three separate one-electron transfer reactions may be summarized [86, 88]



The reduction of  $\text{AuCl}_4^-$  to colloidal gold according to the reactions 5.4 and 5.5 is simplified and the particle growth is much more complex than these reactions indicate. For example, in addition to these reactions it is proposed that alcohol adsorbs onto gold colloids and reduces adsorbed Au(III) [88]. Moreover, disproportionation reactions from gold(II) to gold(III) and gold(I) occur.

The rate of gold(III) reduction can be controlled by the ultrasound irradiation conditions such as the temperature and the ultrasound intensity. The size of the gold nanoparticles can be controlled by changing the alcohol concentration and alkyl chain length [88]. Therefore, this method is useful in the rapid fabrication of metal nanoparticles, but the particles are polydisperse which is a problem for applications where monodisperse solutions are required.

### 5.3 Oxidation of solid gold using ultrasound

Gold is one of the most stable coinage metals because it is not attacked by either oxygen or sulphur at any temperature [27]. The dissolution of gold is essential for its extraction and recovery [89]. Two conditions have to be fulfilled to dissolve bulk gold which are an oxidizing agent and a suitable ligand. For example, gold will not dissolve appreciably in either hydrochloric or nitric acid alone, but dissolves in aqua regia to give tetrachloroauric(III) acid. In organic solutions, these conditions also have to be fulfilled.

The nobility of the coinage metals is due to the high positive value of the redox potential [90]. However, as it was described in chapter 2, these high redox potentials can be significantly lowered in the presence of a nucleophile. Furthermore, size

effects can also result in a lowering of the reduction potential value making these metals more susceptible towards oxidation [91]. In fact, it has been described that colloidal gold can be dissolved in water in the presence of a nucleophile and that gold (and other noble metals) dissolves in polar organic solvents in the presence of halogens and corresponding halides [92–95].

In this section a detailed study on the oxidation of solid gold in chloroform solutions of the surfactant cetyltrimethylammonium bromide (CTAB), with the aid of ultrasound is described. Furthermore, it is shown that this procedure can form the basis for the preparation of gold colloids in organic solvents.

### 5.3.1 Experimental Results

Chloroform was chosen as a solvent because it can dissolve CTAB in high concentrations. Experiments were performed with CTAB concentrations of  $10^{-3}$ ,  $10^{-2}$  and  $10^{-1}$  M. For example, in a typical experiment, a piece of solid gold (99.99 % purity, approximately 1 g) was added to one of the CTAB solutions and ultrasonic vibrations were transmitted continuously into the solution by means of the Branson 450 Probe Sonifier for 15 minutes. For the lowest concentrations of CTAB in chloroform ( $10^{-3}$  M), the solution turned slightly yellow after 15 minutes, while the chloroform solution with 0.1 M CTAB became bright yellow. In the absence of sonication, no observable reaction occurred, even after several days. The yellow color of the sonicated solution seems to indicate that a Au(III) compound was formed. UV-Vis absorption spectroscopy shows a strong absorption at 387 nm with a distinct shoulder at 458 nm which is indicative of the formation of a Au(III) compound, more specifically the  $\text{AuBr}_4^-$  anion. Furthermore, this spectrum is basically identical with that of  $\text{HAuBr}_4$  solubilized in chloroform by CTAB as can be seen in Figure 5.2. Note also that the type of sonifier used is not crucial, but the reaction time is dependent upon the sonification power. A simple ultrasonic bath (e.g. a Branson Sonifier 2510) for cleaning glassware is sufficient to oxidize the gold. In this case however, using a Branson Sonifier 2510, the reaction time is several hours.

The formation of tetrabromo aurate as a function of time by UV-Vis absorption was also monitored, by taking a UV-Vis absorption spectrum every minute during

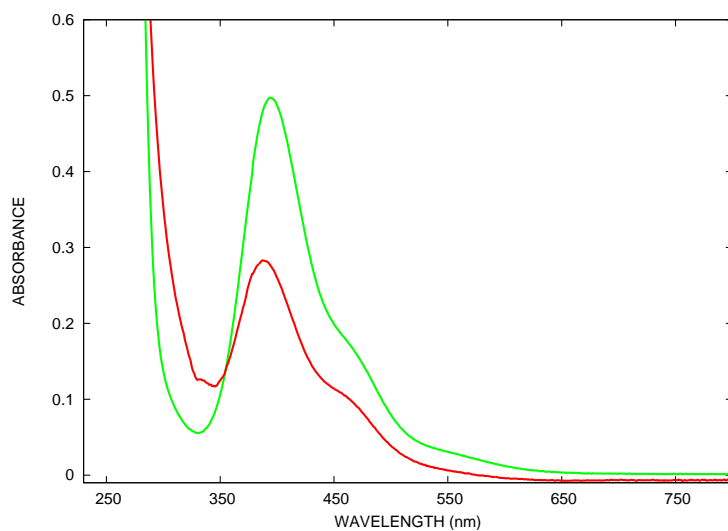


**Fig. 5.2:** UV-Vis absorption spectra of a sonicated solution (0.1 M CTAB in CHCl<sub>3</sub>) (red line) and HAuBr<sub>4</sub> dissolved in a 0.1 M CTAB/CHCl<sub>3</sub> solution (green line).

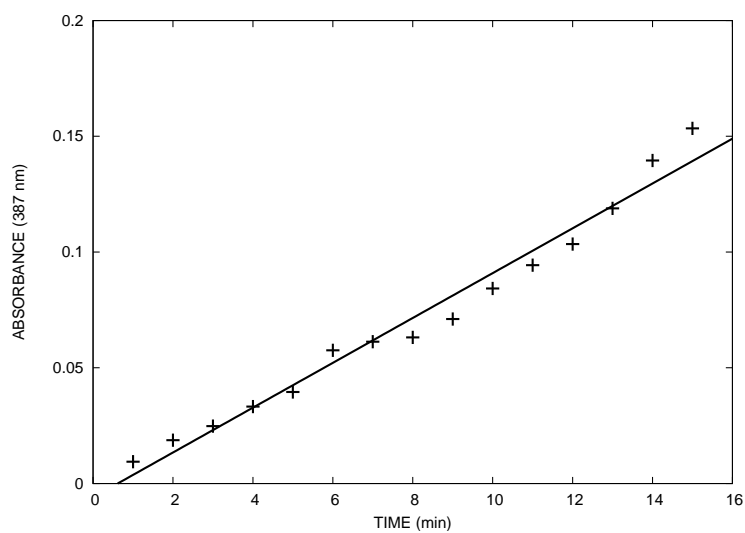
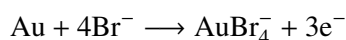


**Fig. 5.3:** UV-Vis absorption measured at 387 nm every minute during 15 minutes sonication of a piece of solid gold in a 0.1 M CTAB in CHCl<sub>3</sub> solution.

the 15 minutes of sonication. The results are visualized in Figure 5.3 where the UV-Vis absorption was always measured at 387 nm. During these 15 minutes, the concentration of  $\text{AuBr}_4^-$  was found to increase linearly with time during the time course of the experiment, indicating zero order kinetics.

Since the formation of  $\text{AuBr}_4^-$  from gold requires an oxidizing agent, probably molecular oxygen in air, the same experiment was performed under a molecular nitrogen atmosphere. In this case, no oxidation of gold was observed during the time course of the experiment, which suggests that molecular oxygen is indeed the oxidizing agent. This also indicates why sonication is absolutely necessary because during sonication the reaction mixture is continuously provided with oxygen. In Chapter 2 we saw that the high redox potential of gold is significantly lowered in the presence of a nucleophile and that the reaction with oxygen as oxidizing agent probably takes place by adsorption of oxygen onto the gold surface followed by the reaction of this surface layer with a suitable ligand. Hence, the reaction to oxidize gold to gold(III) in the presence of the bromide ions is written as



### 5.3.2 Gold colloid formation

One of the advantages of the method described above is that it provides a unique and very simple procedure to transfer tetrabromoauroate into organic solvents, leading to the possibility of colloid formation in a variety of organic solvents. While traditional methods for gold colloid formation are usually water-based, or require a two-phase method, the procedure as described below directly leads to colloid formation in the organic solvent [18,66].

Upon addition of a small amount of a suitable reducing agent to the sonicated gold/CTAB/chloroform solution, gold colloids are formed. For example, after adding a small amount sodium borohydride ( $40\ \mu\text{L}$  1 M  $\text{NaBH}_4$  in water) to 10 mL of the sonicated solution, the yellow color turns reddish-pink almost immediately, indicative of colloidal gold formation. However, after adding a small amount of hydrazine hydrate ( $40\ \mu\text{L}$ ) to the sonicated solution, the yellow solution initially becomes colorless, probably due to the formation of a Au(I) complex, but after 1

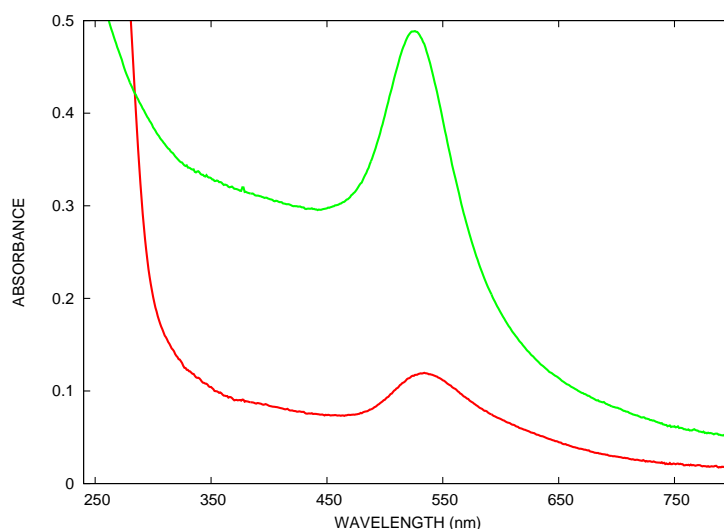


**Fig. 5.4:** UV-Vis absorption spectra from a sonicated solution after the addition of a small amount hydrazine hydrate (red line) and after the addition of a small amount  $\text{NaBH}_4$  in water (green line).

min the solution turns reddish-purple which is again indicative of colloidal gold formation. UV-Vis absorption spectra visualized in Figure 5.4 taken from sonicated gold/CTAB/chloroform solutions after the addition of the reducing agents  $\text{NaBH}_4$  or hydrazine hydrate show a strong plasmon resonance at 525 nm and 535 nm respectively. Dynamic light scattering (DLS) experiments gave typical average diameters of 28 nm for the sonicated solution after addition of  $\text{NaBH}_4$  and 32 nm for the sonicated solution after addition of hydrazine hydrate (Figure 5.5). An ESEM picture taken from a sonicated solution after the addition of  $\text{NaBH}_4$  can be seen in Figure 5.6 showing polydisperse spherical gold nanoparticles. Atomic force microscopy (AFM, contact mode)<sup>2</sup> from a sonicated solution after the addition of hydrazine hydrate shows spherical nanoparticles with an average diameter of 18 nm, but with a significant size dispersity ( $18 \pm 5\text{ nm}$ ) (Figure 5.7). The difference between the DLS and AFM measurements can be attributed to the CTAB molecules stabilizing the gold colloids in the chloroform solution. The explanation

<sup>2</sup> AFM images were taken with a USPM Scan Atomic Force Microscopy from Quesant Instrument Corporation available in the laboratory.

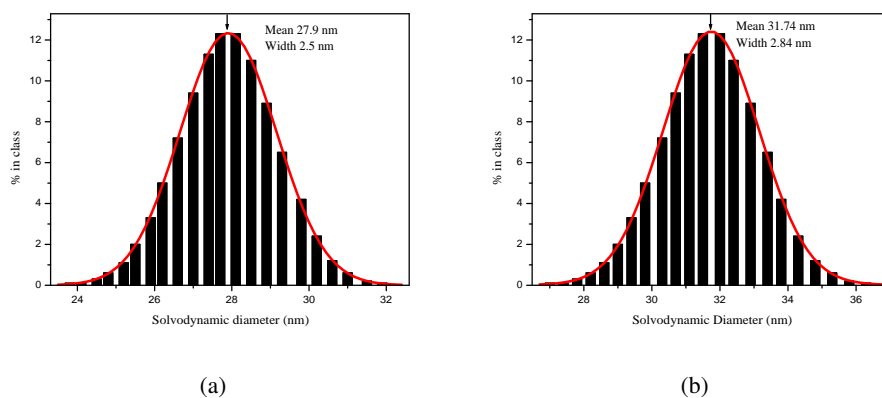


**Fig. 5.5:** Dynamic Light Scattering measurements of a sonicated solution after the addition of NaBH<sub>4</sub> (a) and hydrazine hydrate (b).

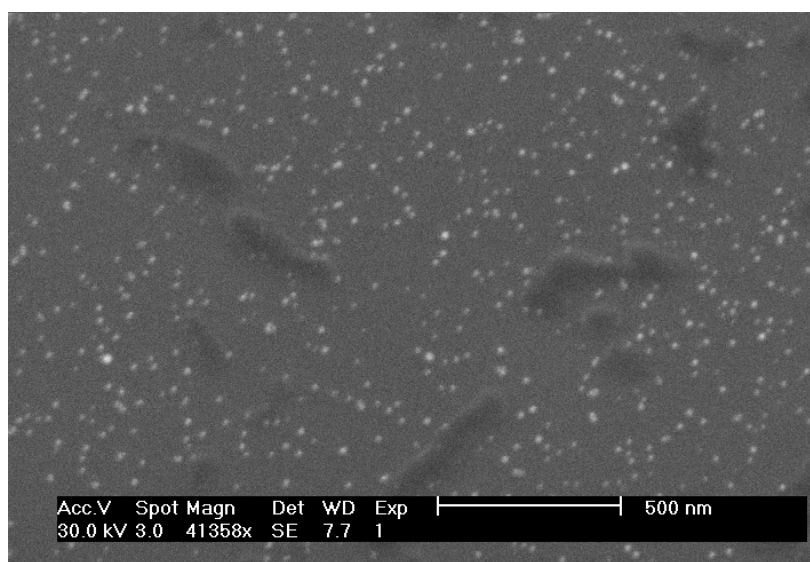


**Fig. 5.6:** ESEM picture taken from a sonicated solution after the addition of NaBH<sub>4</sub> showing gold nanoparticles.

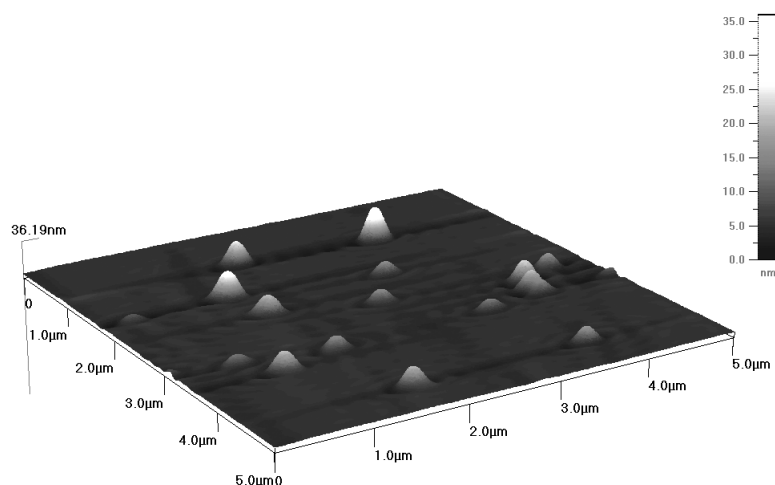


**Fig. 5.7:** AFM image (contact mode) taken from the solution after the addition of hydrazine hydrate showing gold nanoparticles. Z-Height  $\sim 20$  nm.

lies in the fact that DLS experiments measures the solvodynamic radius which is normally close to, but always larger than the exact geometrical radius of the gold nanoparticles.

However, this process can be utilized as an easy preparation method for creating gold colloids after adding a suitable reducing agent to the  $\text{AuBr}_4^-/\text{CTA}^+$  in chloroform system whereby gold colloids are manufactured and stabilized immediately in chloroform.

## 5.4 Conclusions

The sonochemical fabrication of gold colloids in an ultrasound field and the theoretical description was reviewed in this chapter. Furthermore, it was shown in a detailed study that solid gold is effectively oxidized in concentrated chloroform solutions of cetyltrimethylammonium bromide with the aid of sonication, leading to the formation of cetyltrimethylammonium tetrabromo aurate. The  $\text{Br}^-$  from CTAB

is acting as a nucleophile and oxygen in the air is responsible for the oxidation of the bulk gold. Moreover, this process was utilized as an easy preparation method for creating gold colloids after the addition of a suitable reducing agent to the sonicated solution whereby gold colloids were fabricated and stabilized immediately in chloroform by CTAB molecules. These nanoparticles were fully characterized by UV-Vis spectroscopy, dynamic light scattering, AFM and ESEM.

The sonication methods described in this chapter yield polydisperse gold nanoparticles which can be a problem for some applications when monodisperse solutions of gold nanoparticles are required.



## **6. WET CHEMICAL SYNTHESIS OF GOLD NANORODS**

### **6.1 Introduction**

The optical, electronic and catalytic properties of nanostructured materials depend mainly on their size and shape whereas these properties can be adjusted by shape control [53, 62–64]. Therefore, the optical properties of gold nanorods based on experimental results are discussed in this chapter to confirm the theory described in chapter 2. Moreover, this chapter gives a detailed experimental study of a wet chemical synthesis technique to prepare gold nanorods based on a seed-mediated growth method in the presence of the surfactant cetyltrimethylammonium bromide [96]. Shape control of gold nanorods is induced by manipulating the length and aspect ratios of the gold nanorods by varying the surfactant concentration. Hence, we were able to synthesize high aspect ratio gold nanorods having average lengths over more than 1  $\mu\text{m}$ .

### **6.2 Optical properties of gold nanorods**

As described in chapter 2 for gold nanorods, the optical absorption spectra split into two surface plasmon resonances which are a longitudinal mode along the long axis of the rod and a transverse mode perpendicular to the first mode [53, 54]. Two plasmon resonances can be seen clearly in the UV-Vis spectrum in Figure 6.1 taken from a solution of gold nanorods prepared by a seed-mediated growth method which will be described in the next section. The corresponding ESEM image is

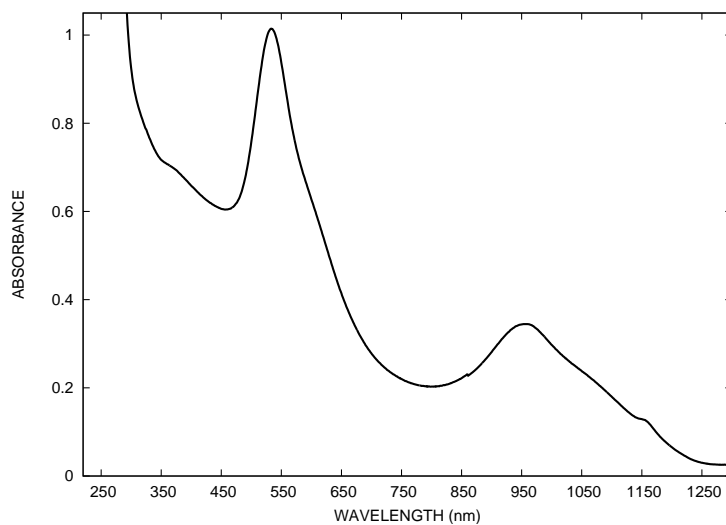


**Fig. 6.1:** UV-Vis absorption spectrum taken from gold nanorods prepared by the seed-growth method in a 0.01 M CTAB in H<sub>2</sub>O solution.

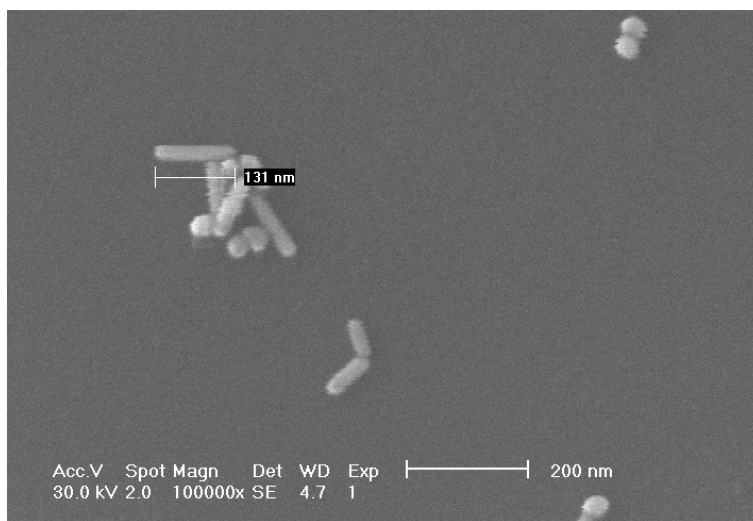


**Fig. 6.2:** ESEM image taken from gold nanorods prepared by the seed-growth method in a 0.01 M CTAB in H<sub>2</sub>O solution.

shown in Figure 6.2 visualizing gold nanorods with average aspect ratios of 3.5. The first theoretical calculations to explain the optical properties of gold nanorods were performed by Gans who extended the Mie theory to prolate and oblate spheroidal particles averaged over all orientations [52]. The theory of Gans predicts that the longitudinal resonance shifts to longer wavelengths with increasing aspect ratio (the length to diameter ratio), whereas the transverse resonance shifts only slightly to shorter wavelengths [52].

We can summarize that spherical gold nanoparticles and gold nanorods not only differ in shape but also in terms of the optical properties. Spherical gold nanoparticles show only one size dependent absorption maximum, whereas gold nanorods have two maximums dependent on the aspect ratio with the longitudinal mode shifted to longer wavelengths.

### 6.3 Two-step synthesis of high aspect ratio gold nanorods

There are several methods to prepare gold nanorods reported in literature. For example, they can be synthesized in rigid templates such as nanoporous matrices or in the presence of surfactants by electrochemical or seed-mediated growth methods [51, 96–101]. Surfactant based methods are usually considered as being more practical for large-scale synthesis. Gold nanorods with aspect ratios as high as 18 with lengths of a few 100 nanometers have been reported where the nanorods were synthesized by using a multi-step seed-mediated growth method [96, 100]. Another group reported the synthesis of gold nanorods with aspect ratios of 10 in a two-step method using a binary surfactant mixture [101]. This method yields pure nanorods in contrast to the previous method where a mixture of differently shaped particles is obtained. In our experiments we used a two-step surfactant based method to prepare gold nanorods with extremely high aspect ratios ( $> 20$ ) and average lengths of more than a micrometer. Our method is a simplified procedure of the procedures described by Jana *et al.* [96, 100]. It yields a mixture of spherical, triangular and rodlike nanoparticles, with the predominant formation of rodlike particles at high surfactant concentrations. Changing the surfactant concentration was shown to vary the length of the nanorods formed.

### 6.3.1 Experimental procedure

The seed solution was prepared by mixing 20 mL of a  $2.5 \times 10^{-4}$  M  $\text{HAuCl}_4 \cdot 3\text{H}_2\text{O}$  and  $2.5 \times 10^{-4}$  M  $\text{Na}_3\text{citrate}$  in water with 400  $\mu\text{L}$  of a freshly prepared icecold water solution of 0.1 M  $\text{NaBH}_4$ . The color of the solution immediately changes from yellow to orange. The growth solution was prepared by adding an appropriate amount of cetyltrimethylammonium bromide (CTAB) (to yield overall CTAB concentrations of  $10^{-3}$ ,  $10^{-2}$ , 0.1 and 1 M) to a 10 mL solution of  $2.5 \times 10^{-4}$  M  $\text{HAuCl}_4 \cdot 3\text{H}_2\text{O}$  in water. To dissolve all the CTAB, the solution can be heated slightly, but after dissolution the solution is cooled down to room temperature ( $20^\circ\text{C}$ ) again, except for the 1 M CTAB solution which was kept at  $35^\circ\text{C}$  to prevent precipitation of CTAB. Next 40  $\mu\text{L}$  of 0.1 M L(+)-ascorbic acid is added to the solution. The bright yellow solution immediately turns colorless, due to the formation of a Au(I) complex with CTAB. Finally the gold nanorods were prepared by adding 25  $\mu\text{L}$  of the seed solution to 10 mL of the growth solution. After gentle mixing, the solution is allowed to stand for several hours to complete the growth of the gold nanorods.

### 6.3.2 Experimental results

The advantage of the method being described in this chapter over the procedure reported by Jana *et al.* is that we were able to synthesize very long gold nanorods. Moreover, Jana *et al.* describe a multistep procedure, requiring several seed- and growth cycles while the method described here requires only a single seed and growth step. Hence, we were able to study the role of the CTAB concentration on the length of gold nanorods formed. The synthesis of the gold nanorods was performed in the presence of different amounts of CTAB, and depending on its concentration, a difference in the amounts and sizes of the gold nanorods were observed. The UV-Vis spectra of the gold nanorod mixtures in the presence of  $10^{-3}$ ,  $10^{-2}$ , and 0.1 M CTAB are shown in Figure 6.3. All spectra are quite complex although a transversal and longitudinal plasmon band typical for rodlike particles is clearly seen.

Two possible mechanisms for rod formation have been proposed in literature: a direct surfactant templating mechanism with or without an electric-field directed

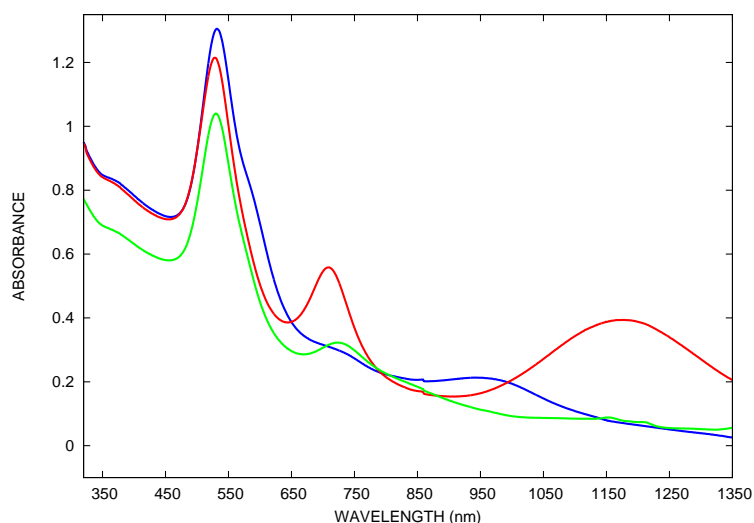


**Fig. 6.3:** UV-Vis spectra of solutions containing nanorods, prepared in the presence of  $10^{-3}$  (green line),  $10^{-2}$  (red line), and 0.1 M (blue line) CTAB.

growth of gold nanorods [100, 102] and a mechanism suggesting the lowering of the interfacial tension of a specific crystal facet [103]. Since the formation of rods is already observed well below the critical micelle concentration of CTAB, a templating mechanism seems unlikely. However, a clear dependence of rod length on CTAB concentration is observed with the rod length increasing significantly upon increasing CTAB concentration. Moreover, at CTAB concentrations higher than the sphere-to-rod transition [104, 105], both rod diameter and length increase drastically, which seems to suggest that a templating mechanism does influence rod formation.

This was confirmed by scanning electron microscopy (ESEM). A solution of 0.001 M CTAB showed mainly the presence of spherical nanoparticles of 10 nm diameter with only a small amount of nanorods of an average length of 110 nm and width of 30 nm. However, with increasing concentration of CTAB we clearly observe an increase of nanorod formation and nanorod length. Thus, a solution containing 0.01 M CTAB gave nanorods with an average length of 220 nm and 40 nm while a solution containing 0.1 M CTAB yielded 400 nm length and 18 nm width. Although the amount of nanorods (as compared to spherical and triangular particles)

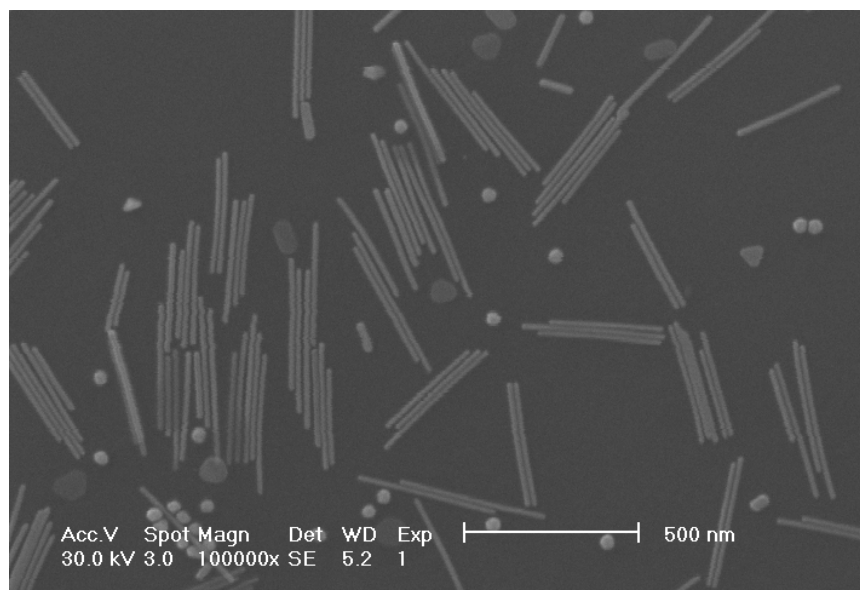
Concentration CTAB (M) Growth solution	Average Length (nm)	Average Aspect ratio
$10^{-3}$	110	3.5
$10^{-2}$	220	5.5
$10^{-1}$	450	25
1	> 1000	25

**Tab. 6.1:** Nanorods lengths and aspect ratios, as measured by SEM, for different surfactant concentrations.

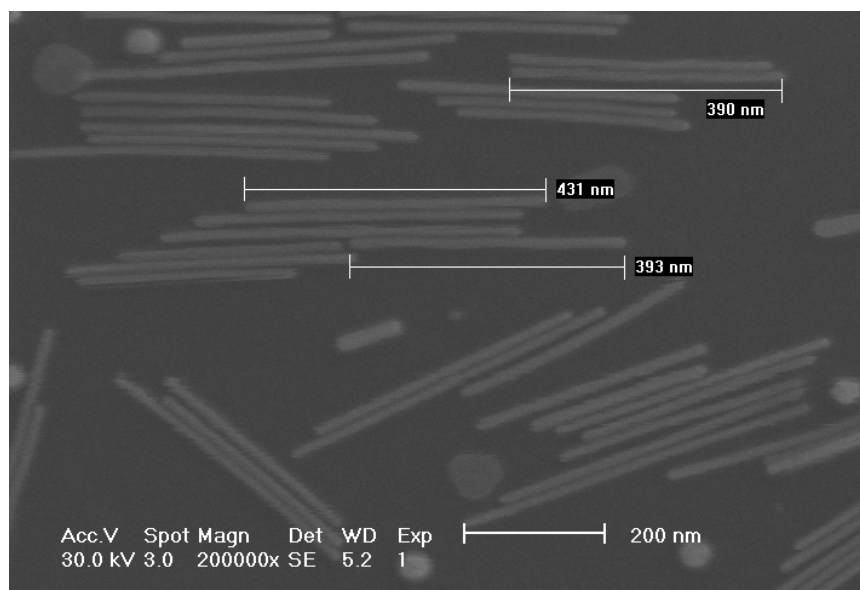
increases with increasing CTAB concentration, we still observe a small amount of nanoparticles with atypical shapes as can be seen in the ESEM images in Figure 6.4.

In the presence of 1 M of CTAB, the solution containing the nanorods is only slightly colored and the absorption spectrum is rather featureless in the visible and near infrared. Scanning electron microscopy images show the formation of extremely long nanorods with average lengths of over 1 micron and 60 nm width (Figure 6.5), with a small amount of atypically shaped particles still present. The absence of significant absorption in the visible and near infra red is due to the fact that nanorod formation shifts the plasmon resonance to lower energies, whereas the high energy plasmon resonance decreases in intensity.

The average lengths and aspect ratios of the different nanorods as measured by SEM are summarized in Table 6.1 for each CTAB concentration. Note the extremely high aspect ratios and nanorod lengths at high CTAB concentration. We are not aware of any other simple surfactant based method that yields gold nanorods of these dimensions and aspect ratios. In this respect, this method could be very useful for large scale-synthesis of nanorods. However, it has to be realized that this synthetic method does not yield pure nanorods and an additional purification step, such as centrifugation, might be necessary. Therefore, UV-Vis absorption spectra taken from a 0.1 M CTAB solution before and after a first (and second) centrifugation can be seen in Figure 6.6. A gold nanorod solution was used where the longitudinal plasmon resonance around 850 nm is not clearly distinguished from the transverse resonance around 530 nm. However, after a first centrifugation at 1250 rpm for 30 minutes with the pellet being redissolved in 10 mL of Milli-Q wa-

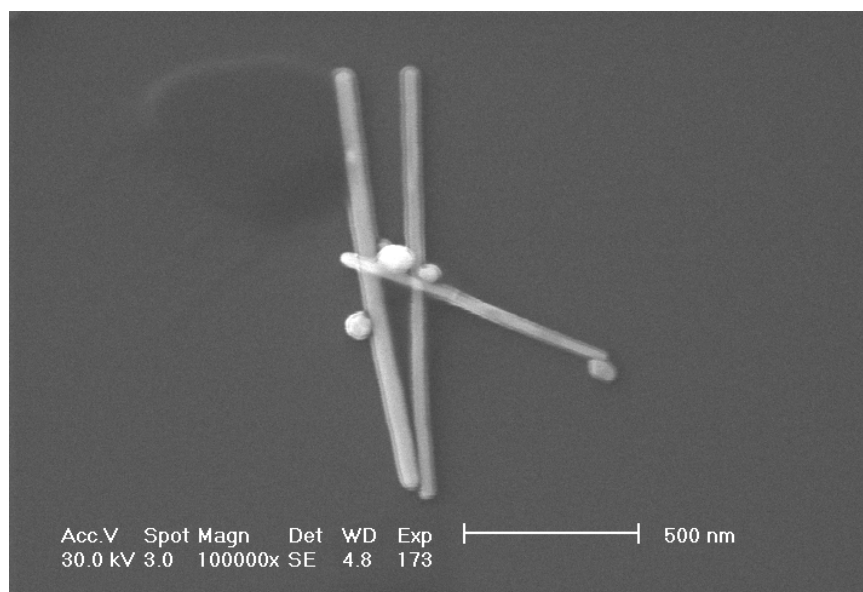


(a)

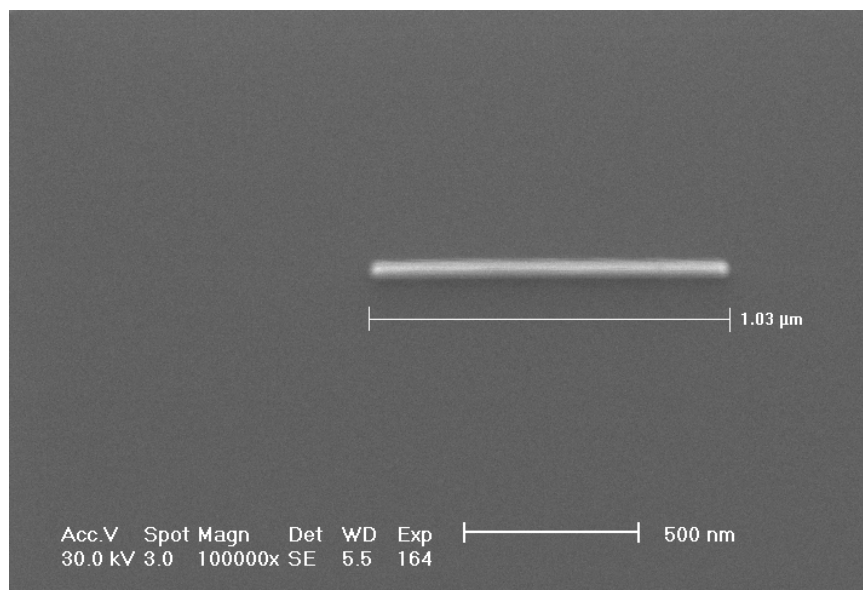


(b)

**Fig. 6.4:** ESEM images taken from gold nanorods prepared by the seed-growth method in a 0.1 M CTAB in H<sub>2</sub>O solution.



(a)



(b)

**Fig. 6.5:** ESEM images taken from gold nanorods prepared by the seed-growth method in the presence of 1 M CTAB in H<sub>2</sub>O solution.



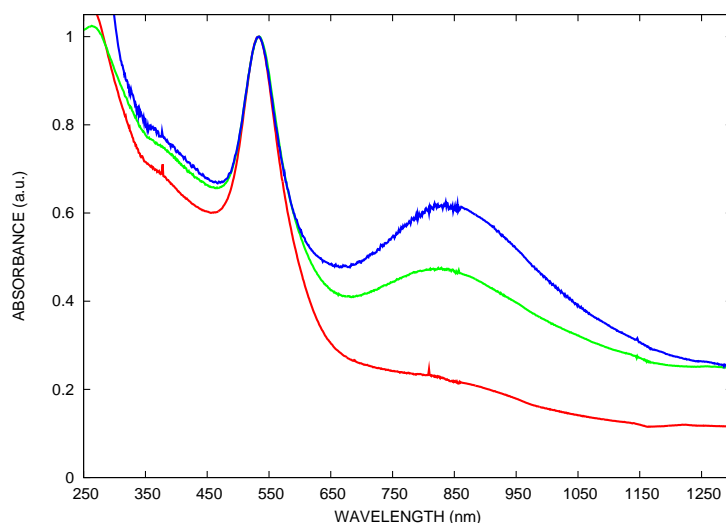


**Fig. 6.6:** UV-Vis absorption spectra of gold nanorods prepared by the seed-mediated growth method from a 0.1 M CTAB in  $H_2O$  solution before centrifugation (red line), after a first centrifugation at 1250 rpm for 30 min (green line) and after a second centrifugation at 700 rpm for 30 min (blue line). The spectra are normalized.

ter, the longitudinal plasmon resonance can now be clearly distinguished from the transverse one. After a second centrifugation at 700 rpm for 30 minutes with the pellet again redissolved in 10 mL of Milli-Q water, the longitudinal plasmon resonance is even more pronounced in relation to the transverse plasmon resonance.

## 6.4 Conclusions

The optical properties of gold nanorods were reviewed with our experimental results for synthesizing gold nanorods. The UV-Vis absorption spectra clearly show two plasmon resonances for nanorods having average lengths of 110 nm and aspect ratios of 3.5. The UV-Vis absorption spectra were confirmed by ESEM images. Furthermore, this chapter gave a two-step synthesis technique of high aspect ratio ( $> 20$ ) gold nanorods based on a seed-mediated growth procedure. Furthermore, the shape control of the gold nanorods is induced by manipulating the length and

aspect ratios of the gold nanorods by varying the surfactant concentration which is cetyltrimethylammonium bromide. This synthetic method does not yield pure gold nanorods, but we are not aware of any other simple surfactant based method yielding gold nanorods of these dimensions. Hence, together with a purification step, this procedure is useful to prepare high aspect ratio gold nanorods in large amounts.

## **7. WET CHEMICAL SYNTHESIS OF GOLD NANOSHELLS**

### **7.1 Introduction**

A specific class of nanoparticles are nanoshells which are composed of a dielectric core (e.g. silica) coated by a thin metallic film (e.g. gold). Hence, the synthesis of these particles involves firstly the formation of the dielectric core (e.g. silica nanoparticles) which is followed by an attachment of very small colloidal gold particles acting as nucleation sites for further reduction of a gold salt so that the dielectric core nanoparticles become covered completely by a continuous metallic film. In this chapter we discuss the wet chemical synthesis of gold nanoshells as proposed by Halas *et al.* and Van Blaaderen *et al.* [60, 106, 107]. We were able to coat individual silica nanoparticles simultaneously with a continuous gold film. The optical properties from these gold nanoshells are tunable over a wide range of the optical spectrum making them potential valuable candidates for sensor applications.

### **7.2 Optical properties of gold nanoshells**

The optical properties of nanoshells depend strongly on the size of the dielectric core, the thickness of the metallic thin film and the surrounding media [60]. UV-Vis absorption spectra taken from different silica core, gold nanoshell solutions prepared in the laboratory are shown in Figure 7.1. In contrast to colloidal gold where the surface plasmon resonance is not strongly dependent on the particle

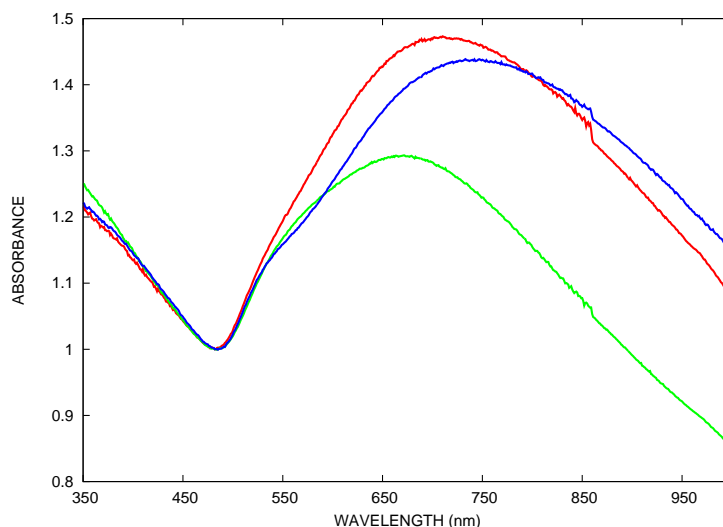


**Fig. 7.1:** UV-Vis spectra taken from different silica core, gold nanoshell solutions. The spectra are normalized.

size, gold nanoshells allow a tuning of the surface plasmon resonance across the visible and infrared [76]. This depends on the variation of the shell thickness on the dielectric core. Calculations performed on the optical resonances of silica core, gold shell nanoparticles have demonstrated that when the shell thickness decreases, the optical absorption is shifted to longer wavelengths [60, 108]. Therefore, gold nanoshells are ultimately useful in nanosensor applications. Moreover, gold coated silica nanoparticles are nowadays receiving much interest because of their possible applications in cancer detection and treatments [56, 57].

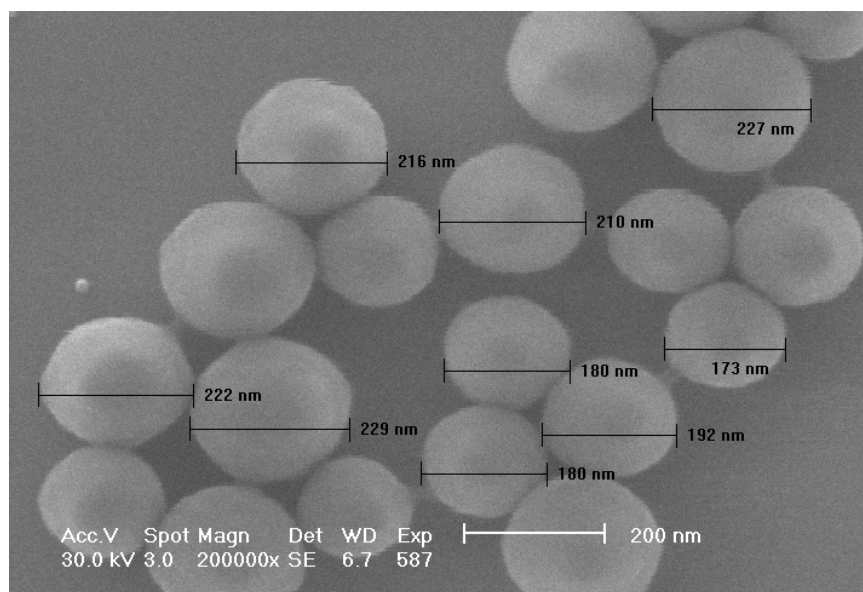
### 7.3 Experimental Procedure & Results

Silica nanoparticles were prepared using the Stöber-Fink-Bohn procedure [109]. Firstly, pure ethanol (50 mL) was mixed with 25% ammonia (5 mL) and 1.5 mL tetraethylorthosilicate ( $\text{Si}(\text{OC}_2\text{H}_5)_4$ ) was then added under vigorous stirring to the solution which was left to react for at least twelve hours. The surfaces of the silica nanoparticles ( $\text{SiO}_2$ ) were functionalized by adding 50  $\mu\text{L}$  3-aminopropyl-

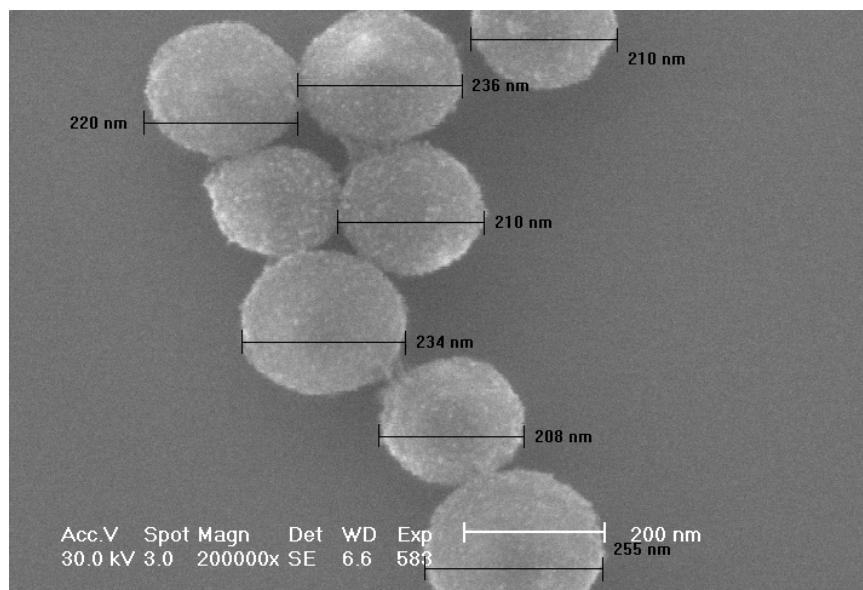
trimethoxysilane (APTMS) to the colloidal suspension which was then gently refluxed for one hour. The APTMS-coated colloidal suspension was purified by repeated centrifugation and redispersion in ethanol. An ESEM image from the APTMS-coated silica nanoparticles is shown in Figure 7.2(a). There is no difference before and after the functionalization of the silica nanoparticles with APTMS. Very small colloidal gold nanoparticles that attach on the APTMS-functionalized silica nanoparticles to become nucleation sites for further reduction of a gold salt were prepared according to the Duff procedure [110]. To 45.5 mL Milli-Q water portions of sodium hydroxide (0.2 M, 1.5 mL), the reducing agent Tetrakis-(hydroxymethyl)phosphonium chloride (THPC, 1 mL of a solution of 1.2 mL of 80% aqueous solution diluted to 100 mL with Milli-Q water) and hydrogen tetrachloroauric acid (2 mL, 25 mM) were added in this order under vigorous stirring. This resulted in the formation of an orange-brown colloidal suspension with the gold nanoparticles being 1-2 nm in diameter [110].

The attachment of the small gold nanoparticles onto the APTMS-functionalized silica cores was done by placing 1 mL of the APTMS-functionalized silica particles dispersed in ethanol in a centrifuge tube along with an excess of the gold nanoparticles (10 mL of the gold colloid solution). The centrifuge tube was shaken gently for five minutes and was then left alone for three hours. This mixture was centrifuged at 2500 rpm and a red-colored pellet was settled at the bottom of the tube. Therefore, the supernatant was taken away carefully with a pasteur pipet, leaving a slightly red-colored pellet, which was redispersed and sonicated in 10 mL Milli-Q water. An ESEM figure of these gold coated APTMS-silica nanoparticles is shown in Figure 7.2(b) with the attachment of the small gold nanoparticles being clearly distinguished from the silica cores.

However, to grow a continuous gold film on the Au-APTMS-silica nanoparticles, a suitable solution containing a reducible gold salt has to be prepared. Therefore, 25 mg potassium carbonate ( $K_2CO_3$ ) was dissolved in 100 mL Milli-Q water and after 10 minutes of stirring, we added 1.5 mL of a solution of 1%  $HAuCl_4$  in Milli-Q water. The total reducible gold salt solution appeared transparent yellow in the beginning, but it became colorless slowly over the course of 30 min, indicating the formation of a gold(I) complex. To 4 mL of this colorless solution 200  $\mu$ L of the solution containing the Au-APTMS-silica nanoparticles was injected while stirring

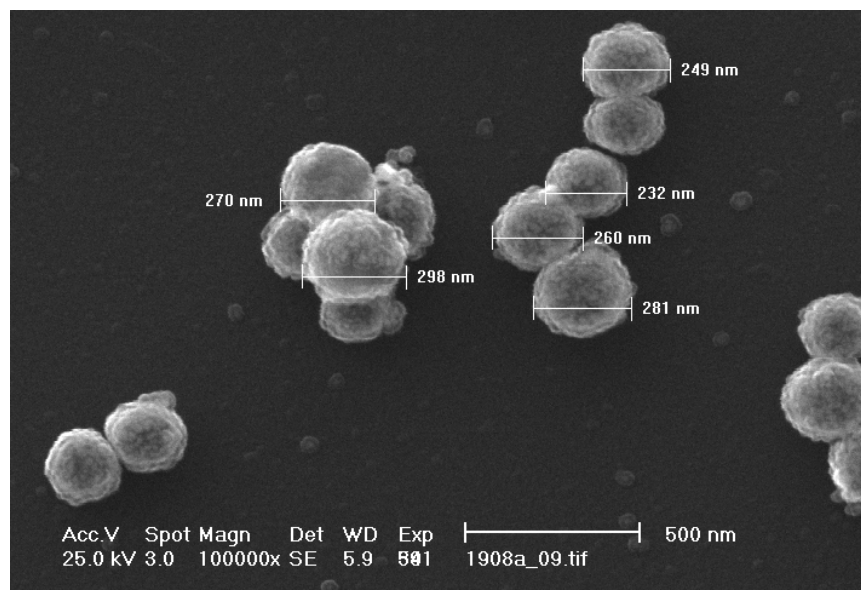


(a)

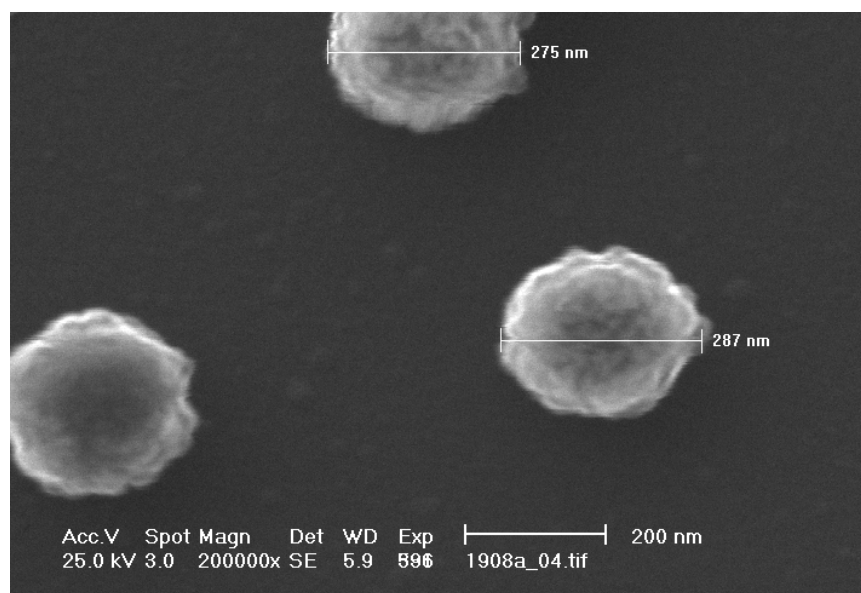


(b)

**Fig. 7.2:** ESEM images taken from APTMS-coated silicaspheres prepared by the Stöber-Fink-Bohn method (a) and gold coated silicaspheres (b).



(a)



(b)

**Fig. 7.3:** ESEM images taken from silica core, gold nanoshells.

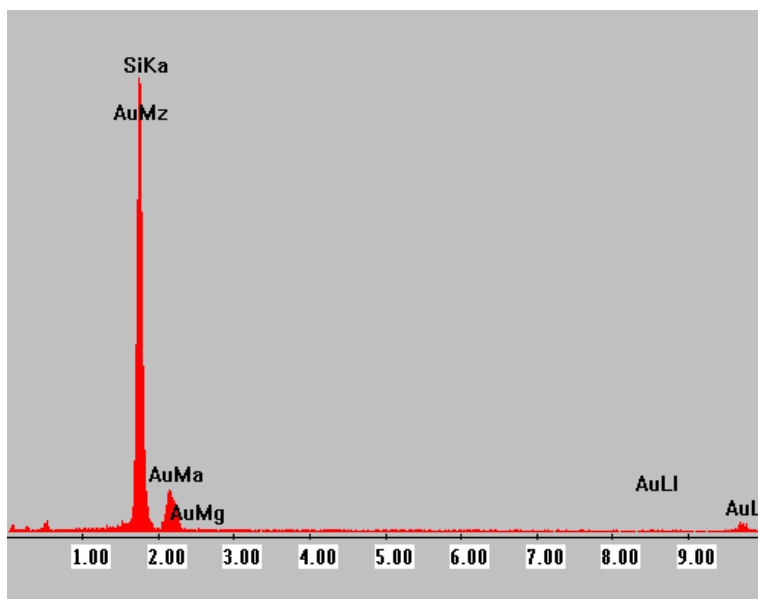


**Fig. 7.4:** EDS/EDX spectrum from a sample of silica core, gold nanoshells showing only silicon and gold peaks.

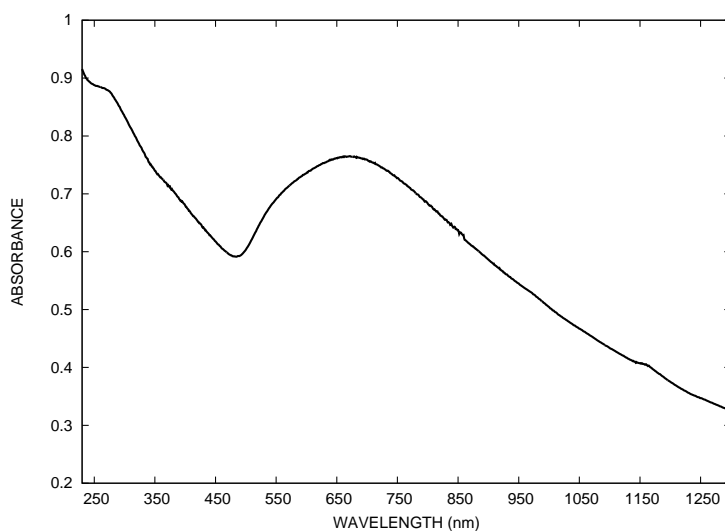


**Fig. 7.5:** UV-Vis spectrum taken from a solution of silica core, gold nanoshells.



vigorously. Subsequently, 10  $\mu\text{L}$  of the reducing agent formaldehyde was added and the solution changed from colorless to blue over the course of 2 till 5 minutes, which is characteristic of gold nanoshell formation. ESEM images of these gold nanoshells are shown in Figure 7.3. Figure 7.4 shows a qualitative analysis from a sample of silica core, gold nanoshells obtained by an Energy Dispersive System/X-ray spectrometer (EDS/EDX)<sup>1</sup> having only characteristic silicium and gold peaks. The thickness of the gold nanoshells synthesized following the procedure described above was approximately 40 nm. The corresponding UV-Vis absorption spectrum is shown in Figure 7.5 where the absorption maximum of the plasmon resonance lies around 680 nm. Hence, we were able to coat silica nanoparticles with a continuous gold layer.

## 7.4 Conclusions

In this last chapter the method to prepare gold nanoshells on the dielectric cores of silica nanoparticles was discussed. It was clear that the plasmon resonance is tunable over a wide range of the ultraviolet and visible region. The gold nanoshells were synthesized by simultaneously covering separate silica nanoparticles with a continuous gold layer. These gold nanoshells were fully characterized by UV-Vis spectroscopy and ESEM measurements. Furthermore, we confirmed with a qualitative EDS/EDX spectrum that a sample of silica core, gold nanoshells only show characteristic silicium and gold peaks.

---

<sup>1</sup> EDS/EDX spectra were taken by Ing. Rudy De Vos from the Department of Metallurgy and Materials Engineering (MTM) with an X-Ray Spectrometer available in the XL30 ESEM-FEG Scanning Electron Microscope.



## GENERAL CONCLUSIONS & SUMMARY

The preparation of nanometer-scale metal particles in solution is a major subject in the field of nanochemistry because of their unusual optical properties and their possible applications in catalysis. Furthermore, they have been proposed as future building blocks in nanotechnology. The typical colors coming from gold and silver nanoparticles were already exploited many centuries ago in the fabrication of glass. Therefore, wet chemical methods to prepare colloids of the coinage metals have been known for a long time and they were based on the reduction of a suitable metal salt in the presence of stabilizers.

The properties coming from gold nanoparticles are very different from the corresponding bulk material. Moreover, the size and shape greatly influences their properties. For example, spherical gold nanoparticles exhibit a single plasmon resonance in the visible region of the spectrum, while rodlike particles exhibit a longitudinal and transversal plasmon resonance.

In this PhD thesis we reviewed colloidal gold from a historical point of view being the starting point for modern colloid chemistry and hence, nanochemistry. The theoretical background gave an explanation of nanomaterials and an introduction in colloid stability with a steady focus on gold nanoparticles. Furthermore, an introduction in gold chemistry, explaining the formation of gold complexes was given. The theoretical background ended with the explanation of plasmon resonances responsible for the remarkable colors of coinage metal sols.

In the experimental part of this PhD thesis we discussed standard techniques to prepare nearly spherical gold colloids, whereby a gold complex is reduced in the presence of a suitable stabilizer. The only possibility to induce chirality is at the level of the stabilizer. Hence, when using chiral stabilizers, this chirality can be

found at the surface of the metal nanoparticles which was confirmed with circular dichroism.

Physicochemical techniques to fabricate gold nanoparticles are respectively laser-ablation of bulk gold in solution and ultrasonic irradiation of a gold salt in aqueous solutions of aliphatic alcohols. In chloroform solutions of cetyltrimethylammonium bromide (CTAB, a cationic surfactant), we were able to oxidize bulk gold.

In the case of laserablation, we were able to oxidize the gold even in the absence of oxidizing agents such as oxygen. Hence, we showed that a first step in gold colloid formation by laserablation is ionization of gold. The formation of gold colloids occurred only after addition of a suitable reducing agent. The mechanism proposed suggested the formation of any gold(III) and gold(I) complex, as long as the ablation process is performed in the presence of the right amount of ligands. However, it must be realized that the formation of ionic compounds through laser ablation depends on the nature of the solvent. Any solvent with strong reducing properties does not lead to the formation of gold complexes.

Ultrasonic irradiation of aqueous solutions of a gold salt and an aliphatic alcohol leads to the formation of polydisperse gold colloids. In chloroform solutions of CTAB however, we were able to effectively oxidize solid gold to Au(III). The bromide ion, which is provided by CTAB, acts as a nucleophile lowering the reduction potential of gold, and oxygen from the air subsequently oxidizes the gold. Only after the addition of a suitable reducing agent gold colloids are formed.

Gold nanorods were formed using a wet chemical seed-mediated growth technique in aqueous solutions of cetyltrimethylammonium bromide (CTAB). We were able to prepare gold nanorods with high aspect ratios ( $> 20$ ) and average lengths of more than 1000 nm. We showed that the length and aspect ratios of the nanorods can be manipulated by varying the CTAB concentration.

The last chapter of this PhD thesis discusses the procedure to prepare gold nanoshells on dielectric cores of silica nanoparticles. The plasmon resonance is now tunable over a wide range of the ultraviolet and visible region. Hence, gold nanoparticles of different shapes are valuable potential candidates for many future optical applications.

## **APPENDIX**



## A. GROUP THEORY APPLICATIONS FOR GOLD COMPLEXES

This appendix describes group theoretical applications for gold complexes. For a more detailed discussion of chemical applications of group theory, we refer to the handbook of F. Albert Cotton [111]. It is not the intention of this appendix to give a full explanation, but only to give a more theoretical understanding of the use of symmetry in relation with gold complexes. Hence, it is assumed that the reader is familiar with symmetry operations, character tables and point groups.

A molecule possesses electronic, vibrational and rotational energies. The rotational energies have no symmetry properties and will not be mentioned in this appendix. We will focus on molecular vibrations and electronic transitions.

### A.1 Molecular vibrations

In this work we have not performed Infrared spectroscopy neither Raman spectroscopy of gold complexes. However, the use of group theory gives us more insight in the symmetry and applications, and shows which modes are Raman active and which Infrared active. Furthermore, a detailed worked out example helps us to understand more the construction of a molecular orbital energy level diagram useful for electronic spectroscopy. The gold complexes important in our study are the halo complexes  $[\text{AuX}_4]^-$  and  $[\text{AuX}_2]^-$  ( $\text{X} = \text{Cl}, \text{Br}$ ). In this appendix the gold complex  $[\text{AuX}_4]^-$  has been worked out with group theory to find the fundamental vibrational modes. This is a square planar molecule and belongs to the  $D_{4h}$  point group. The gold complex  $[\text{AuX}_2]^-$  is a linear molecule and belongs to the  $D_{\infty h}$

point group, but is not worked out completely. The characters tables represented for these gold complexes are given in Table A.2 and Table A.3 respectively.

### A.1.1 Square-planar complexes $[\text{AuX}_4]^-$

The group theoretical application for the square-planar complexes is now worked out. First of all a total reducible representation ( $\Gamma_{3N}$ ) describing the total degrees of freedom for the  $[\text{AuX}_4]^-$  complex has to be found. Therefore we need to know the contribution of each symmetry operation that moves an atom onto another atom ( $\Gamma_{xyz}$ ). Furthermore we need to know the contribution of the unmoved atoms ( $\Gamma_{\text{u.m.a.}}$ ) to the total representation. Combining  $\Gamma_{xyz}$  and  $\Gamma_{\text{u.m.a.}}$  gives the total reducible representation

$D_{4h}$	$E$	$2C_4$	$C_2$	$2C'_2$	$2C''_2$	$i$	$2S_4$	$\sigma_h$	$2\sigma_v$	$2\sigma_d$
$\Gamma_{xyz}$	3	1	-1	-1	-1	-3	-1	1	1	1
$\Gamma_{\text{u.m.a.}}$	5	1	1	3	1	1	1	5	3	1
$\Gamma_{3N}$	15	1	-1	-3	-1	-3	-1	5	3	1

With the decomposition formula the irreducible representations can be found<sup>1</sup>

$$a_i = \frac{1}{h} \sum_{\mathcal{R}} g \chi_i(\mathcal{R}) \chi_T(\mathcal{R}) \quad (\text{A.1})$$

where  $a_i$  is the number of contributions for the irreducible representation,  $\mathcal{R}$  refers to one particular operation,  $h$  is the order of the group,  $g$  is the number of elements in the class,  $\chi_i(\mathcal{R})$  is the character for the symmetry operation  $\mathcal{R}$  for the irreducible representation and  $\chi_T(\mathcal{R})$  is the character for the analogous operation  $\mathcal{R}$  in the total reducible representation. The decomposition of the total reducible representation has been worked out for the  $D_{4h}$  point group and the results are found in Table A.1. The total representation is composed of

$$\Gamma_{3N} = A_{1g} + A_{2g} + B_{1g} + B_{2g} + E_g + 2A_{2u} + B_{2u} + 3E_u$$

This result can be checked. We should have  $3n = 15$  total degrees of freedom, so

<sup>1</sup> Note that F. Albert Cotton does not write the term  $g$ , the number of elements in the class. This is written here for completeness.



**Tab. A.1:** The decomposition of the total reducible representation ( $\Gamma_{3N}$ ) to find all the irreducible representations for the  $D_{4h}$  point group.

$$\begin{aligned}
a_{A_{1g}} &= \frac{1}{16}(1 \cdot 1 \cdot 15 + 2 \cdot 1 \cdot 1 + 1 \cdot 1 \cdot 1 + 2 \cdot 1 \cdot 3 + 2 \cdot 1 \cdot 1 + 1 \cdot 1 \cdot 3 + 2 \cdot 1 \cdot 1 + 1 \cdot 1 \cdot 5 + 2 \cdot 1 \cdot 3 + 2 \cdot 1 \cdot 1) = \frac{16}{16} = 1 \\
a_{A_{2g}} &= \frac{1}{16}(1 \cdot 1 \cdot 15 + 2 \cdot 1 \cdot 1 + 1 \cdot 1 \cdot 1 + 2 \cdot 1 \cdot 3 + 2 \cdot 1 \cdot 1 + 1 \cdot 1 \cdot 3 + 2 \cdot 1 \cdot 1 + 1 \cdot 1 \cdot 5 + 2 \cdot 1 \cdot 3 + 2 \cdot 1 \cdot 1) = \frac{16}{16} = 1 \\
a_{B_{1g}} &= \frac{1}{16}(1 \cdot 1 \cdot 15 + 2 \cdot 1 \cdot 1 + 1 \cdot 1 \cdot 1 + 2 \cdot 1 \cdot 3 + 2 \cdot 1 \cdot 1 + 1 \cdot 1 \cdot 3 + 2 \cdot 1 \cdot 1 + 1 \cdot 1 \cdot 5 + 2 \cdot 1 \cdot 3 + 2 \cdot 1 \cdot 1) = \frac{16}{16} = 1 \\
a_{B_{2g}} &= \frac{1}{16}(1 \cdot 1 \cdot 15 + 2 \cdot 1 \cdot 1 + 1 \cdot 1 \cdot 1 + 2 \cdot 1 \cdot 3 + 2 \cdot 1 \cdot 1 + 1 \cdot 1 \cdot 3 + 2 \cdot 1 \cdot 1 + 1 \cdot 1 \cdot 5 + 2 \cdot 1 \cdot 3 + 2 \cdot 1 \cdot 1) = \frac{16}{16} = 1 \\
a_{E_g} &= \frac{1}{16}(1 \cdot 2 \cdot 15 + 2 \cdot 0 \cdot 1 + 1 \cdot 2 \cdot 1 + 2 \cdot 0 \cdot 3 + 2 \cdot 0 \cdot 1 + 1 \cdot 2 \cdot 3 + 2 \cdot 0 \cdot 1 + 1 \cdot 2 \cdot 5 + 2 \cdot 0 \cdot 3 + 2 \cdot 0 \cdot 1) = \frac{16}{16} = 1 \\
a_{A_{1u}} &= \frac{1}{16}(1 \cdot 1 \cdot 15 + 2 \cdot 1 \cdot 1 + 1 \cdot 1 \cdot 1 + 2 \cdot 1 \cdot 3 + 2 \cdot 1 \cdot 1 + 1 \cdot 1 \cdot 3 + 2 \cdot 1 \cdot 1 + 1 \cdot 1 \cdot 5 + 2 \cdot 1 \cdot 3 + 2 \cdot 1 \cdot 1) = \frac{0}{16} = 0 \\
a_{A_{2u}} &= \frac{1}{16}(1 \cdot 1 \cdot 15 + 2 \cdot 1 \cdot 1 + 1 \cdot 1 \cdot 1 + 2 \cdot 1 \cdot 3 + 2 \cdot 1 \cdot 1 + 1 \cdot 1 \cdot 3 + 2 \cdot 1 \cdot 1 + 1 \cdot 1 \cdot 5 + 2 \cdot 1 \cdot 3 + 2 \cdot 1 \cdot 1) = \frac{32}{16} = 2 \\
a_{B_{1u}} &= \frac{1}{16}(1 \cdot 1 \cdot 15 + 2 \cdot 1 \cdot 1 + 1 \cdot 1 \cdot 1 + 2 \cdot 1 \cdot 3 + 2 \cdot 1 \cdot 1 + 1 \cdot 1 \cdot 3 + 2 \cdot 1 \cdot 1 + 1 \cdot 1 \cdot 5 + 2 \cdot 1 \cdot 3 + 2 \cdot 1 \cdot 1) = \frac{0}{16} = 0 \\
a_{B_{2u}} &= \frac{1}{16}(1 \cdot 1 \cdot 15 + 2 \cdot 1 \cdot 1 + 1 \cdot 1 \cdot 1 + 2 \cdot 1 \cdot 3 + 2 \cdot 1 \cdot 1 + 1 \cdot 1 \cdot 3 + 2 \cdot 1 \cdot 1 + 1 \cdot 1 \cdot 5 + 2 \cdot 1 \cdot 3 + 2 \cdot 1 \cdot 1) = \frac{16}{16} = 1 \\
a_{E_u} &= \frac{1}{16}(1 \cdot 2 \cdot 15 + 2 \cdot 0 \cdot 1 + 1 \cdot 2 \cdot 1 + 2 \cdot 0 \cdot 3 + 2 \cdot 0 \cdot 1 + 1 \cdot 2 \cdot 3 + 2 \cdot 0 \cdot 1 + 1 \cdot 2 \cdot 5 + 2 \cdot 0 \cdot 3 + 2 \cdot 0 \cdot 1) = \frac{48}{16} = 3
\end{aligned}$$

**Tab. A.2:** Character table representing the  $D_{4h}$  group characteristic for  $[\text{AuX}_4]^-$ .

$D_{4h}$	$E$	$2C_4$	$C_2$	$2C'_2$	$2C''_2$	$i$	$2S_4$	$\sigma_h$	$2\sigma_v$	$2\sigma_d$		
$A_{1g}$	1	1	1	1	1	1	1	1	1	1	$R_z$	$x^2 + y^2, z^2$
$A_{2g}$	1	1	1	-1	-1	1	1	1	-1	-1		$x^2 - y^2$
$B_{1g}$	1	-1	1	1	-1	1	-1	1	1	-1		$xy$
$B_{2g}$	1	-1	1	-1	1	1	-1	1	-1	1		$(xz, yz)$
$E_g$	2	0	-2	0	0	2	0	-2	0	0	$(R_x, R_y)$	$(xz, yz)$
$A_{1u}$	1	1	1	1	1	-1	-1	-1	-1	-1		
$A_{2u}$	1	1	1	-1	-1	-1	-1	-1	1	1		$z$
$B_{1u}$	1	-1	1	1	-1	-1	1	-1	-1	1		
$B_{2u}$	1	-1	1	-1	1	-1	1	-1	1	-1	$(x, y)$	
$E_u$	2	0	-2	0	0	-2	0	2	0	0		

we should have 15 one-dimensional irreducible representations. The total representation is comprised of 11 irreducible representations, but four of them are two-dimensional representations ( $E$ ). Taking this into account, we get the 15 degrees of freedom. However, we have to subtract the translations and rotational degrees of freedom ( $(x, y, z)$  and  $(R_x, R_y, R_z)$  in Table A.2) to find the fundamental modes of vibration for the gold complex

$$\begin{aligned}
\Gamma_{vib} &= \Gamma_{3N} - \Gamma_{T+R} \\
&= (A_{1g} + A_{2g} + B_{1g} + B_{2g} + E_g + 2A_{2u} + B_{2u} + 3E_u) - (A_{2g} + E_g + A_{2u} + E_u) \\
&= A_{1g} + B_{1g} + B_{2g} + A_{2u} + B_{2u} + 2E_u
\end{aligned}$$

We are left with  $3n - 6 = 9$  fundamental modes of vibration. Having  $E$  as a

two-dimensional representation, we have satisfied this requirement<sup>2</sup>. However, we still need to find which of these vibrations occur in infrared and/or Raman spectra. Therefore, we need to introduce selection rules. Without going too much into detail we give the selection rules described by Cotton [111]. For IR active molecules

*A normal vibrational mode will be infrared active if it belongs to the same representation as any one or several of the Cartesian coordinates*

For Raman active molecules

*A normal vibrational mode will be Raman active if it belongs to the same representation as one or more of the products or a simple combination of the Cartesian coordinates*

With the use of the character tables showing to which representations the Cartesian coordinates and combinations thereof belong to, it is easy to find which fundamental modes are IR active and which Raman active. Furthermore, there is another important selection rule for centrosymmetric molecules which is called the exclusion rule

*In a centrosymmetric molecule no Raman-active vibration is also infrared-active and no infrared-active vibration is also Raman-active*

With these selection rules in mind we find the IR and Raman active modes for the square planar gold complex

$\nu_1(A_{1g}), \nu_2(B_{1g}), \nu_3(B_{2g})$	Raman active
$\nu_4(A_{2u}), \nu_6(E_u), \nu_7(E_u)$	Infrared active
$\nu_5(B_{2u})$	Inactive

The Au-X stretching vibrations can also be found with the aid of group theoretical applications. Therefore, we need to find a new reducible representation using the Au-X stretch as the basis set. This reducible representation is

<sup>2</sup> Some textbooks write that there are seven fundamental modes of vibration for the square planar gold complexes, however with this treatment we showed that there have to be nine when the two-dimensional representation is included.

**Tab. A.3:** Character table representing the  $D_{\infty h}$  group characteristic for  $[\text{AuX}_2]^-$ 

$D_{\infty h}$	$E$	$2C_{\infty}^{\Phi}$	...	$\infty\sigma_v$	$i$	$2S_{\infty}^{\Phi}$	...	$\infty C_2$		
$\Sigma_g^+$	1	1	...	1	1	1	...	1	$R_z$ $(R_x, R_y)$	$x^2 + y^2, z^2$
$\Sigma_g^-$	1	1	...	-1	1	1	...	-1		$(xz, yz)$
$\Pi_g$	2	$2\cos\Phi$	...	0	2	$-2\cos\Phi$	...	0		$(x^2 - y^2, xy)$
$\Delta_g$	2	$2\cos 2\Phi$	...	0	2	$2\cos 2\Phi$	...	0		
...	...	...	...	...	...	...	...	...		
$\Sigma_u^+$	1	1	...	1	-1	-1	...	-1	$z$ $(x, y)$	
$\Sigma_u^-$	1	1	...	-1	-1	-1	...	1		
$\Pi_u$	2	$2\cos\Phi$	...	0	-2	$2\cos\Phi$	...	0		
$\Delta_u$	2	$2\cos 2\Phi$	...	0	-2	$-2\cos 2\Phi$	...	0		
...	...	...	...	...	...	...	...	...		

$D_{4h}$	$E$	$2C_4$	$C_2$	$2C_2'$	$2C_2''$	$i$	$2S_4$	$\sigma_h$	$2\sigma_v$	$2\sigma_d$
$\Gamma_{\text{stretch}}$	4	0	0	2	0	0	0	4	2	0

Again, this representation can be reduced with the decomposition formula (Equation A.1) to find the irreducible representations for the stretching modes resulting in

$$\Gamma_{\text{stretch}} = A_{1g} + B_{1g} + E_u$$

There are three Au-X stretching vibrations with two of them ( $\nu_1$  and  $\nu_2$ ) Raman active and the other ( $\nu_6$ ) infrared active. All the other modes are bending modes and are not considered here further.

### A.1.2 Linear molecules $[\text{AuX}_2]^-$

The procedure described for the square planar molecules to find the normal modes of vibration is not trivial for the linear molecules  $[\text{AuX}_2]^-$  which belong to the infinite point group  $D_{\infty h}$  with the character table represented in Table A.3. In this appendix we are not going to deduce these vibrational modes as this can be found elsewhere. Reference [112] for example gives a relatively easy method for determining the irreducible representations. The general procedure however is the same as for the square planar complexes as there has to be found a reducible representation  $\Gamma_{3N}$  which has to be decomposed to find the irreducible representations. The

total representation is composed of

$$\Gamma_{3N} = \Sigma_g^+ + \Pi_g + 2\Sigma_u^+ + 2\Pi_u$$

When subtracting the translations and rotational<sup>3</sup> degrees of freedom (  $(x, y, z)$  and  $(R_x, R_y)$  in Table A.3) the fundamental modes of vibration for the linear gold complex can be found

$$\begin{aligned}\Gamma_{vib} &= \Gamma_{3N} - \Gamma_{T+R} \\ &= (\Sigma_g^+ + \Pi_g + 2\Sigma_u^+ + 2\Pi_u) - (\Pi_g + \Sigma_u^+ + \Pi_u) \\ &= \Sigma_g^+ + \Sigma_u^+ + \Pi_u\end{aligned}$$

With the aid of the selection rules and character table we find the IR and Raman active normal modes

$$\begin{array}{ll}\nu_1(\Sigma_g^+) & \text{Raman active} \\ \nu_2(\Sigma_u^+), \nu_3(\Pi_u) & \text{Infrared active}\end{array}$$

where  $\nu_1$  is the symmetric stretching vibration,  $\nu_2$  the asymmetric stretching vibration and  $\nu_3$  the bending vibration.

---

<sup>3</sup> For linear molecules there are only two rotational degrees of freedom, hence linear molecules have  $3N - 5$  vibrational modes.

## A.2 Ultraviolet-Visible Spectroscopy

The UV-Vis spectra of gold(I) complexes have very high energy bands and are assigned as ligand-to-metal charge-transfer transitions [29, 113]. Our interest however, will focus on the electronic spectra of the square planar  $[\text{AuX}_4]^-$  complexes. Again, it is not the intention of this appendix to give a full explanation of crystal field theory, ligand field theory and molecular orbital theory. An explanation of these can be found in textbooks as Reference [114]. However, we will use these

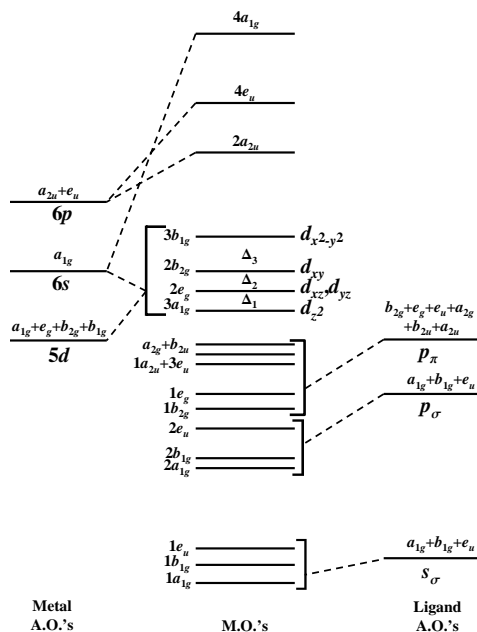


**Fig. A.1:** Qualitative Molecular orbital energy levels for a square-planar gold(III) complex.

theories together with group theory for explaining the qualitative molecular-orbital energy level diagram for a square-planar gold(III) complex as shown in Figure A.1.

### A.2.1 Ligand Field Theory

Ligand field theory is an application of molecular orbital theory that concentrates on the five  $d$  orbitals ( $d_{z^2}$ ,  $d_{x^2-y^2}$ ,  $d_{yz}$ ,  $d_{zx}$  and  $d_{xy}$ ) of a central metal atom in a

complex. For octahedral and tetrahedral symmetry the  $d$  orbitals split into two sets [111, 114] and the separation between the orbitals is called the ligand-field splitting parameter  $\Delta_o$  or  $\Delta_t$ <sup>4</sup>. However, the square planar gold complexes  $[\text{AuX}_4]^-$  belong to the lower symmetry  $D_{4h}$ . When referring to the character table for  $D_{4h}$  (Table A.2) we obtain specific information to find the corresponding representations for the  $d$  orbitals

$$\begin{array}{ll} A_{1g} & d_{z^2} \\ B_{1g} & d_{x^2-y^2} \\ B_{2g} & d_{xy} \\ E_g & d_{xz}, d_{yz} \end{array}$$

There are four different symmetry species corresponding to the orbitals. Hence, it is required to use three orbital splitting parameters ( $\Delta_1, \Delta_2$  and  $\Delta_3$ ) as can be seen in the qualitative molecular orbital energy diagram (Figure A.1). The order of the  $d$  orbital energies is a matter of making quantum mechanical computations and was found to be  $d_{x^2-y^2} > d_{xy} > d_{xz} > d_{yz} > d_{z^2}$  [27, 31, 32].

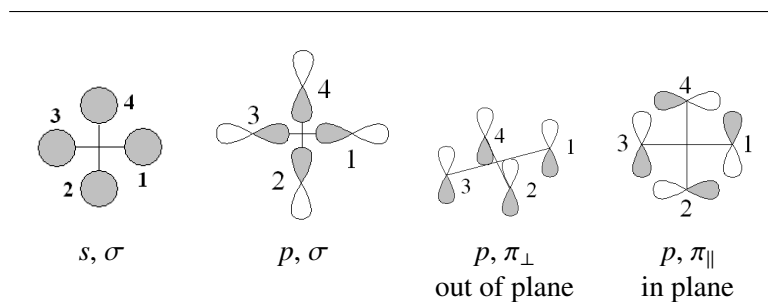
The interaction of the  $d$  orbitals with the valence orbitals of the four halogen ligands can be described by the Molecular Orbital Theory to obtain symmetry-adapted linear combinations (SALCs). This is discussed in the next section.

### A.2.2 Symmetry Adapted Linear Combinations (SALCs)

We will now discuss the strategy for describing the molecular orbitals of a metal complex by constructing linear combinations of atomic orbitals. The valence shell orbitals of the ligands are used as a basis set to find a reducible representation of the point group of the molecule. This representation then has to be decomposed into its component irreducible representations. The ligand orbitals are then combined into linear combinations belonging to these irreducible representations by using the projections operator

$$\hat{\mathcal{P}}^{\Gamma_i} = \frac{l_i}{h} \sum_{\mathcal{R}} \chi_i(\mathcal{R}) \hat{\mathcal{R}} \quad (\text{A.2})$$

<sup>4</sup> The subscript  $o$  in  $\Delta_o$  signifies octahedral symmetry whereas  $t$  in  $\Delta_t$  signifies tetrahedral.

**Tab. A.4:** The symmetry related sets of ligand valence shell orbitals in a square planar complex with a numbering system.

where  $l_i$  the dimensionality of the irreducible representation  $\Gamma_i$ ,  $h$  the order of the group,  $\chi_i(\mathcal{R})$  the character for operation  $\mathcal{R}$  in the irreducible representation  $\Gamma_i$  and  $\hat{\mathcal{R}}$  a symmetry operation<sup>5</sup>. The term  $l_i/h$  is not important as we have to normalize the functions.

The valence shell orbitals of the ligands are the  $s$ ,  $p_x$ ,  $p_y$  and  $p_z$  orbitals, but it is more convenient to think of the orbitals within symmetry related sets. Table A.4 shows schematically the  $s$  and  $p$  orbitals and their corresponding symmetry. The  $s$  orbital is spherically symmetric. Together with one  $p$  orbital, the  $s$  orbital constructs  $\sigma$  bonds. The other two  $p$  orbitals have the possibility to construct  $\pi$  bonds, but are out of plane ( $\perp$ ) and in plane ( $\parallel$ ) respectively. These orbitals symmetry sets can be used to find reducible representations

$D_{4h}$	$E$	$2C_4$	$C_2$	$2C'_2$	$2C''_2$	$i$	$2S_4$	$\sigma_h$	$2\sigma_v$	$2\sigma_d$
$\Gamma_\sigma$	4	0	0	2	0	0	0	4	2	0
$\Gamma_{\pi_\perp}$	4	0	0	-2	0	0	0	-4	2	0
$\Gamma_{\pi_\parallel}$	4	0	0	-2	0	0	0	4	-2	0

These reducible representations reduce to the following irreducible representations:

$$\Gamma_\sigma = A_{1g} + B_{1g} + E_u$$

$$\Gamma_{\pi_\perp} = A_{2u} + B_{2u} + E_g$$

$$\Gamma_{\pi_\parallel} = A_{2g} + B_{2g} + E_u$$

<sup>5</sup> Every member of a class of symmetry operations has to be treated.

By using the projection operator, it is now possible to construct symmetry adapted linear combinations (SALCs). We work this out for the  $\Gamma_\sigma$  bonding and give the solutions for the  $\Gamma_{\pi_\perp}$  and  $\Gamma_{\pi_\parallel}$ . We use orbital 1 at random in Table A.4 and assign the orbital with  $\sigma$  ( $\sigma_1$ ).

$$\begin{aligned}
 \hat{\mathcal{P}}^{\Gamma_{A_{1g}}} &= \frac{1}{16} [(1)(\hat{E})(\sigma_1) + (1)(\hat{C}_4^1)(\sigma_1) + (1)(\hat{C}_4^3)(\sigma_1) + (1)(\hat{C}_2)(\sigma_1) + (1)(\hat{C}_2'^1)(\sigma_1) \\
 &\quad + (1)(\hat{C}_2'^2)(\sigma_1) + (1)(\hat{C}_2''^1)(\sigma_1) + (1)(\hat{C}_2''^2)(\sigma_1) + (1)(\hat{i})(\sigma_1) + (1)(\hat{S}_4^1)(\sigma_1) \\
 &\quad + (1)(\hat{S}_4^2)(\sigma_1) + (1)(\hat{\sigma}_h)(\sigma_1) + (1)(\hat{\sigma}_v^1)(\sigma_1) + (1)(\hat{\sigma}_v^2)(\sigma_1) + (1)(\hat{\sigma}_d^1)(\sigma_1) \\
 &\quad + (1)(\hat{\sigma}_d^2)(\sigma_1)] \\
 &= \frac{1}{16} [\sigma_1 + \sigma_2 + \sigma_4 + \sigma_3 + \sigma_1 + \sigma_3 + \sigma_4 + \sigma_2 + \sigma_3 + \sigma_2 + \sigma_4 + \sigma_1 + \sigma_1 \\
 &\quad + \sigma_3 + \sigma_4 + \sigma_2] \\
 &= \frac{1}{16} [4\sigma_1 + 4\sigma_2 + 4\sigma_3 + 4\sigma_4] = \frac{1}{4} [\sigma_1 + \sigma_2 + \sigma_3 + \sigma_4]
 \end{aligned}$$

We have now created a SALC and it has to be normalized

$$\Gamma_{A_{1g}} = \frac{1}{2} [\sigma_1 + \sigma_2 + \sigma_3 + \sigma_4]$$

Using the projection operator on  $B_{1g}$  we find (note that we have already done every symmetry operation on the  $\sigma$  orbital)

$$\begin{aligned}
 \hat{\mathcal{P}}^{\Gamma_{B_{1g}}} &= \frac{1}{16} [(1)(\sigma_1) + (-1)(\sigma_2) + (-1)(\sigma_4) + (1)(\sigma_3) + (1)(\sigma_1) + (1)(\sigma_3) \\
 &\quad + (-1)(\sigma_4) + (-1)(\sigma_2) + (1)(\sigma_3) + (-1)(\sigma_2) + (-1)(\sigma_4) + (1)(\sigma_1) \\
 &\quad + (1)(\sigma_1) + (1)(\sigma_3) + (-1)\sigma_4 + (-1)(\sigma_2)] \\
 &= \frac{1}{16} [4\sigma_1 - 4\sigma_2 + 4\sigma_3 - 4\sigma_4] = \frac{1}{4} [\sigma_1 - \sigma_2 + \sigma_3 - \sigma_4] \\
 \Rightarrow \Gamma_{B_{1g}} &= \frac{1}{2} [\sigma_1 - \sigma_2 + \sigma_3 - \sigma_4] \text{ when normalized}
 \end{aligned}$$



The  $E_u$  SALC is

$$\begin{aligned}
 \hat{\phi}^{\Gamma_{E_u}} &= \frac{1}{16} [(2)(\sigma_1) + (0)(\sigma_2) + (0)(\sigma_4) + (-2)(\sigma_3) + (0)(\sigma_1) + (0)(\sigma_3) \\
 &\quad + (0)(\sigma_4) + (0)(\sigma_2) + (-2)(\sigma_3) + (0)(\sigma_2) + (0)(\sigma_4) + (2)(\sigma_1) \\
 &\quad + (0)(\sigma_1) + (0)(\sigma_3) + (0)\sigma_4 + (0)(\sigma_2)] \\
 &= \frac{2}{16} [4\sigma_1 - 4\sigma_3] = \frac{1}{2} [\sigma_1 - \sigma_3] \\
 \Rightarrow \Gamma_{E_u} &= \frac{1}{\sqrt{2}} [\sigma_1 - \sigma_3] \text{ when normalized}
 \end{aligned}$$

However, since  $E_u$  is two-dimensional, there are two functions. We get the other function by  $C_2''$  symmetry<sup>6</sup>. Hence we find the normalized  $E_u$  functions

$$\Gamma_{E_u} = \frac{1}{\sqrt{2}} [\sigma_1 - \sigma_3] \quad \text{and} \quad \Gamma_{E_u} = \frac{1}{\sqrt{2}} [\sigma_2 - \sigma_4]$$

The same procedure by using the projection operator can be done for the  $\Gamma_{\pi_{\perp}}$  and  $\Gamma_{\pi_{\parallel}}$  irreducible representations. The normalized solutions for  $\Gamma_{\pi_{\perp}}$  are

$$\begin{aligned}
 \Gamma_{A_{2u}} &= \frac{1}{2} [\pi_{\perp 1} + \pi_{\perp 2} + \pi_{\perp 3} + \pi_{\perp 4}] \\
 \Gamma_{B_{2u}} &= \frac{1}{2} [\pi_{\perp 1} - \pi_{\perp 2} + \pi_{\perp 3} - \pi_{\perp 4}] \\
 \Gamma_{E_g} &= \frac{1}{\sqrt{2}} [\pi_{\perp 1} - \pi_{\perp 3}] \quad \text{and} \quad \Gamma_{E_u} = \frac{1}{\sqrt{2}} [\pi_{\perp 2} - \pi_{\perp 4}]
 \end{aligned}$$

The normalized solutions for  $\Gamma_{\pi_{\parallel}}$  are

$$\begin{aligned}
 \Gamma_{A_{2g}} &= \frac{1}{2} [\pi_{\parallel 1} + \pi_{\parallel 2} + \pi_{\parallel 3} + \pi_{\parallel 4}] \\
 \Gamma_{B_{2g}} &= \frac{1}{2} [\pi_{\parallel 1} - \pi_{\parallel 2} + \pi_{\parallel 3} - \pi_{\parallel 4}] \\
 \Gamma_{E_u} &= \frac{1}{\sqrt{2}} [\pi_{\parallel 1} - \pi_{\parallel 3}] \quad \text{and} \quad \Gamma_{E_u} = \frac{1}{\sqrt{2}} [\pi_{\parallel 2} - \pi_{\parallel 4}]
 \end{aligned}$$

The total orbital transformation scheme for the  $D_{4h}$  symmetry is given in Table A.5.

<sup>6</sup> Also possible with  $2C_4$ ,  $2S_4$  and  $2\sigma_d$ , the other symmetry operations transform the SALC into itself.

**Tab. A.5:** Orbital transformation scheme for the  $D_{4h}$  symmetry [115].

Representation	Metal Orbitals	Ligand Orbitals
$A_{1g}$	$d_{z^2}, s$	$\frac{1}{2}[\sigma_1 + \sigma_2 + \sigma_3 + \sigma_4]$
$A_{2g}$		$\frac{1}{2}[\pi_{  1} + \pi_{  2} + \pi_{  3} + \pi_{  4}]$
$A_{2u}$	$p_z$	$\frac{1}{2}[\pi_{\perp 1} + \pi_{\perp 2} + \pi_{\perp 3} + \pi_{\perp 4}]$
$B_{1g}$	$d_{x^2-y^2}$	$\frac{1}{2}[\sigma_1 - \sigma_2 + \sigma_3 - \sigma_4]$
$B_{2g}$	$d_{xy}$	$\frac{1}{2}[\pi_{  1} - \pi_{  2} + \pi_{  3} - \pi_{  4}]$
$B_{2u}$		$\frac{1}{2}[\pi_{\perp 1} - \pi_{\perp 2} + \pi_{\perp 3} - \pi_{\perp 4}]$
$E_g$	$d_{yz}, d_{xz}$	$\frac{1}{\sqrt{2}}[\pi_{\perp 1} - \pi_{\perp 3}], \frac{1}{\sqrt{2}}[\pi_{\perp 2} - \pi_{\perp 4}]$
$E_u$	$p_x, p_y$	$\frac{1}{\sqrt{2}}[\sigma_1 - \sigma_3], \frac{1}{\sqrt{2}}[\sigma_2 - \sigma_4]$ $\frac{1}{\sqrt{2}}[\pi_{  1} - \pi_{  3}], \frac{1}{\sqrt{2}}[\pi_{  2} - \pi_{  4}]$

This table gives the information from group theory needed to construct the qualitative molecular-orbital energy level diagram for the square-planar gold(III) complex as shown in Figure A.1. The molecular orbitals are approximated by

$$\Psi(\text{m.o.}) = C_{M(i)}\Phi(\text{metal}) + C_{L(j)}\Phi(\text{ligand}) \quad (\text{A.3})$$

where  $C$  refers to the normalization restrictions. The quantum calculation of the energies however is crucial and also the most difficult part of the procedure. However, this will not be explained here as this was not intention of this appendix.

## B. DERIVATION OF THE FLAT ELECTRICAL DOUBLE LAYER

The *fundamental differential equation* for the electrical double layer is

$$\Delta\psi = \frac{2nve}{\varepsilon} \sinh (ve\psi/kT) \quad (\text{B.1})$$

For a flat double layer around a colloid particle,  $\psi$  is only a function of  $x$ , which is the normal co-ordinate. Hence,  $\Delta\psi$  may be replaced by  $d^2\psi/dx^2$ . Furthermore, by introducing the following substitutions

$$y = ve\psi/kT, \quad z = ve\psi_0/kT, \quad \kappa^2 = \frac{2nv^2e^2}{\varepsilon kT}, \quad \text{and} \quad \xi = \kappa x$$

the fundamental differential equation B.1 is brought into a more simple form

$$\frac{d^2y}{d\xi^2} = \sinh y \quad (\text{B.2})$$

which is also  $(\sinh \alpha = (e^\alpha - e^{-\alpha})/2)$

$$2\frac{d^2y}{d\xi^2} = e^y - e^{-y} \quad \text{or} \quad 2\frac{dy}{d\xi} \frac{d^2y}{d\xi^2} = (e^y - e^{-y}) \cdot \frac{dy}{d\xi} \quad (\text{B.3})$$

The left term can be rewritten

$$\frac{d}{d\xi} \left( \frac{dy}{d\xi} \right)^2 = 2 \frac{dy}{d\xi} \frac{d}{d\xi} \frac{dy}{d\xi} = 2 \frac{dy}{d\xi} \frac{d^2y}{d\xi^2}$$

and by now integrating the left and right terms

$$\int \frac{d}{d\xi} \left( \frac{dy}{d\xi} \right)^2 d\xi = \int (e^y - e^{-y}) dy \quad (\text{B.4})$$

we find

$$\left( \frac{dy}{d\xi} \right)^2 = e^y + e^{-y} + C_1 \quad (\text{B.5})$$

For one single double layer, the constant  $C_1$  is (for  $\xi = \infty$  and therefore  $y = 0$  we have  $dy/d\xi = 0$ )

$$C_1 = -2$$

and we find (with the minus sign before the square root, since for positive values of  $y$  the derivative  $dy/d\xi$  is negative if  $x$  and  $\xi$  are counted positive from the surface into the bulk of the solution)

$$\frac{dy}{d\xi} = -\sqrt{e^y + e^{-y} - 2} = -(e^{y/2} - e^{-y/2}) \quad (\text{B.6})$$

This can be rewritten as

$$\frac{dy}{e^{y/2} - e^{-y/2}} = -d\xi \quad (\text{B.7})$$

When substituting  $\alpha = e^{y/2} \Rightarrow d\alpha = \frac{1}{2}e^{y/2}dy$  we obtain

$$\frac{2d\alpha}{\alpha^2 - 1} = \frac{d\alpha}{\alpha - 1} - \frac{d\alpha}{\alpha + 1} = d \ln(\alpha - 1) - d \ln(\alpha + 1)$$

Integration of Equation B.7 will then be

$$\int (d \ln(e^{y/2} - 1) - d \ln(e^{y/2} + 1)) = \int -d\xi \quad (\text{B.8})$$

or

$$\ln(e^{y/2} - 1) - \ln(e^{y/2} + 1) = \ln \frac{(e^{y/2} - 1)}{(e^{y/2} + 1)} = -\xi + C_2 \quad (\text{B.9})$$

The boundary condition of  $y = z$  for  $\xi = 0$  determines the value of  $C_2$

$$C_2 = \ln \frac{(e^{z/2} - 1)}{(e^{z/2} + 1)}$$

Inserting this value of  $C_2$  into Equation B.9 we obtain

$$\ln \frac{(e^{y/2} - 1)}{(e^{y/2} + 1)} = -\xi + \ln \frac{(e^{z/2} - 1)}{(e^{z/2} + 1)} \quad (\text{B.10})$$

and we can write this as

$$\exp \ln \frac{(e^{y/2} - 1)}{(e^{y/2} + 1)} = \exp \left( -\xi + \ln \frac{(e^{z/2} - 1)}{(e^{z/2} + 1)} \right) = \exp(-\xi) \cdot \exp \ln \frac{(e^{z/2} - 1)}{(e^{z/2} + 1)} \quad (\text{B.11})$$

or

$$\frac{(e^{y/2} - 1)}{(e^{y/2} + 1)} = e^{-\xi} \cdot \frac{(e^{z/2} - 1)}{(e^{z/2} + 1)} \quad (\text{B.12})$$

and because  $\tanh \alpha = \frac{e^\alpha - e^{-\alpha}}{e^\alpha + e^{-\alpha}}$  we get for the left term

$$\frac{(e^{y/2} - 1)}{(e^{y/2} + 1)} = \frac{(e^{2y/4} - e^{-y/4+y/4})}{(e^{2y/4} + e^{-y/4+y/4})} = \frac{(e^{y/4} - e^{-y/4})e^{y/4}}{(e^{y/2} + e^{-y/4})e^{y/4}} = \frac{(e^{y/4} - e^{-y/4})}{(e^{y/2} + e^{-y/4})} = \tanh \frac{y}{4}$$

The same can be done for the right term so Equation B.12 simplifies to

$$\tanh \frac{y}{4} = \tanh \frac{z}{4} e^{-\xi} \quad \text{or} \quad \tanh \left[ \frac{ve\psi}{4kT} \right] = \tanh \left[ \frac{ve\psi_0}{4kT} \right] e^{-\kappa x} \quad (\text{B.13})$$

which is the solution of a flat double layer around a colloid particle. However, if Equation B.12 is written in the following form

$$e^{y/2} = \frac{1 + \left( e^{-\xi} \cdot \frac{(e^{z/2}-1)}{(e^{z/2}+1)} \right)}{1 - \left( e^{-\xi} \cdot \frac{(e^{z/2}-1)}{(e^{z/2}+1)} \right)} \quad (\text{B.14})$$

which is the same as

$$y = 2 \ln \frac{1 + e^{-\xi} \cdot \gamma}{1 - e^{-\xi} \cdot \gamma}, \quad \text{with} \quad \gamma = \frac{e^{z/2} - 1}{e^{z/2} + 1} \quad (\text{B.15})$$

this equation can be simplified for  $\xi \gg 1$  to<sup>1</sup>

$$\begin{aligned}
 y &= 2 \ln \frac{(1 + e^{-\xi} \cdot \gamma)(1 + e^{-\xi} \cdot \gamma)}{(1 - e^{-\xi} \cdot \gamma)(1 + e^{-\xi} \cdot \gamma)} \\
 &= 2 \ln \frac{1 + 2e^{-\xi} \cdot \gamma + e^{-2\xi} \gamma^2}{1 - e^{-2\xi} \gamma^2} \\
 &\approx 2 \ln(1 + 2e^{-\xi} \cdot \gamma) \\
 &\approx 2 \left( 2e^{-\xi} \cdot \gamma - \frac{(2e^{-\xi} \cdot \gamma)^2}{2} + \frac{(2e^{-\xi} \cdot \gamma)^3}{3} - \dots \right) \\
 &\approx 4e^{-\xi} \cdot \gamma
 \end{aligned} \tag{B.16}$$

having a useful approximation for large values of  $x$ . When the substitution for  $\gamma$  is used and for small values of  $z$  ( $z \ll 1$ ), the following expression is obtained<sup>2</sup>

$$\begin{aligned}
 y &= 4e^{-\xi} \cdot \frac{e^{z/2} - 1}{e^{z/2} + 1} \\
 &= 4e^{-\xi} \cdot \frac{1 + z/2 + \frac{z/2}{2!} + \frac{z/2}{3!} + \dots - 1}{1 + z/2 + \frac{z/2}{2!} + \frac{z/2}{3!} + \dots + 1} \\
 &= 4e^{-\xi} \cdot \frac{z/2 + \frac{z/2}{2!} + \frac{z/2}{3!} + \dots}{2 + z/2 + \frac{z/2}{2!} + \frac{z/2}{3!} + \dots} \\
 &= 4e^{-\xi} \cdot \frac{z/2}{2 + z/2} \\
 &= 4e^{-\xi} \cdot \frac{z}{4} \\
 \Rightarrow y &= ze^{-\xi} \text{ or } \psi = \psi_0 e^{-\kappa x}
 \end{aligned} \tag{B.17}$$

which is the Debye-Hückel approximation.

---

<sup>1</sup>  $\ln(1 + x) = x - \frac{x^2}{2} + \frac{x^3}{3} - \dots$

<sup>2</sup>  $e^x = 1 + x + \frac{x^2}{2!} + \frac{x^3}{3!} + \dots$

## REFERENCES

- [1] J. M. Stillman. *The Story of Alchemy and early Chemistry*. Dover Publications, Inc., 1960.
- [2] H. M. Leicester. *The Historical Background of Chemistry*. Dover Publications, Inc., 1971.
- [3] L. B. Hunt. The True Story of Purple of Cassius. *Gold Bull.*, 9(4):134–139, 1976.
- [4] F. E. Wagner, S. Haslbeck, L. Stievano, S. Calogero, Q. A. Pankhurst, and K.-P. Martinek. Before striking gold in gold-ruby glass. *Nature*, 407:691–692, 2000.
- [5] D. J. Barber and I. C. Freestone. Before striking gold in gold-ruby glass. *Archaeometry*, 32:33–45, 1990.
- [6] C.-A. Reichen. *A history of chemistry*. Editio-Service S.A., Geneva Hawthorn Books Inc., 2 edition, 1968.
- [7] G. B. Kauffman. The Role of Gold In Alchemy. Part I. *Gold Bull.*, 18(1):31–44, 1985.
- [8] G. B. Kauffman. The Role of Gold In Alchemy. Part II. *Gold Bull.*, 18(2):69–78, 1985.
- [9] H. Hartley. *Studies in the History of Chemistry*. Oxford University Press, 1971.
- [10] M. Faraday. Experimental relations of gold (and other metals) to light. *Philos. Trans. R. Soc.*, page 1857, 145–181.
- [11] P. Mulvaney. Surface Plasmon Spectroscopy of Nanosized Metal Particles. *Langmuir*, 12:788–800, 1996.
- [12] R. A. Zsigmondy. Properties of Colloids. *Nobel Lecture*, December 11 1926. <http://www.nobel.se/chemistry/laureates/1925/zsigmondy-lecture.html>.
- [13] G. Mie. Beiträge zur optik trüber medien, speziell kolloidaler metallösungen von gustav mie. *Annalen Der Physik*, 25(3):377–445, 1908.
- [14] J. Turkevich. Colloidal Gold Part I: Historical and Preparative Aspects, Morphology and Structure. *Gold Bull.*, 18(3):86–91, 1985.

- [15] J. Turkevich, P. C. Stevenson, and J. Hillier. A Study of the Nucleation and Growth Processes in the Synthesis of Colloidal Gold. *Disc. Farad. Soc.*, 11:55–75, 1951.
- [16] R. H. Doremus. Optical Properties of Small Gold Particles. *J. Chem. Phys.*, 40(8):2389–2396, 1964.
- [17] G. Frens. Controlled Nucleation for the Regulation of the Particle Size in Monodisperse Gold Suspensions. *Nature Phys. Sci.*, 241:19–22, January 1 1973.
- [18] M. Brust, M. Walker, D. Bethell, D. J. Schiffrin, and R. Whyman. Synthesis of Thiol-derivatised Gold Nanoparticles in a Two-phase Liquid-Liquid System. *J. Chem. Soc.*, pages 801–802, 1994.
- [19] C. N. R. Rao, G. U. Kulkarni, P. J. Thomas, and P. P. Edwards. Size-Dependent Chemistry: Properties of Nanocrystals. *Chem. Eur. J.*, 8(1):29–35, 2002.
- [20] C. J. Murphy. Nanocubes and Nanoboxes. *Science*, 298:2139–2141, 2002.
- [21] The Royal Society & The Royal Academy of Engineering. *Nanoscience and Nanotechnologies*, 2004. <http://www.nanotec.org.uk/>.
- [22] R. F. Service. Nanotoxicology:nanotechnology grows up. *Science*, 304:1732–1734, 2004.
- [23] C. N. R. Rao and A. K. Cheetham. Science and technology of nanomaterials: current status and future prospects. *J. Mater. Chem.*, 11:2887–2894, 2001.
- [24] K. J. Klabunde, editor. *Nanoscale Materials in Chemistry*. John Wiley & Sons, Inc., 2001.
- [25] G. U. Kulkarni, P. J. Thomas, and C. N. R. Rao. Mesoscale organization of metal nanocrystals. *Pure Appl. Chem.*, 74(9):1581–1591, 2002.
- [26] T. Castro, R. Reifengerger, E. Choi, and R. P. Andres. Size-dependent melting temperature of individual nanometer-sized metallic clusters. *Phys. Rev. B*, 42(13):8548–8556, 1990.
- [27] R. J. Puddephatt. *The Chemistry of Gold*. Elsevier, 1978.
- [28] N. P. Finkelstein and R. D. Hancock. A New Approach to the Chemistry of Gold. *Gold Bull.*, 7:72–77, 1974.
- [29] H. Kunkely and A. Vogler. Photooxidation of  $\text{AuCl}_2^-$  and  $\text{AuBr}_2^-$  induced by ds Excitation. *Inorg. Chem.*, 31:4539–4541, 1992.
- [30] A. Vogler and H. Kunkely. Photoreactivity of gold complexes. *Coord. Chem. Rev.*, 219-221:489–507, 2001.
- [31] H. Basch and H. B. Gray. Molecular Orbital Theory for Square-Planar Metal Halide Complexes. *Inorg. Chem.*, 6(2):365–369, 1967.



- [32] W. R. Mason and H. B. Gray. Electronic Structures of Square-Planar Complexes. *J. Am. Chem. Soc.*, 90:5721–5729, 1968.
- [33] A. K. Gangopadhyay and A. Chakravorty. Charge Transfer Spectra of some Gold (III) Complexes. *J. Chem. Phys.*, 35:2206–2209, 1961.
- [34] J. Turkevich. Colloidal Gold Part II: Colour, Coagulation, Adhesion, Alloying and Catalytic Properties. *Gold Bull.*, 18(4):125–131, 1985.
- [35] B. V. Enustun and J. Turkevich. Coagulation of Colloidal Gold. *J. Am. Chem. Soc.*, 85:3317–3328, 1963.
- [36] R. J. Hunter. *Foundations of Colloid Science. Vol. 1.* Oxford University Press, 1989.
- [37] D. C. Grahame. The Electrical Double Layer and the Theory of Electrocapillarity. *Chem. Rev.*, 41:441–501, 1947.
- [38] R. J. Hunter. *Zeta Potential in Colloid Science.* Academic Press, 1981.
- [39] E. J. W. Verwey and J. TH. G. Overbeek. *Theory of the Stability of Lyophobic Colloids.* Elsevier Publishing Company, Inc., 1948.
- [40] J. O'M. Bockris, B. E. Conway, and E. Yeager, editors. *Comprehensive Treatise of Electrochemistry*, volume 1, chapter 9, pages 379–437. Plenum Press, New York, 1980.
- [41] D. J. Shaw. *Introduction to Colloid and Surface Chemistry.* Butterworths, 3rd edition, 1989.
- [42] H.-F. Eicke, editor. *Modern Trends of Colloid Science in Chemistry and Biology*, chapter 1, pages 9–33. Birkhäuser Verlag, Basel, 1985.
- [43] C. F. Bohren and D. R. Huffman. *Absorption and Scattering of Light by Small Particles.* Wiley, New York, 1983.
- [44] U. Kreibig and M. Vollmer. *Optical Properties of Metal Clusters*, volume 25. Springer, Berlin, 1995.
- [45] J. Zheng, C. Zhang, and R. M. Dickson. Highly Fluorescent, Water-Soluble, Size-Tunable Gold Quantum Dots. *Phys. Rev. Lett.*, 93(7):0774021–0774024, 2004.
- [46] C. Kittel. *Introduction to Solid State Physics.* John Wiley & Sons, Inc., third edition, 1966.
- [47] R. E. Dodd. *Chemical Spectroscopy.* Elsevier, New York, 1962.
- [48] M. M. Alvarez, J. T. Khoury, T. G. Schaaff, M. N. Shafigullin, I. Vezmar, and R. L. Whetten. Optical Absorption Spectra of Nanocrystal Gold Molecules. *J. Phys. Chem.*, 101:3706–3712, 1997.

- [49] S. Link and M. A. El-Sayed. Size and Temperature Dependence of the Plasmon Absorption of Colloidal Gold Nanoparticles. *J. Phys. Chem. B*, 103:4212–4217, 1999.
- [50] U. Kreibig and C. v. Fragstein. The Limitation of Electron Mean Free Path in Small Silver Particles. *Z. Phys.*, 224:307–323, 1969.
- [51] B. M. I. van der Zande, M. R. Böhmer, L. G. J. Fokkink, and C. Schönenberger. Colloidal Dispersions of Gold Rods: Synthesis and Optical Properties. *Langmuir*, 16:451–458, 2000.
- [52] R. Gans. Über die Form ultramikroskopischer Goldteilchen. *Ann. Phys.*, 37:881–900, 1912.
- [53] S. Link and M. A. El-Sayed. Simulation of the Optical Absorption Spectra of Gold Nanorods as a Function of Their Aspect Ratio and the Effect of the Medium Dielectric Constant. *J. Phys. Chem. B*, 103:3073–3077, 1999.
- [54] S. Link and M. A. El-Sayed. Spectral Properties and Relaxation Dynamics of Surface Plasmon Electronic Oscillations in Gold and Silver Nanodots and Nanorods. *J. Phys. Chem. B*, 103:8410–8426, 1999.
- [55] P. B. Johnson and R. W. Christy. Optical Constants of the Noble Metals. *Phys. Rev. B*, 6(12):4370–4379, 1972.
- [56] D. P. O’Neal, L. R. Hirsch, N. J. Halas, J. D. Payne, and J. L. West. Photo-thermal tumor ablation in mice using near infrared-absorbing nanoparticles. *Cancer Letters*, 209:171–176, 2004.
- [57] C. Loo, A. Lowery, N. Halas, J. West, and R. Drezek. Immunotar-geted Nanoshells for Integrated Cancer Imaging and Therapy. *Nano Lett.*, 5(4):709–711, 2005.
- [58] A. L. Aden and M. Kerker. Scattering of Electromagnetic Waves from Two Concentric Spheres. *J. App. Phys.*, 22(10):1242–1246, 1951.
- [59] P. Mulvaney and L. M. Liz-Marzan. Rational Material Design Using Au Core-Shell Nanocrystals. *Top. Curr. Chem.*, 226:225–246, 2003.
- [60] S. J. Oldenburg, R. D. Averitt, S. L. Westcott, and N. J. Halas. Nanoengi-neering of optical resonances. *Chem. Phys. Lett.*, 288:243–247, 1998.
- [61] O. P. Yadav, A. Palmqvist, N. Cruise, and K. Holmberg. Synthesis of plat-inum nanoparticles in microemulsions and their catalytic activity for the ox-idation of carbon monoxide. *Colloids Surfaces A*, 221:131–134, 2003.
- [62] K. L. Kelly, E. Coronado, L. L. Zhao, and G. C. Schatz. The Optical Prop-erties of Metal Nanoparticles: The Influence of Size, Shape, and Dielectric Environment. *J. Phys. Chem. B*, 107:668–677, 2003.
- [63] G. Schmid. The role of big metal clusters in nanoscience. *J. Chem. Soc., Dalton Trans.*, pages 1077–1082, 1998.

- [64] G. Schmid, M. Bäuml, M. Geerkens, I. Heim, C. Osemann, and T. Sawitowski. Current and future applications of nanoclusters. *Chem. Soc. Rev.*, 28:179–185, 1999.
- [65] E. Hutter and J. H. Fendler. Exploitation of Localized Surface Plasmon Resonance. *Adv. Mater.*, 16(19):1685–1706, 2002.
- [66] C. D. Keating, M. D. Musick, M. H. Keefe, and M. J. Natan. Kinetics and Thermodynamics of Au Colloid Monolayer Self-Assembly. *J. Chem. Ed.*, 76(7):949–955, 1999.
- [67] J. A. Rodriguez, J. Dvorak, T. Jirsak, G. Liu, J. Hrbek, Y. Aray, and C. Gonzalez. Coverage Effects and the Nature of the Metal-Sulfur Bond in S/Au(111): High-Resolution Photoemission and Density-Functional Studies. *J. Am. Chem. Soc.*, 125:276–285, 2003.
- [68] R. Whyman. Gold nanoparticles. A renaissance in gold chemistry. *Gold Bull.*, 29(1):11–15, 1996.
- [69] G. Koeckelberghs, L. De Cremer, W. Vanormelingen, T. Verbiest, A. Persoons, and C. Samyn. Synthesis and properties of polydithieno[3,2-b:2',3'-d]pyrroles: A class of soluble (chiral) conjugated polymers with a stable oxidized state. *Macromolecules*, 38:4545–4547, 2005.
- [70] S. Stoeva, K. J. Klabunde, C. M. Sorensen, and I. Dragieva. Gram-Scale Synthesis of Monodisperse Gold Colloids by the Solvated Metal Atom Dispersion Method and Digestive Ripening and Their Organization into Two- and Three-Dimensional Structures. *J. Am. Chem. Soc.*, 124(10):2305–2311, 2002.
- [71] L. Zhai and R. D. McCullough. Regioregular polythiophene gold nanoparticle hybrid materials. *J. Mater. Chem.*, 14:141–143, 2004.
- [72] T. G. Schaaff and R. L. Whetten. Giant Gold-Gluthione Cluster Compounds: Intense Optical Activity in Metal-Based Transitions. *J. Phys. Chem. B*, 104:2630–4641, 2000.
- [73] C. F. Shaw III, N. A. Schaeffer, R. C. Elder, M. K. Eidsness, J. M. Trooster, and G. H. M. Calis. Bovine Serum Albumin Gold Thiomalate Complex:  $^{197}\text{Au}$  Mössbauer, EXAFS and XANES, Electrophoresis,  $^{35}\text{S}$ -Radiotracer, and Fluorescent Probe Competition Studies. *J. Am. Chem. Soc.*, 106:3511–3521, 1984.
- [74] C. F. Shaw III, G. Schmitz, H. O. Thompson, and P. Witkiewicz. Bis (L-cysteinato)gold(I): Chemical Characterization and Identification in Renal Cortical Cytoplasm. *J. Inorg. Biochem.*, 10:317–330, 1979.
- [75] J. E. Anderson and S. M. Sawtelle. *In situ* generation and characterization of gold(I) complexes from  $\text{K}[\text{AuCl}_4]$  in aqueous solutions. *Inorganica Chimica Acta*, 194:171–177, 1992.
- [76] V. H. Perez-Luna, K. Aslan, and P. Betala. Colloidal Gold. In H.S. Nalwa, editor, *Encyclopedia of Nanoscience and Nanotechnology*, volume 2, pages 199–220. American Scientific Publishers, 2004.

- [77] J. Neddersen, G. Chumanov, and T. M. Cotton. Laser Ablation of Metals: A New Method for Preparing SERS Active Colloids. *Appl. Spectr.*, 47:1959–1964, 1993.
- [78] F. Mafuné, J.-y. Kohno, Y. Takeda, T. Kondow, and H. Sawabe. Formation and Size Control of Silver Nanoparticles by Laser Ablation in Aqueous Solution. *J. Phys. Chem. B.*, 104:9111–9117, 2000.
- [79] F. Mafuné, J.-y. Kohno, Y. Takeda, and T. Kondow. Structure and Stability of Silver Nanoparticles in Aqueous Solution Produced by Laser Ablation. *J. Phys. Chem. B.*, 104(35):8333–8337, 2000.
- [80] A. C. Curtis, D. G. Duff, P. P. Edwards, D. A. Jefferson, B. F. G. Johnson, A. I. Kirkland, and A. S. Wallace. Preparation and structural characterization of an unprotected copper sol. *J. Phys. Chem.*, 92:2270–2275, 1988.
- [81] A. Takami, H. Kurita, and S. Koda. Laser-Induced Size Reduction of Noble Metal Particles. *J. Phys. Chem. B.*, 103:1226–1232, 1999.
- [82] F. Mafuné, J.-y. Kohno, Y. Takeda, and T. Kondow. Formation of Gold Nanoparticles by Laser Ablation in Aqueous Solution of Surfactant. *J. Phys. Chem. B.*, 105:5114–5120, 2001.
- [83] Y. Takeuchi, T. Ida, and K. Kimura. Colloidal Stability of Gold Nanoparticles in 2-Propanol under Laser Irradiation. *J. Phys. Chem. B.*, 101:1322–1327, 1997.
- [84] F. Mafuné, J.-y. Kohno, Y. Takeda, and T. Kondow. Growth of Gold Clusters into Nanoparticles in a Solution Following Laser-Induced Fragmentation. *J. Phys. Chem. B.*, 106:8555–8561, 2002.
- [85] F. Mafuné, J.-y. Kohno, Y. Takeda, and T. Kondow. Dissociation and Aggregation of Gold Nanoparticles under Laser Irradiation. *J. Phys. Chem. B.*, 105:9050–9056, 2001.
- [86] K. Okitsu, A. Yue, S. Tanabe, H. Matsumoto, and Y. Yobiko. Formation of Colloidal Gold Nanoparticles in an Ultrasonic Field: Control of Rate of Gold(III) Reduction and Size of Formed Gold Particles. *Langmuir*, 17:7717–7720, 2001.
- [87] W. Chen, W. Cai, L. Zhang, G. Wang, and L. Zhang. Sonochemical Processes and Formation of Gold Nanoparticles within Pores of Mesoporous Silica. *J. Coll. Int. Sci.*, 238:291–295, 2001.
- [88] R. A. Caruso, M. Ashokkumar, and F. Grieser. Sonochemical Formation of Gold Sols. *Langmuir*, 18:7831–7836, 2002.
- [89] T. Pal, N. R. Jana, and T. K. Sau. Nucleophile Induced Dissolution of Gold. *Corrosion Science*, 39(5):981–986, 1997.
- [90] R.C. Weast, editor. *CRC Handbook of Chemistry and Physics*. The Chemical Rubber Co., 51st edition, 1970.

- [91] A. Henglein. Physicochemical Properties of Small Metal Particles in Solution: Microelectrode Reactions, Chemisorption, Composite Metal Particles, and the Atom-to-Metal Transition. *J. Phys. Chem.*, 97:5457–5471, 1993.
- [92] M. D. Benari, G. T. Hefter, and A. J. Parker. Anodic Dissolution of Silver, Copper, Palladium and Gold in Dimethylsulfoxide-Halide Solutions. *Hydrometallurgy*, 10:367–389, 1983.
- [93] Y. Nakao. Dissolution of Metals in Halogen-Cetylpyridinium Halide-Benzene Systems. *J. Chem. Research (S)*, pages 228–229, 1991.
- [94] Y. Nakao. Dissolution of Noble Metals in Halogen-Halide-Polar Organic Solvent Systems. *J. Chem. Soc., Chem. Commun.*, pages 426–427, 1991.
- [95] Y. Nakao. Preparation of a Gold Organosol in Chloroform and its Discolouration by Photoirradiation. *J. Chem. Soc., Chem. Commun.*, pages 2067–2068, 1994.
- [96] N. R. Jana, J. D. Gearheart, and C. J. Murphy. Wet Chemical Synthesis of High Aspect Ratio Cylindrical Gold Nanorods. *J. Phys. Chem. B*, 105:4065–4067, 2001.
- [97] B. M. I. van der Zande, M. R. Böhmer, L. G. J. Fokkink, and C. Schönenberger. Aqueous Gold Sols of Rod-Shaped Particles. *J. Phys. Chem. B*, 101:852–854, 1997.
- [98] Y. Niidome, K. Nishioka, H. Kawasaki, and S. Yamada. Rapid synthesis of gold nanorods by the combination of chemical reduction and photoirradiation processes; morphological changes depending on the growing processes. *Chem. Commun.*, 101:2376–2377, 2003.
- [99] F. Kim, J. H. Song, and P. Yang. Photochemical Synthesis of Gold Nanorods. *J. Am. Chem. Soc.*, 124:14316–14317, 2002.
- [100] C. J. Murphy and N. R. Jana. Controlling the Aspect Ratio of Inorganic Nanorods and Nanowires. *Adv. Mater.*, 14(1):80–81, 2002.
- [101] B. Nikoobakht and M. A. El-Sayed. Preparation and Growth Mechanism of Gold Nanorods (NRs) Using Seed-Mediated Growth Method. *Chem. Mater.*, 15:1957–1962, 2003.
- [102] J. Pérez-Juste, L. M. Liz-Marzán, S. Carnie, D. Y. C. Chan, and P. Mulvaney. Electric-Field-Directed Growth of Gold Nanorods in Aqueous Surfactant Solutions. *Adv. Funct. Mater.*, 14(6):571–579, 2004.
- [103] S. K. Kang, S. Chah, C. Y. Yun, and J. Yi. Aspect Ratio Controlled Synthesis of Gold Nanorods. *Korean J. Chem. Eng.*, 20(6):1145–1148, 2003.
- [104] N. K. Raman, M. T. Anderson, and C. J. Brinker. Template-Based Approaches to the Preparation of Amorphous, Nanoporous Silicas. *Chem. Mater.*, 8(8):1682–1701, 1996.

- [105] C. J. Brinker, Y. Lu, A. Sellinger, and H. Fan. Evaporation-Induced Self-Assembly: Nanostructures Made Easy. *Adv. Mater.*, 11(7):579–585, 1999.
- [106] T. Pham, J. B. Jackson, N. J. Halas, and T. R. Lee. Preparation and Characterization of Gold Nanoshells Coated with Self-Assembled Monolayers. *Langmuir*, 18:4915–4920, 2002.
- [107] C. Graf and A. van Blaaderen. Metallodielectric Colloidal Core-Shell Particles for Photonic Applications. *Langmuir*, 18:524–534, 2002.
- [108] N. J. Halas. The Optical Properties of Nanoshells. *Optics & Photonics News*, pages 26–30, August 2002.
- [109] W. Stöber, A. Fink, and E. Bohn. Controlled Growth of Monodisperse Silica Spheres in the Micron Size Range. *J. Colloid Interf. Sci.*, 26:62–69, 1968.
- [110] D. G. Duff, A. Baiker, and P. P. Edwards. A new hydrosol of gold clusters. 1. Formation and particle size variation. *Langmuir*, 9:2301–2309, 1993.
- [111] F. A. Cotton. *Chemical Applications of Group Theory*. John Wiley & Sons, Inc., 3rd edition, 1990.
- [112] J. A. Greathouse. Group Theory Calculations Involving Linear Molecules. *The Chemical Educator*, 1(1), 1996.
- [113] M. E. Koutek and W. R. Mason. Electronic Structure and Spectra of Linear Dihaloaurate Ions. *Inorg. Chem.*, 19:648–653, 1980.
- [114] D. F. Schriver and P. W. Atkins. *Inorganic Chemistry*. Oxford University Press, 3rd edition, 1999.
- [115] H. B. Gray and C. J. Ballhausen. A Molecular Orbital Theory for Square Planar Metal Complexes. *J. Am. Chem. Soc.*, 85:260–265, 1963.

## Publications

### International Publications

- *Laser ablation of gold in chloroform solutions of cetyltrimethylammonium bromide*  
T. Mortier, T. Verbiest and A. Persoons  
Chemical Physics Letters, 382 (5-6), 650-653 (2003)
- *Oxidation of solid gold in chloroform solutions of cetyltrimethylammonium bromide*  
T. Mortier, A. Persoons and T. Verbiest  
Inorganic Chemistry Communications, 8 (12), 1075-1077 (2005)
- *Two-step synthesis of high aspect ratio gold nanorods*  
T. Mortier, A. Persoons and T. Verbiest  
Central European Journal of Chemistry, 4 (1), 160-165 (2006)

### National Publications

- *Astrochemie: Een atomaire en moleculaire reis doorheen het heelal*  
KVCV Chemie Magazine, 2003, nr 4, 15-23
- *Colloidchemie: een historische schets van de zoektocht naar de eigenschappen van goudcolloïden*  
KVCV Chemie Magazine, 2003, nr 4, 26-29
- *Redactioneel: Nanomaterialen met verleden en toekomst*  
Mens & Molecule, 2005, 1 (3), p. 4
- *Redactioneel: Doctoreren in Vlaanderen*  
Mens & Molecule, 2005, 2 (2), p. 4





## **NEDERLANDSE SAMENVATTING**

### **Een experimentele studie over de bereiding van gouden nanodeeltjes en hun eigenschappen**

In het eerste gedeelte van dit proefschrift wordt de geschiedenis van colloidaal goud beschreven. De specifieke rode kleur van goudcolloïden werd namelijk reeds in de zeventiende eeuw gebruikt om glaswerk te kleuren. Bovendien bestaat er glaswerk uit de vierde eeuw na Christus waarvan uit analyse is gebleken dat men legeringen van goud- en zilvercolloïden had gebruikt in de fabricatie van het glas. Het tweede hoofdstuk geeft de nodige theoretische achtergrond. Vandaag behoort het onderzoek over de bereiding en de karakterisering van goudcolloïden namelijk tot het domein van de nanomaterialen. Hiermee wordt bedoeld dat de afmetingen van deze materialen liggen tussen 1 en 1000 nm. De elektrische, optische en magnetische eigenschappen van nanomaterialen kunnen immers sterk verschillen van deze in het bulk materiaal. De specifieke rode kleur van een goudsol is afkomstig van de zogenaamde plasmon resonantie. Plasmon resonanties ontstaan wanneer de golflengte van het licht groter is dan de afmeting van het nanodeeltje zelf. Hierdoor kunnen de elektronen van het nanodeeltje collectief gaan oscilleren bij een welbepaalde golflengte. Bovendien zijn de eigenschappen van de nanomaterialen sterk gerelateerd aan de vorm die ze aannemen. Zo vertonen sferische gouden nanodeeltjes een specifieke plasmonband in het elektronisch absorptiespectrum en vertonen gouden nanodraadjes twee plasmonbanden. Deze typische eigenschappen van goudcolloïden zijn uitermate interessant in de ontwikkeling van nanosensoren. Het fundamenteel onderzoek in het tweede gedeelte van dit proefschrift handelt over verschillende syntheses technieken om goudcolloïden te bereiden en te karak-

teriseren.

In een eerste experimenteel hoofdstuk worden enkele standaard technieken beschreven om sferische gouden nanodeeltjes te synthetiseren. Hierbij werd er een onderscheid gemaakt tussen de citraatreductiemethode en de Brust methode. Bij de citraatreductiemethode worden de goudcolloïden in waterige oplossingen kinetisch gestabiliseerd door de aanwezige negatieve citraationen nog aanwezig in de oplossing. De Brust methode geeft ons de mogelijkheid om goudcolloïden te stabiliseren in organische solventen met behulp van chirale thiolen waardoor er chiraliteit kan worden geïntroduceerd op het oppervlak van de gouden nanodeeltjes.

In de twee volgende hoofdstukken worden enkele fysicochemische technieken aangehaald om metaalcolloïden te bereiden. Metaalcolloïden kunnen respectievelijk worden gevormd door laserablatie van een bulk materiaal in eender welke oplossing en door de reductie van een goudzout gebruik makend van ultrasoon geluid (sonicatie). Met behulp van een kationisch surfactant in chloroform was het ook mogelijk om met beide technieken het bulk goud te oxideren ter vorming van goudcomplexen. In het geval van laserablatie kon de hypothese worden vooropgesteld dat in de eerste fase van het ablatieproces bulk goud ioniseert alvorens het zal reduceren ter vorming van goudcolloïden. In het geval van het ultrasoon geluid verlaagt een nucleofiel de reductiepotentiaal van het goud en wordt het vervolgens geoxideerd door zuurstof uit de lucht. In beide gevallen werd er enkel na toevoeging van een reductans colloïdaal goud gevormd.

De laatste twee hoofdstukken van dit proefschrift beschrijven syntheses technieken om gouden nanodeeltjes met verschillende vormen te fabriceren. Een volledige studie over de bereiding van gouden nanodraadjes in waterige oplossingen van een kationisch surfactant toont aan dat door een verhoging van de surfactant concentratie in water de gemiddelde lengte kan toenemen van 100 nm tot meer dan 1000 nm. Dit opent perspectieven voor een synthese op grote schaal.

In het laatste hoofdstuk tenslotte geven we de procedure met bijhorende resultaten voor de bereiding van silica nanodeeltjes die volledig omgeven zijn door een schil van goud. De plasmon resonantie van deze goudschillen kan geregeld worden over een groot gebied van het elektronisch absorptiespectrum. Deze deeltjes zijn daarom potentiële kandidaten voor vele optische toepassingen.